MESO-SCALE COOLING DEVICES EXPERIMENTAL AND NUMERICAL HEAT TRANSFER ANALYSIS
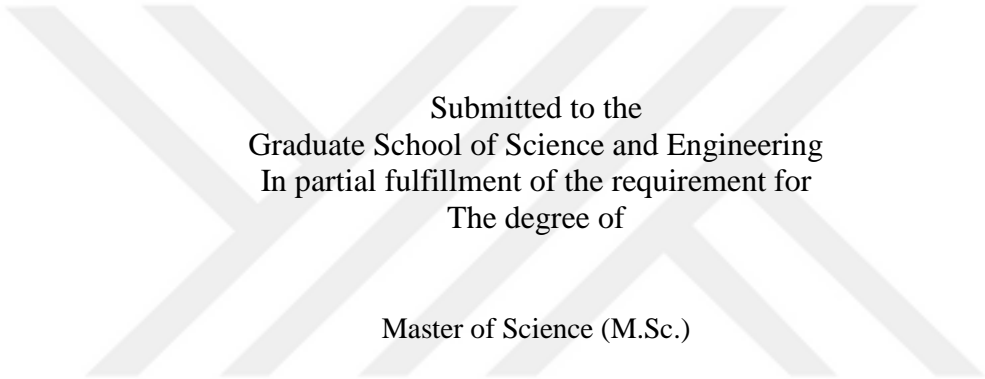
A Master of Science Thesis

by

Shadi Habibi Parsa

Submitted to the
Graduate School of Science and Engineering
In partial fulfillment of the requirement for
The degree of

Master of Science (M.Sc.)
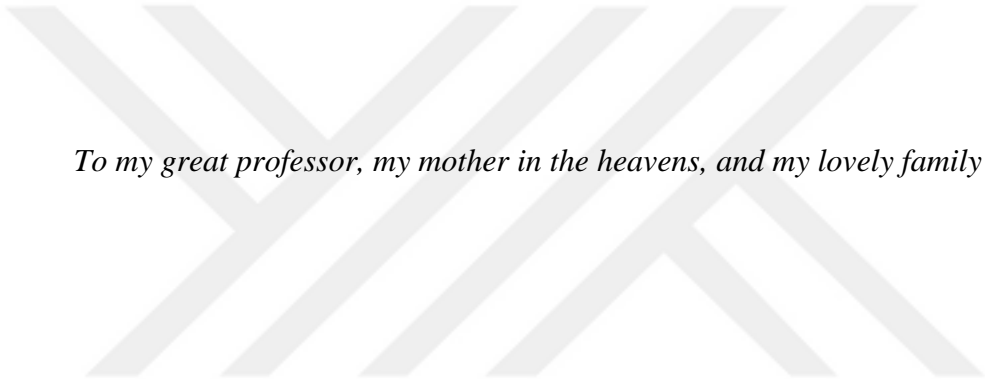
In the
Department of Mechanical Engineering

Özyeğin University
January, 2017

Approved by:

_____

Professor Dr. Mehmet Arik, Advisor
Department of Mechanical Engineering,
Özyeğin University

_____

_____

Date Approved: 2016.

2

To my great professor, my mother in the heavens, and my lovely family

ABSTRACT

Various thermal management strategies and related technologies are recently developed based on the specific needs, which they are designed to fulfill. Some of these technologies are muffin fans, synthetic jets, and piezoelectric fans. These three technologies are chosen based on the need to compare their core system of heat removing. The muffin fans are the small scale of the normal rotary fans which exploit a number of blades to produce a flow, which performs the cooling. Synthetic jets and the piezoelectric fans both use the oscillation created by a piezoelectric plate to establish a flow. The presence of an oscillating diaphragm in the synthetic jets simulates the breathing process which is done in the lungs of a human being. In the case of piezoelectric fans, the blade is being replaced with an oscillating cantilever beam which periodic movement generates a flow that eventually removes the heat.

This study consists of various parts; in the first part, previously mentioned technologies are experimentally compared, in terms of their heat transfer characteristics. In order to test the technologies, an experimental system was designed and manufactured. The test system consists of two main compartments. The heat source and the cooling device; cooling devices are secured on a plexi fixture. This stand is adjustable so that the cooling device can operate in various distances. Fixtures are designed and manufactured to securely hold the devices in position, in order to avoid any extra oscillation during operation. The heat source of the test set up is a square copper heater, placed in front of the cooling technology, which is under the tests. Then, the effect of distance on the heat removal of these cooling devices are examined and reported by putting them at various distances.

For the case of the muffin fan, it was observed that the heat transfer coefficient showed inverse relation with distance; higher distance exhibited low heat transfer and thus the fan was only applicable at close distances to the heater. For the synthetic jet, an optimum distance existed after which the heat transfer was not efficient. In the case of the piezoelectric fan, not

only increase in the distance resulted on the low heat transfer coefficient but also the heat transfer coefficient depended on the deflection of the piezoelectric fan slab. The effect of slab deflection is studied by the use of two different materials, mylar and metallic substrate fans. The highest Nusselt number for the synthetic jet and the piezoelectric fan is around 60 while for the muffin fan this number is less than 20. The deflection of the piezoelectric slab is so crucial that in the case of the mylar slab the highest achieved heat transfer coefficient is 20 W/m^2-K, while for the metallic fan it is approximately three times higher than mylar and it is about 58 W/m^2-K.

Beside the extensive experimental investigations, the piezoelectric fan is numerically modeled via FLUENT-ANSYS software in order to find the inaccessible results during experiments and better understanding of phenomena. The numerical results are in accordance with the experimental outcomes with a deviation of about 20 percent. The maximum velocity is found to be approximately 1.8 m/s.

The flow is also being visualized by the use of the PIV imaging during the heat transfer characteristics examination of the piezoelectric fan. PIV imaging results shed light on side cooling that partially happens at the close distances. The phenomenon of the side cooling is captured after the movement analysis of more than 5000 frames of the operating maylar piezoelectric fan. It is seen that in the distance less than 5 mm there is no time for the formation of the vortex and thus the induced flow is deprived towards the sides. This means that while the heat source is coordinated in the centerline of the fan; the induced flow is cooling the heat source sides and not the heater itself. This is not desirable since the cooling efficiency is lowered at this state.

Finally, a high-speed camera has also been used to capture the on spot behavior of the piezoelectric fan over the flow. With the frequency of 3000 frames per second of camera, the

flow is captured by the use of a smoke pen. The vortex formation is seen within the various frequencies of the piezoelectric fan. The effect of deflection value is also captured by the sequences of the camera. The formed vortex radius is different in the case of different deflection values.

ÖZETÇE

Son zamanlarda çeşitli termal yönetim stratejileri ve ilgili teknolojiler, özel ihtiyaçları yerine getirmek üzerine dayanarak geliştirilmektedir. Bu teknolojilerin bazıları muffin fanları, sentetik jetler ve piezoelektrik fanlardır. Bu üç teknoloji kendi çekirdek ısı giderim sistem karşılaştırma ihtiyacını baz alınarak seçilmiştir.

Muffin fanları, normal döner fanların küçük ölçeğidirler ve Soğutma yapan bir akım üretmek için bir dizi bıçak kullanırlar. Sentetik jetleri ve piezoelektrik fanların ikisi de akım oluşturmak için bir piezoelektrik plaka tarafından oluşturulan salınımı kullanırlar. Sentetik Jetlerde salınımlı bir diyafram varlığı insanın akciğerinde yapılan nefes alma işlemini simule eder. Bıçak, Piezoelektrik fanlardaki periyodik hareketi sonucunda ısıyı gideren bir akış oluşturan salınımlı konsol ışını ile değiştiriliyor.

Bu çalışma çeşitli bölümlerden oluşmaktadır, birinci bölümde, daha önce bahsedilen teknolojiler deneysel olarak, ısı transfer karakteristikleri bakımından karşılaştırılmıştır. Teknolojileri test etmek için deneysel bir sistem tasarlanıp ve üretilmiştir. Test sistemi iki ana bölmeden oluşur. Isı kaynağı ve soğutma cihazı; Soğutma cihazları bir plexi fikstüre sabitlenmiştir. Bu stand ayarlanabilir, böylece soğutma cihazı çeşitli mesafelerde çalışabilir. Fikstürler, çalışma esnasında ekstra salınımı önlemek için cihazları sabit tutacak şekilde tasarlanıp ve üretilmiştir. Testin kurulumun ısı kaynağı, testlerin altında olan soğutma teknolojisinin önüne yerleştirilen kare bir bakır ısıtıcıdır. Daha sonra uzaklığın bu soğutma cihazlarının ısı gidermesi üzerindeki etkisi, çeşitli mesafelere yerleştirilerek incelenir ve raporlanır

Muffin fan durumunda, ısı transfer katsayısının mesafe ile ters ilişki gösterdiği, yüksek mesafenin düşük ısı transferi sergilediği ve bu nedenle fan ısıtıcıya yakın mesafelerde uygulanabileceği görülmüştür. Sentetik jetler için, ısı aktarımı etkili olmadıktan sonra

optimum bir mesafe oluşur. Piezoelektrik fan durumunda, yalnızca düşük ısı aktarım katsayısı ile sonuçlanan mesafedeki artış değil, aynı zamanda, ısı aktarım katsayısı piezoelektrik fan levhasının dönmesine bağlıdır. Levhanın dönme etkisi, mylar ve metalik substrate fanları olmak üzere iki farklı malzeme kullanılarak incelenmiştir. Sentetik jet ve piezoelektrik fan için en yüksek Nusselt sayısı 60 civarındayken, muffin fanında bu sayı 20 den düşüktür. Piezoelektrik levhanın dönmesi o kadar önemlidir ki, mylar levhasında elde edilen en büyük ısı transferi eşdeğeri 20 W/m^2-K dır, metalik fan için mylar'dan yaklaşık üç kat daha yüksektir ve yaklaşık 58 W/m^2-K dır.

Kapsamlı deneysel soruşturmaların yanı sıra, Deneyler sırasında erişilemeyen sonuçların bulunması ve olayların daha iyi anlaşılması için, , piezoelektrik fan, sayısal olarak FLUENT-ANSYS yazılımı ile modellenmiştir. Sayısal sonuçlar, yaklaşık yüzde 20 sapma ile deney sonuçları ile uyumludur. Maksimum hız Yaklaşık 1.8 m/s olduğu bulunmuştur. Akış, piezoelektrik fanın ısı transfer özellikleri incelemesi sırasında PIV görüntüleme yöntemiyle de görselleştirilmektedir. PIV görüntüleme sonuçları, kısmen yakın mesafelerde gerçekleşen yan soğutma açıklığa kavuşturmasına yol açıyor. Yan soğutma olayı, 5000'den fazla kare maylar piezoelektrik fanın hareket analizinden sonra ele geçiyor.

5 mm'den daha az uzaklığa vorteks oluşumu için zaman olmadığı ve dolayısıyla sonuçlanan akışın yanlara doğru yoksun olduğu görülmektedir. Bunun anlamı, ısı kaynağının fan merkez çizgisinde koordine edilmesine rağmen, sonuçlanan akış ısı kaynağının yanlarını soğutulup, Isıtıcının kendisinin soğutulmamasıdır, bu durum arzu edilmez çünkü bu durumda soğutma verimi düşürülür.

Son olarak, yüksek hızlı bir kamera 'da piezoelektrik fanın akış üzerindeki nokta davranışını kaydetmek için kullanılmıştır. Kameranın saniyede 3000 kare frekansıyla akış bir duman kalemi kullanılarak kaydedilmiştir. Vorteks oluşumu piezoelektrik fanının çeşitli

frekanslarında görülür. Dönme değerinin etkisi kameranın dizileri tarafından da kaydedilmiştir. Oluşan vorteks etki alanı, farklı dönme değerleri durumunda farklıdır.

ACKNOWLEDGEMENT

TABLE OF CONTENTS

LIST OF FIGURES

NOMENCLATURE

A	Amplitude of oscillation	(m)
A_{area}	Approximate cross section area of the test enclosure	(m^2)
AC	Alternating current	(Ampere)
C	Characteristic length of the structure under oscillation	(m)
COP	Coefficient of performance	
D	Muffin fan diameter/synthetic jet nozzle's diameter	(m)
DAQ	Data acquisition	
DC	Direct current	(Ampere)
DOE	Design of experiment	
$DPIV$	Digital particle image velocimetry	
f	Frequency of vortex formation	(Hz)
fps	Frames per second	
FSI	Fluid-solid interaction	
F	Sum of drag and lift forces in rotary fan	
G	Distance between piezoelectric fan and heater	(m)
G/A	Distance ratio	
H	Distance between synthetic jet/muffin fan and heater	(m)
h_f	Heat transfer coefficient for forced convection	(W/m^2-K)
$h_{cooling\ device}$	Cooling device heat transfer coefficient	(W/m^2-K)
H/D	Distance ratio	
I_x	Partial derivative of the image data with respect to x	
I_y	Partial derivative of the image data with respect to y	
I_t	Partial derivative of the image data with respect to time	
K	Thermal conductivity	(W/m-K)
KC	Keulegan-Carpenter number	

L	Width of piezoelectric fan slab	(m)
LK	Lukas-Kanade (method)	
Nu	Nusselt number	
P	Wetted perimeter of the cross section of enclosure	(m)
PIV	Particle image velocimetry	
$Q_{natural\ convection}$	Heat removed by natural convection	(W)
$Q_{conduction}$	Heat removed by conduction	(W)
$Q_{cooling\ device}$	Heat removed by cooling device	(W)
Q_t	Total heat removed	(W)
Q_{net}	Net power given to heater	(W)
q_n	Number of pixels inside the window of the tracking program	
Re	Reynolds number	
Re_{osc}	Oscillatory Reynolds number	
St	Strouhal number	
s_i	Momentum source component	(kg.m/s)
T_s	Heat source (heater) temperature	
T_∞	Ambient temperature	
t	Time	
U	Main stream velocity	(m/s)
u_i	Velocity component of fluid in direction of x_i	(m/s)
V_{pp}	Peak to peak voltage value (AC)	(Volts)
V	Voltage value (DC)	(Volts)
v_x	Local image flow (velocity) vector in x direction	
v_y	Local image flow (velocity) vector in y direction	
x_i	Cartesian coordinate in x direction	
ρ	Density of the working fluid (air)	(kg/m^3)

μ	Dynamic viscosity	(kg/m.s)
υ	Kinematic viscosity	(m^2/s)
ω	Angular velocity	(rad/s)
τ_i	Stress tensor component	(N/m^2)

CHAPTER I

INTRODUCTION

1. Introduction on meso-scale cooling technologies

Recent innovations in electronics micro-fabrication technologies and demand for high performance devices in nearly every industry, lead towards a variety of challenging technological hurdles. The electronic devices are now faster, more efficient and have more computational and operational capabilities. These added values are achieved by the evolution of a very critical factor in the manufacturing. The applied chips are exhibiting more capabilities with the cost of generating higher heat fluxes as a result of more internal activities than previous chips. The complicated new designs mainly include more chip sets than before to satisfy the ever demanding market. The thermal challenge is to control the hot-spots by the proper system of thermal design, which includes the heat sweeping via a reliable method. The thermal solution should be implemented as a light-weight-low-cost thermal scenario.

The intrinsic nature of all possible techniques of cooling includes methods of removing the heat. The heat removal efficiency is the characteristic criteria while the ease of maintenance of manufacturing is also the other aspect of issue.

Cooling can be done by a number of methods. These methods can be divided into many categories based on various criteria. One common criterion is to divide the cooling methods into active and passive methods. The passive cooling generally includes heat sinks, heat pipes and fins. It is called passive since the heat sweeping is mostly done without the use of electricity and controlling chips. In these methods the natural convection is responsible for the removal of the heat.

The active cooling systems consume electricity while including dynamic parts. The axial fans, synthetic jets and the piezoelectric fans are some examples that are under the category of

active cooling. When active methods are being considered it is important to note the coefficient of performance of the device. This coefficient indicates the ratio of gained performance to the power the device is consuming. COP is a measure of how efficient a system is, in terms of the power consumption.

All of the factors mentioned above are the critical factors which should be considered to reach a reliable thermal solution. With the current variety in the thermal problems the solutions should also be flexible and sustainable enough so they can be also modified accordingly. In this study, three various forms of cooling has been studied experimentally and then as will be mentioned in the later chapters, one of them has been studied via the computational fluid dynamics (CFD) method for more insight into mechanism of cooling. The selected technologies are rotating fan, synthetic jet and piezoelectric fan.

These technologies are chosen based on their different approach on the concept of heat removal. Rotating fans simply exploit the blades capability to generate a forward flow which can sweep heat. Synthetic jets and piezoelectric fans through the sweeping flow remove heat with the aid of oscillation, each with a slight distinctive route.

In the following sections, each of the selected methodologies are being discussed and the details of each will be presented.

1.1 Rotating fan technology
A common route of exploiting a generated flow for heat removal is the fan technology. The common design is to drive the working fluid through the impeller. The induced flow is approximately towards the axial direction. Rotary fans usually have a high mass flow rate and a low value of pressure rise. Their ease of use made them the most common alternative in many applications. But with the advent of the new generation of devices, the need for a higher

performance, lower ranges of noise production, less space consumption and compliance with the green policies are crucially accentuated by all the researches in field [1].

Due to the empirical characteristic of the blade design before the advent of the computational methods, primitive way of selecting the proper blade design was based on the simplified two-dimensional, theory of the flow [2].The most important factors of the fan blade design are the empirical coefficient diagrams and vortex generation regime if the electrical motor-related characteristics are set aside.

An inclusive clarification for the fans based on their application has been done by Bleier [3]. In this study the standard testing techniques of AMCA alongside with the extended application of the fans has been provided in full detail. After the commercialization of the CFD through the empirical methods are being used only in the applications which precise flow related value monitoring is not of high importance. The contemporary usage of CFD enables the designer to modify, design and optimize the resultant flow of a fan with a higher degree of certainty while the need to conduct various cases of experimental tests are also somehow eliminated.

Figure 1: A typical axial fan [3]

Figure 1 presents a typical axial fan. The characteristics of a fan are commonly featured by a variety of physical quantities including static pressure, total pressure, flow, rate, rotation speed, motor input, and mechanical efficiency, static pressure efficiency, and sound level etc. The static pressure and the flow rate are mostly used as indices to characterize the fan performance.

These fans are also categorized by some of mentioned physical attributes. These are the designators of the induced flow. All of them are effective in the flow regime that the fan is capable of generating. On the other hand these quantities are also interconnected with the mechanical characteristics of the fan motor too. The efficiency of the fan motor dictates the possible range of the previously mentioned quantities. Before the use of the CFD methods, the most reliable method of design or selection of a fan was to use the performance curve. The performance curve depicts the relationship between the static pressure and the flow rate. Since in most of the practical cases these two values are approximately known, therefore, a selection or a design plan can be made based on them.

With the help of computational methods, nowadays it is possible to have a high precise prediction of various critical characteristics such as inter-blade flows and exterior flow fields within the inlet/exit of a fan.

The conventional methods of using CFD technique result in the prediction of the fan performance and flow details. The velocity and pressure distributions (contours, vectors and particle tracking etc.) are calculated using numerical schemes. The fan performance, i.e. the relationship between the static pressure and the flow rate, is subsequently extracted from the computational results. According to the used numerical schemes the results may vary, the needed computational time might differ as well as the convergence time. These methods have a reported accuracy level of around 80 %. [4].

The topics of interest in the numerical study of the fans mainly include the modifications of the turbulence models, the mesh and grid structure algorithms, boundary conditions, etc. The grid problem itself can be divided into two categories of static and moving grids. The moving grid is a problem which might seem easy to tackle but in the computational simulations the accuracy of the implanted movement is a critical manner. Currently the most used method in the fan problems is the use of the moving boundary condition which has its own bugs and errors. In order to achieve the high accuracy results the employed models should be complied with the experimental results to a high extent. Later on in the piezoelectric section, the moving boundary condition solution approach will be elaborately explained.

1.1.1 Muffin fans

The muffin fan is the small scale of the rotating fans. The mechanism is the same as mentioned in the previous section. The used muffin fan in this study is shown in Figure 2. The dimensions of this model, makes it capable of being used in small volume sizes. Some samples are also shown in Figure 3.

Figure 2: Muffin fan dimensions [5]

Figure 3: Sample of muffin fan application in cell phone [5]

1.1.2 The governing equations for the rotating fans

The three-dimensional fluid dynamics of the incompressible, Newtonian, and turbulent flow in an axial flow fan is generally described by the Navier–Stokes equations. These equations for the conservation of mass and momentum in cartesian tensor notation can be derived as follows:

$$
\frac{\partial}{\partial t}(\rho u_i) = 0
$$
$$
\frac{\partial}{\partial t}(\rho u_i) + \frac{\partial}{\partial x_j}(\rho u_i u_j - \tau_{ij}) = -\frac{\partial P}{\partial x_i} + s_i
$$

(1)

Where ρ the density of fluid is, x_i is the Cartesian coordinate, u_i is the velocity component of fluid in direction x_i, τ_{ij} is the stress tensor component, P is the pressure, and s_i is the momentum source component [5].

These can be solved numerically with many methods and the related literature about these are quiet an independent task itself though will be covered within the further steps.
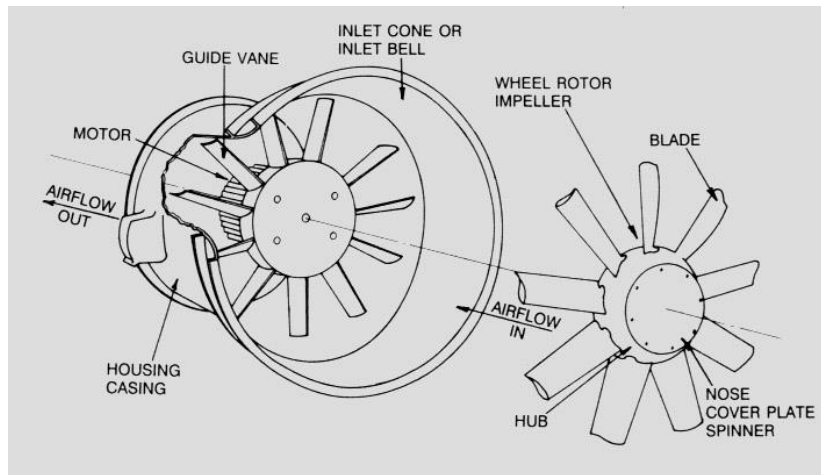
Figure 4: Details of a conventional fan [3]

Selection of a fan is an iterative procedure; each fan is basically designed for a certain system of air volume range and static pressure. So first based on the theoretical aspects of the working environment the pressure and air volume is calculated. Once these values are approximately found, then the next step would be to choose the dimensions and select according to their possible place of attachment.

Axial fans are designated with their flow direction, which is along their axis. The axis of the rotation is the direction in which the flow is moving. Then the flow reaches the blades, and it will be deflected by them, as shown in Figure 4.

The operating principle of axial-flow fans is simply deflection of airflow into helical path. This is the governing mutual fact about all three types of axial-flow fans: propeller fans, tube axial fans, and vane axial fans. Since the pattern of deflected airflow is known, the design procedure and the needed first hand calculations are quiet similar for all the previously mentioned types of the fans.

The helical pattern of the flow can be divided into two separate components of flow, one is an axial velocity and the other is the tangential velocity. The needed components which are the key feature of the flow velocity are the main concerns [5].
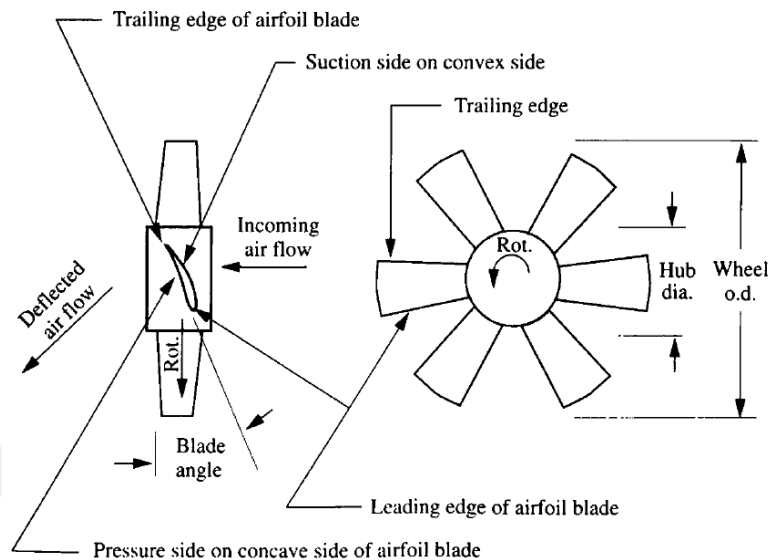
Figure 5: Airfoil in an axial flow fan blade [3]

As the schematic of the fan is shown in the Figure 4 and Figure 5, the blades are in shape of airfoils. The two main category of the fan blades/airfoils are symmetric and asymmetric airfoils. For the case of the fan blades the commonly used airfoil is the symmetric type, unless especially designed models for the unique cases.

As the airfoil/blade is being submerged in the target fluid- in this study air-it produces a positive pressure. This positive pressure is being exerted on the lower area of the airfoil; accordingly there is a negative pressure on the top area. The negative pressure exerts a suction pressure on the top area; this suction pressure is as twice larger as the positive pressure on the lower area. Although there is a magnitude gradient, all these pressures (push and pull in a manner) eventually reinforce one another.

The combination of the mentioned pressures, make the force that is designated as force F. F is fragmented to two components of force, a lift force, perpendicular to the air velocity. The other component is the drag force. Drag is parallel to the relative air velocity [5].

1.2 Synthetic jets

Having a reasonable junction temperature at the various engineering systems is a critical problem in industry. This need accentuates the importance of novel cooling methods with higher heat transfer capabilities than previous techniques. One option might be the usage of impinging jets. The innovative version of the mentioned jets is a synthetic jet with a piezoelectric actuator [6].

Synthetic jet is a flow inducement method in which the stagnant air is used to form a cooling flow [7]. In the synthetic jet the fluid flow is generated by the oscillation of a piezo diaphragm [8].

Synthetic jet is made by a period suction and blow of the flow, this form of periodic behavior can be made by an acoustic speaker, piezoelectric diaphragm, ferromagnetic and moving piston cylinder mechanism, etc. [6,7,9,10] (shown in Figure 8).

The most crucial aspects of the synthetic jets which have been studied extensively can be categorized in the fields of controlling the flow, turbulence in boundary layers, and heat transfer applications. For the case of heat transfer the synthetic jets can be used directly as an independent cooling device or as a modifier of another cooling device by the formation of vortices.

The synthetic jet mechanism is fundamentally based on the oscillation of the piezoelectric diaphragm. The given voltage to the piezoelectric diaphragm make it oscillate. The oscillation induces pulses of rapid turbulent air flow. The high speed velocity pulls the air in the process; this type of flow inducement increases the overall flow by approximately 5 times.

The heat sink heat transfer is improved by the turbulent flow (induced by the jet), the trapped air increases the rate of the exiting heat sweep, and whole process altogether improves the efficiency (Figure 8) [11].
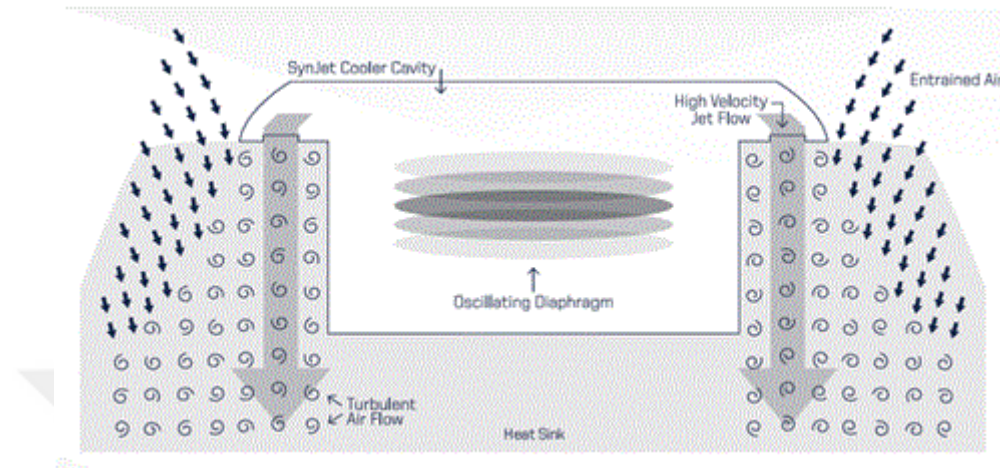
Figure 6: Schematic operational mechanism of a synthetic jet [6]

1.2.1 Augmentation of heat transfer with synthetic jets

Jet impingement is capable of impinging high rates of flow. Pavlova and Amitay [10] experimentally investigated the cooling of a constant heat flux surface and compared the performance of synthetic jet with the continuous jet. Based on their findings the cooling performance of the synthetic jet is significantly higher than continuous jet at the same Reynolds numbers. Arik [8] studied the local and global heat transfer coefficients with high-frequency synthetic jet impinging on a flat surface. At the resonance frequency of 4500 Hz, it is observed that the heat transfer coefficient values were higher between 4 to 10 times than the natural convection values.

1.2.2 System design and concepts

The conventional synthetic jet (here the reference is the Nuventix Jet sample) consists of components depicted in Figure 9.

The blow and suction system consists of a diaphragm for producing the air flow. The oscillation of the diaphragm pushes a pulse of air out side of the nozzle. The pulse of air is

violently ejected and propelled a significant distance away from the nozzle. As the pulse is being ejected from nozzle, the velocity gradient causes a secondary flow to form, causing the resultant flow to be of turbulent nature. Plane turbulent jet is synthesized by the interactions between pairs of counter-rotating vortices. The vortices are produced at the edge of the orifice (See Figure 9).
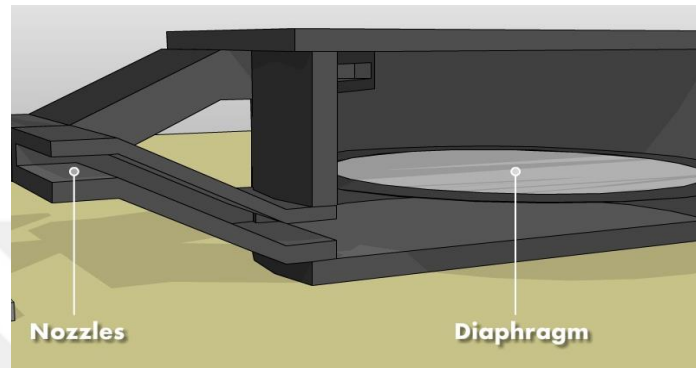
Figure 7: Synthetic jet configuration [6]

The blow and suction system consists of a diaphragm for producing the air flow. The oscillation of the diaphragm pushes a pulse of air out side of the nozzle. The pulse of air is violently ejected and propelled a significant a significant distance away from the nozzle.

As the pulse is being ejected from nozzle, the velocity gradient causes a secondary flow to form, causing the resultant flow to be of turbulent nature. Plane turbulent jet is synthesized by the interactions happening between a pair of counter-rotating vortices. The vortices are produced at the edge of the orifice (See Figure 9).

There is a secondary flow which is generated as the surroundings air is entrained due to the primary high momentum pulse. This secondary entrainment is responsible for up to 10 times the air flow through the heat sink than that of coming out of the nozzle (See Figure 10).
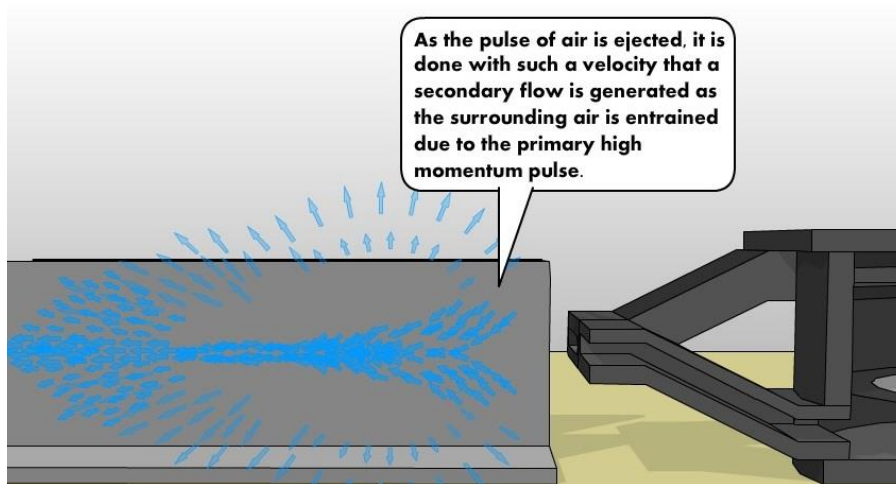
Figure 8: Secondary flow visualization [6]

Once the initial pulse is being ejected away from the nozzle, the ambient air is pulled in due to the movement of the diaphragm. The jet flow generated with this method is unsteady and turbulent. A series of vortex rings are inside this flow that enables the flow to have higher heat transfer coefficients. A jet flow is formed at the edge of the orifice, due to the periodic motion of the diaphragm. This diaphragm is usually mounted on one of the walls of a cavity (Figure 9). When the diaphragm moves in the direction of the orifice, a vortex ring is formed at the edge, and it moves away with its own self-induced velocity such that when the diaphragm moves away from the orifice. This is the reason why this type of jet has a zero net mass flux per each cycle of operation.

The effect of the synthetic jet is only accentuated in the close distances; this means in the far field the created jet flow is similar to a conventional two-dimensional jet if being considered in the time averaged frame of view [12].
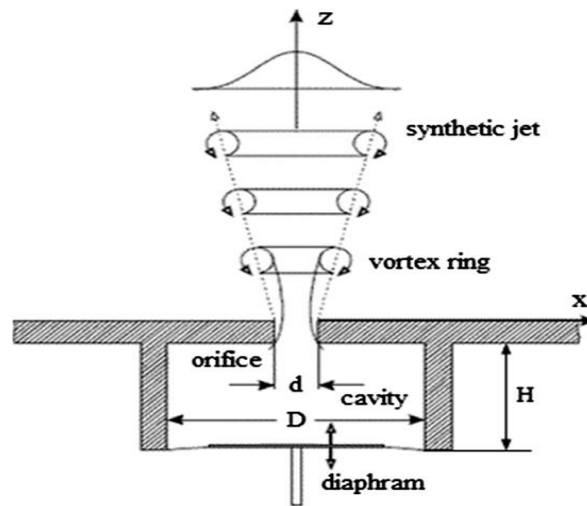
Figure 9: Schematic of synthetic jet actuator [2]

1.3 Piezoelectric fans

Thermal management of electronics is a field in which innovative approaches are essential. Electronic devices are now smaller while their computational power is significantly higher. As a result of recent advances, the heat generation from the electronic chips is confined in smaller volumes. This heat should be removed so that the electronic devices can perform reliably and meet the functional needs.

One innovative approach for heat removal is the use of an oscillating cantilever beam as a flow inducer. The most commonly used device is the piezoelectric fan. The piezoelectric fan is a low-power consumption fan that uses an applied electric voltage to produce material deflections and oscillations. Due to its simple mechanism and its promising initial performance, it may be an effective solution for electronics cooling systems. Piezoelectric fans generate flow by the oscillation of their slabs. The piezoelectric patch operating with alternating current moves the slab periodically. This movement is the origin of the flow generation. The fan consists of a piezo actuator and a slab (Figure 10). The slab is assumed to be a cantilever beam in the modeling [18]. A cantilever beam is normally anchored only at one end [15,19,20].

The pioneering studies on the use of piezoelectric fans were done by Liu et al. [13]. These demonstrated the importance of the orientation of the fan tip, as the fan could be placed in front of the desired heat source in a vertical or horizontal manner. The vertical orientation produced an asymmetrical flow field distribution, while the horizontal orientation was more symmetric. This was due to the asymmetric entrainment of the flow in the vertical configuration.

Arik et al. [14] examined the piezoelectric fan when coupled with a heat sink. This study indicated that metallic piezoelectric fans might have a considerable coefficient of performance. Acikalin et al. [15,16] studied an optimized design for the piezoelectric fan by changing the fan tip geometry. This research group studied the dynamics and topology optimization of piezoelectric fans further [17]. This is a challenging issue, as the nature of piezoelectric fans involves a fluid-structure interaction (FSI). In most studies, FSI is not considered in the solution method due to simulation difficulties.

Toda et al [5] initiated the study on the piezoelectric fan and enhancement factors in the heat transfer. Their simplified models for the vibration and the flow field alongside with the heat transfer showed promising enhancements for the use of the piezoelectric fans as a cooling method. In some studies, it has been also noted that the generated flow can cause minor oscillations in the target structure such as heat source. This phenomenon was not observed in the current study, thus the effect has not been considered [15]. Kimber et al [18] showed the shedding of the vortices from the edges of the cantilever beam. Vortex symmetry phenomenon was observed. Flow field contours and pressure coefficients were reported alongside with the phase dependent depiction of the induced flow. The vortex shedding can be anticipated by the use of the Keulegan–Carpenter *(KC)* number. As discussed in [18], low range of the Keulegan–Carpenter number can be assumed to have the value below 10.

Equation 2 shows the *KC* number in which *A* is the amplitude of the oscillation and *C* is the characteristic length of the structure undergoing oscillation.

$$KC = \frac{2\pi A}{C} \tag{2}$$

$$St = \frac{fL}{U} \tag{3}$$

The measured amplitude of oscillation for the mylar piezoelectric fan is about 1.5 cm. Equation 3 indicates Strouhal number, where *f* is the frequency of vortex formation, *L* is the width of the piezoelectric fan tip (see Figure 10) which is the characteristic length and *U* is the main stream velocity.

In this study the *St* number associated with the piezoelectric fan operation is categorized as low [21] . Low value of St, means the flow can be considered steady state. The vortices formation regime is not affecting the steady state condition. The conclusion can be stated in terms of vortex formation frequency. Low St number suggests that the frequency of formation of the vortices is also low. The vortex formation does not bother the flow near the heat source, thus the heat removal is done by the direct effect of the vortices; which are generated by the piezoelectric fan.

The *KC* number is estimated to be around 7.85, which is considered to be low as discussed in [18]. *KC* number indicates the distance that a fluid particle can depart from the tip before the moment when the fluid direction is being reversed. This can determine the size and the strength of the vortices [17], [22]. Low KC indicates that the vortex cannot travel far away thus; the formation of vortices can only be expected in the close distances and in small diameters. The effect of oscillation amplitude on heat transfer has been explored by Yang [5]. The higher amplitude of the oscillation results in more heat sweep. The metallic piezoelectric fan exhibits a higher oscillation amplitude and deflection resulting in a considerably higher

heat transfer coefficient. The same behavior has also been reported for the frequency of operation for the piezo fans by Yang [5]. The coupling capability of the piezoelectric fan with another passive cooling method such as the use of a heat sink is studied by Petroski et al. [14]. Petroski's study highlights the ability of accentuating the natural convection with a flow induced by a piezoelectric fan.
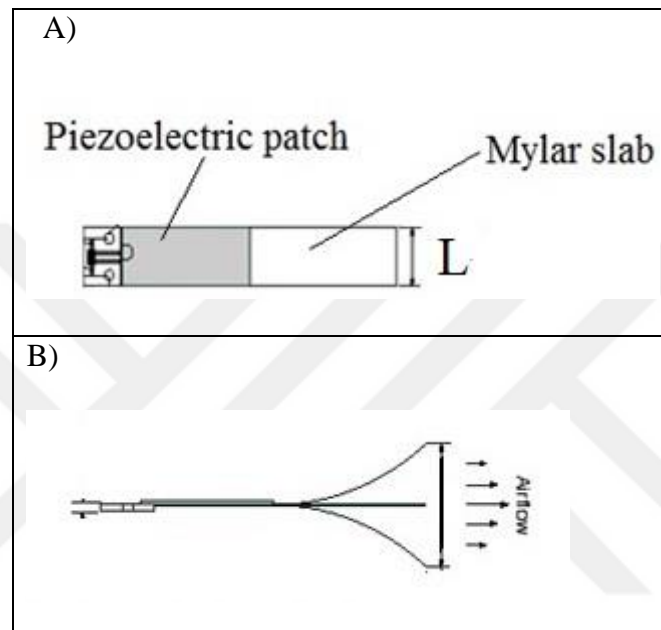
Figure 10: A) Schematic view of the piezoelectric fan, B) Cross section of an operating fan-depicting deflection [9]

Table 1: Summery of the literature review on piezoelectric fan

Heat transfer related variable found in literature review	Reference
Simplified 2D model of the beam	Toda et al.(2002)
Topology optimization, dynamic study of the beam, fluid-solid interaction (FSI)	Burmann et al.(2002)
Fan tip geometry	Acikalin et al .(2007)
Assumption of the slab as a cantilever beam (for the dynamical consideration of the beam)	Kimber, Sudipta and Berg et al.(2009)

Orientation (Horizontal/Vertical)study on the fan	Liu et al. (2009)
Flow distribution, asymmetric or symmetric, 3D or 2D	Liu et al.(2009)
Vortex shedding mechanism	Kimber et al.(2009)
KC/St number investigations	Bidkar, Sobey et al.(2009)
Effect of oscillation amplitude on the heat transfer characteristics	Yang et al.(2009)
Piezoelectric coupled with passive heat transfer devices (heat sink)	Arik et al.(2010)

 A summary of the piezoelectric fan critical concepts is provided in Table 1. Based on the above mentioned literature, it has been decided to reduce the problem of the study for the piezoelectric fan to 2D, so that in the numerical modeling less complexity is needed to be tackled. The assumption of a cantilever beam is considered in the macro code that is implemented in the oscillation of the slab in the simulations. (Details are elaborately defined in Chapter 2 and Chapter 4).

1.4 Summary

In this chapter a brief literature review is presented for rotating fans, muffin fans, synthetic jets and the piezoelectric fans. In chapter two the experimental results of the heat transfer tests for each of these technologies is provided. Chapter three is dedicated to flow visualization, the tested techniques and the results of each is presented. In chapter four, numerical simulation of the piezoelectric fan is discussed. In this study after the experimental phase, the emphasis of the investigations is set on the piezoelectric fans; this is due to their novelty and the nature of their heat transfer regimes. The details of the vortex generation phenomena and the related heat transfer results are elaborately discussed in chapter four.

Table 2: Various types of cooling categorized by the cooling device

Technology	Heat sweeping characteristic (Flow characteristic)	Heat transfer mode	Maximum heat transfer coefficient (W/m^2-K)
Muffin(rotary) fan	Vortex street made by the blades rotary movement	Forced and natural convection	12
Synthetic jet	Produces vortex rings from the orifice	Forced convection	70
Piezoelectric fan	Produces vortices mainly from the fan tip, depending on the oscillation of the slab	Forced convection	57

In order to organize the data gathered from the literature review a summary of the different types of cooling designators for each technology is provided in Table 2.

1.5 Motivation of the present study

This project is investigating novel air-cooling thermal technologies. Three technologies have been selected to be investigated based on their cooling capabilities. These technologies are synthetic jet, piezoelectric fan and muffin fan. Each of the mentioned technologies deploys a different method of cooling. The cooling is done by a form of flow inducement. This flow is generated within different methods in piezoelectric fan, synthetic jet and the muffin fan.

After the first set of experimental tests, it was observed that all the three mentioned technologies depict high degree of dependence, on the variable of distance. Distance from the heat source, affects the achieved heat transfer values in all of the cases. For the cases of the piezoelectric fans and synthetic jets the behavior of the flow regimes did show some interesting attributes. So after witnessing this; study was focused more towards understanding

the flow aspects such as vortex formation/decay. In order to have a clear understanding of piezoelectric fans, numerical simulations are proposed to be done in this study. After performing the simulations with the use of the ANSYS-FLUENT software, another phase is added to this study; the visual investigation of the flow behavior around the piezoelectric fans. The motive of the visual investigation is to understand the real time flow behavior with the help of a high speed camera. So with the help of the numerical analysis and visual analysis a comprehensive study was designed and done.

CHAPTER II

EXPERIMENTAL STUDY

Understanding the heat transfer characteristics of various cooling devices was the first phase of the ASEST project. In order to measure heat transfer related quantities, experiments was designed and performed. In the following chapter the details of the experimental test set up and the methodology of data acquisition is presented. Later on, the acquired data is presented alongside with the preliminary conclusions. The experimental data will be compared with the numerical simulation results in chapter 4.

2.1 Heat transfer set up

An experimental test system was designed and built to measure the three distinctive meso-scale cooling devices including synthetic jet, muffin fan and piezoelectric fan's heat transfer performances.

Table 3: Equipment used in the setup

Device	Company-Model
Data acquisition	Agilent-34972A
AC power supply	Agilent-6811B
DC power supply	Agilent- E3634A
Thermocouple	T-type/OMEGA
Synthetic Jet	Murata Co.
Piezoelectric fan	Mylar-Piezo Co.
Piezoelectric fan	Metallic- Piezo Co.
Muffin fan	Sunnon Co.

In order to measure heat transfer, the set up consisted of heater (acting as the heat source), cooling device and the data acquisition apparatus. Investigation of heat transfer characteristics is based on the temperature difference, caused by each device. The heater surface temperature was held fixed in the experiment sets, while the cooling device distance from heater and operational voltages were the independent variables. The temperature of the heater surface was kept constant at 60 °C. Heater temperature was controlled by a DAQ device.

The whole test rig was mounted in an enclosure so the heater and the cooling device would be isolated from possible environmental effects during the test (See Figure 14).

The list of the complete equipment, used in the setup is shown in Table 3. The setup parts can be divided into two categories. First category is the data acquiring system. This includes the data acquisition device and the thermocouples. Temperature of the areas of interest were measured with the thermocouples and recorded by the data acquisition device.

The second category is the cooling devices. The devices are supplied with the needed power (AC or DC). These power supplies show the voltage and current values. The values were recorded and they will be depicted in the next section of this chapter.

A)

Labels: test set up closure; Data acquisition device; Temperature monitoring software; AC power supply; DC power supply

B)

Labels: mylar piezoelectric fan; metallic piezoelectric fan
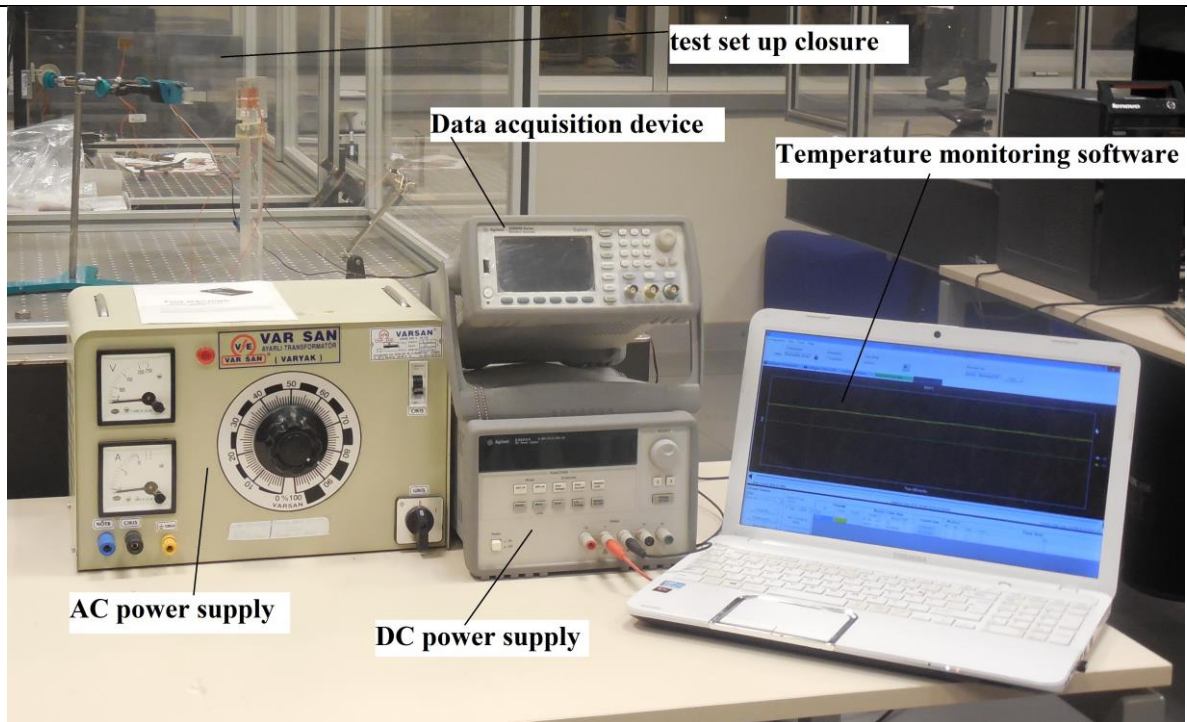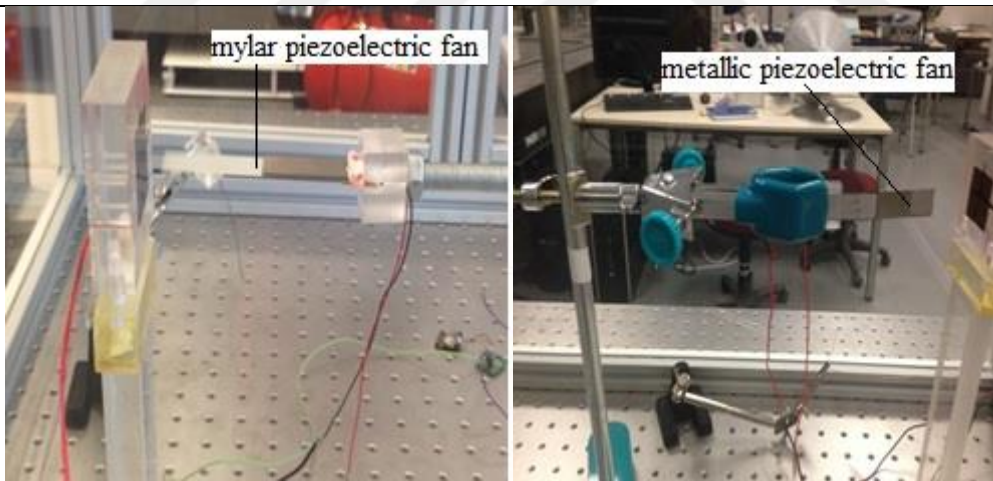
C)
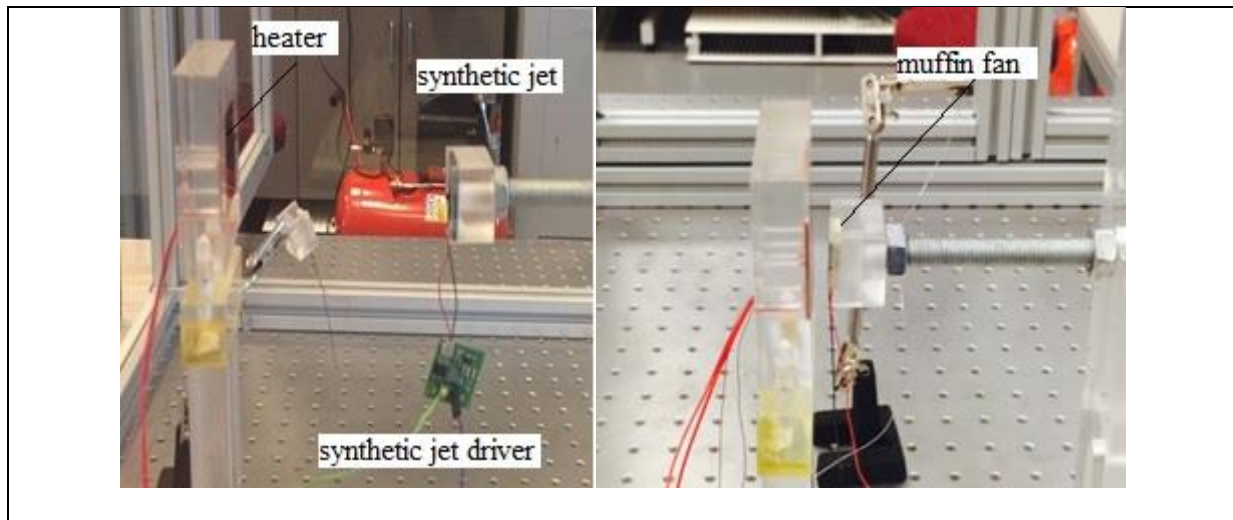
Figure 11: Test set up including A) Power supply and data acquisition,

B left) Mylar piezoelectric fan set up, B right) Metallic piezoelectric fan set up,

C left) Synthetic jet set up components, C right) Muffin fan set up

2.2 Heat source (Heater) specification

2.2 .1 Heater design

Heater's surface temperature should be set at a constant value. Thus, the average temperature of the copper plate should be monitored to achieve the desired value. Three T-type thermocouples are located at the back of the copper plate for the temperature acquisition. The detailed microscopic images are shown in Figure 13. The Figure 13 images are captured with the Hirox-KH microscope which is shown in Figure 12.

In order to create the heat source, a 25mm_25mm Kapton heater was placed at the backside of a 1.5mm thick copper plate, which was also equipped with three T-type thermocouples, as illustrated in Figure 13. Three T type Thermocouples connected to a DAQ (Agilent data acquisition systems). The average of temperature of these sensors defined the heater surface temperature. DAQ showed the trend of the temperature fluctuation. The data should be recorded while the steady state is reached. Steady state was assumed to be achieved if the fluctuation of the monitored values was less than 1 percent.

Figure 12: HIROX KH7700 microscope used for the heater surface evaluation

Figure 13: Thermocouple configuration under the microscope

2.2.2 Heat loss calibration- Guard heater test

It is evident that the designed heater would have some losses due to its lateral areas. The heat losses should be measured, otherwise they will be included in the cooling device performance. This will cause error. Thus the study of heat losses is of high importance.

The applied approach for evaluating the heat loss was the use of a guard heater. The concept was to reduce the surface heat transfer, to an approximate zero. This could be done if the heater front was blocked by another surface with the same temperature. In order to did so, an identical copper heater was placed in front of the heater. The nearly zero temperature difference lets no heat flux from the surface. In this configuration, the heat flux was assumed to be mainly due to the lateral conduction heat losses, from the designed Plexiglas housing.

2.2.3 Heat transfer calculation procedure

The cooling device was mounted on a beam that supports it in a Plexiglas fixture that let the device operate close to the surface area of the heater. The cooling device was located at different distances to study the effect of the distance.

Tests were started by turning on the power supply, and allowing the enclosure to achieve steady state condition, and then the data collection began. Otherwise, the data would not be accurate and might include a high percentage of error.

The heat generated from the surface of the heater was the heat dissipation that should be checked by each of three considered cooling technologies. The heat balance on the surface of the heater reveals the terms that have significant effect on the total heat generation. Here at this point the effect of the radiation was assumed to be insignificant, thus it was neglected.

$$Q_t = Q_{natural-convection} + Q_{conduction} + Q_{coolingdevice} \qquad (4)$$

The performance of each cooling device was dependent on the amount of its heat removal. As stated before the heat losses which were mostly due to the lateral conduction of the Plexiglas housing should be addressed for calculation of the net heat generation.

$$h_f = \frac{Q_{net}}{A * (T_s - T_\infty)}$$ (5)

As many fluid mechanics problem which include many parameters that contribute to the considered variable, it is favorable to implement and use dimensionless numbers which are extracted by the use of the Pi (Buckinham) theorem [23]. List of applied dimensionless numbers in this study are shown in Table 2.

Table 4: Dimensionless numbers of this study

Dimensionless number	Designation	Formula	Description
Reynolds number	Re	$Re = \dfrac{\rho v L}{\mu}$	The primary parameter correlating the viscous behavior of all Newtonian fluids
Nusselt number	Nu	$Nu = \dfrac{h_{coolingdevice} D}{K_{air}}$	Indicating the ratio of forced to natural convection.
Oscillatory Reynolds number	Re$_{osc}$	$Re_{osc} = \dfrac{A \omega C}{\upsilon}$	Viscous behavior of the Newtonian fluids, used in the problems involving oscillational fluid-structure

| Strouhal number | St | $St = \dfrac{fL}{U}$ | Describing oscillating flow mechanisms |
| Keulegan–Carpenter number | KC | $KC = \dfrac{2\pi A}{C}$ | Describing the relative importance of the drag forces over inertia forces for objects in an oscillatory fluid flow |

For the sake of simplification, some geometric dimensionless numbers are also used. These numbers are shown in Table 3.

Table 5: Distance designation parameters

Dimensionless number	Description of parameters	
H/D	H	Distance between synthetic jet/muffin fan and heater
	D	Muffin fan diameter /synthetic jet nozzle
G/A	G	Distance between piezoelectric fan and heater
	A	Amplitude of oscillation
$4A_{area}/P$ (Hydraulic diameter)	A$_{area}$	Approximate cross section area of

		the enclosure
	P	Affected (wetted) perimeter of the cross section

The tests were carried out at the predefined conditions and the performance of the cooling devices was measured in terms of the COP, Nu and heat transfer coefficient for each cooling device. In the next section the experimental results for each device results will be shown.

The main change in this system was the change of the H/D and G/A ratio to study the variations in the heat transfer characteristics.

2.4 Experimental results

2.4.1 Test results for muffin fans

The designed test set up for muffin fan is shown in Figure 14. The fan to heater distance was adjustable. This distance was reported using a non-dimensional number designated as H/D. Where H is the distance between the cooling device and heater, D is diameter of the fan. Four distinctive H/D values were tested to study the effect of distance on the performance of the muffin fan.

Operational condition of the muffin fan was at its highest possible range according to the device manual. The given voltage was 3 Volts. Figure 15 depicts the Nu number for the muffin fan. As expected based on the nature of the rotating fans, there is reverse relation between the distance and Nu. This means that the fan is the most effective at the close distances.
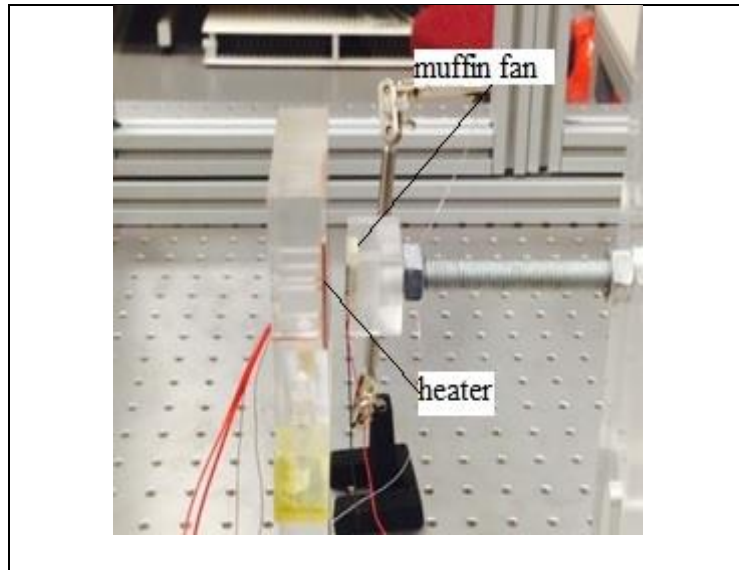
Figure 14: Set up for muffin fan tests

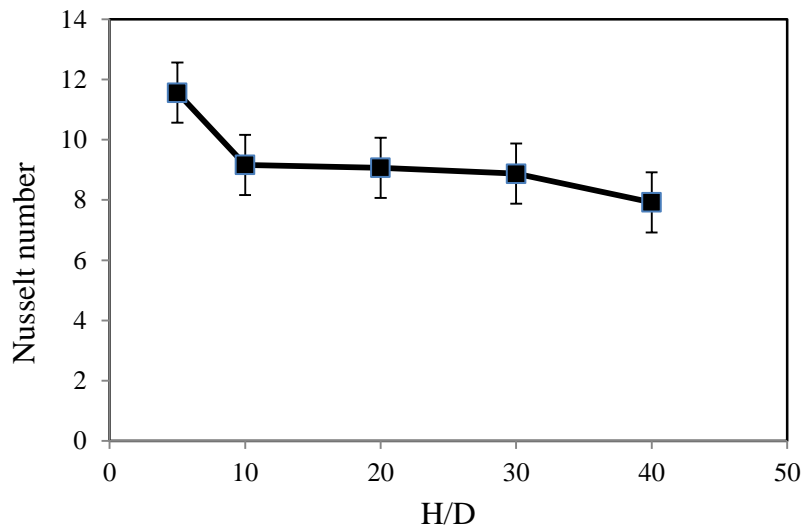Figure 15: Nu number variation for muffin fan

The highest observed heat transfer coefficient was $12W/m^2$-K. There is a sudden decrease in the heat transfer coefficient as H/D increased. This is in accordance with the Nu trend, which is depicted in Figure 15.
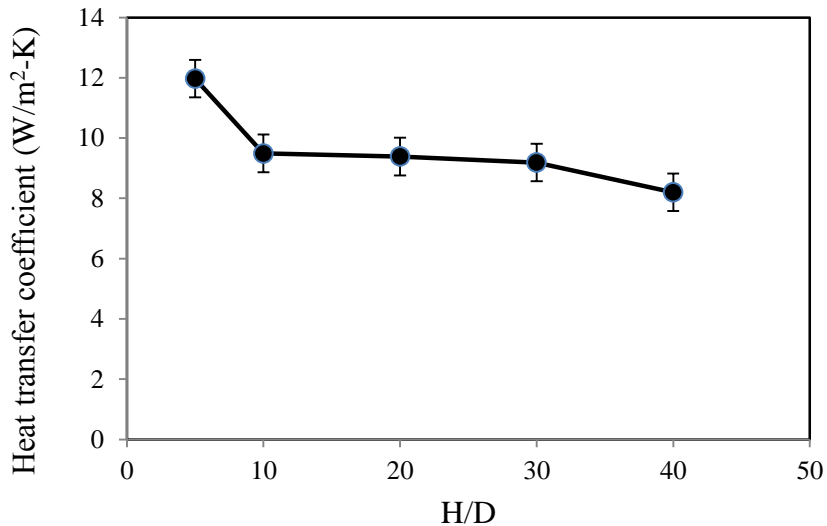
Figure 16: Heat transfer coefficient distribution

Figure 16 shows the heat transfer coefficient distribution for a muffin fan, the sudden reduction after the H/D=5 is evident and it is another proof for the fact that the flow induced by these fans were not strong enough to travel away more. The heat transfer coefficients after this distance were in the range of the natural convection; which means if H/D>5 then the fan operation is not affecting the heat source at all.

It is evident that with the current design of the muffin fan, including the blade and dimensions; the peak performance is expected to happen at very close distances as the COP results show (Shown in Figure 17). This means the fan should be mounted at the closest possible distance from the heater so it can perform an optimal heat removal. This is good for the places where there is no limit for the device placement. Although with the current trend in the electronics this approach is no longer an option. Coefficient of performance is also expected to follow the declining pattern as Nu and heat transfer coefficient. This is shown in Figure 17. The range of COP is lower than 1. In other words the muffin fan with the predefined geometry will not be technically suitable to be used as a cooling device in distant.
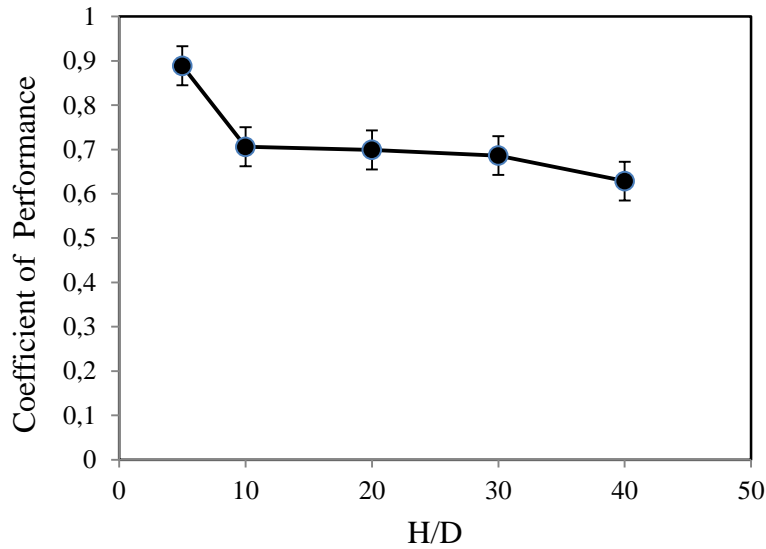
Figure 17: COP measured over the controlled distance

2.4.2 Test results for high frequency synthetic jets

Synthetic jet is operated using a driver, which controls the current input to the jet. The synthetic jet was operated in the range from 5 to 9 Volts, DC. The synthetic jet working mechanism is fairly different from the rotary fans and the piezoelectric fans. In the following, results of investigation on the effect of distance within various operational voltages will be presented.
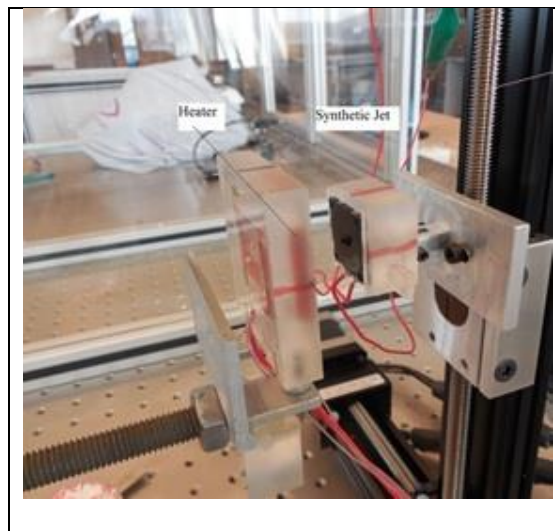
Figure 18: Test set up configuration for synthetic jet

Figure 19: Nu number variation with dimensionless axial distance for the synthetic jet

The variation of Nu with different distances for the synthetic jet is exhibited in Figure 19. As it has depicted the Nu has a peak at the H/D of 40 which is not at the close distance. This shows that the flow regime is in a way that it takes time to be most effective.
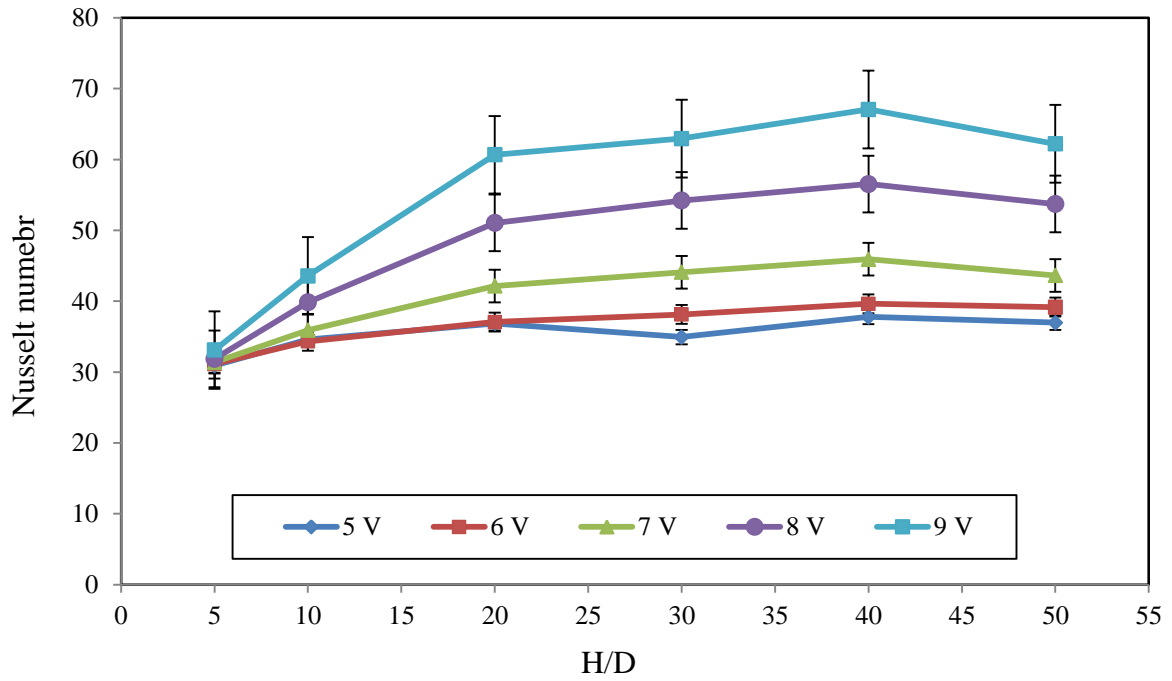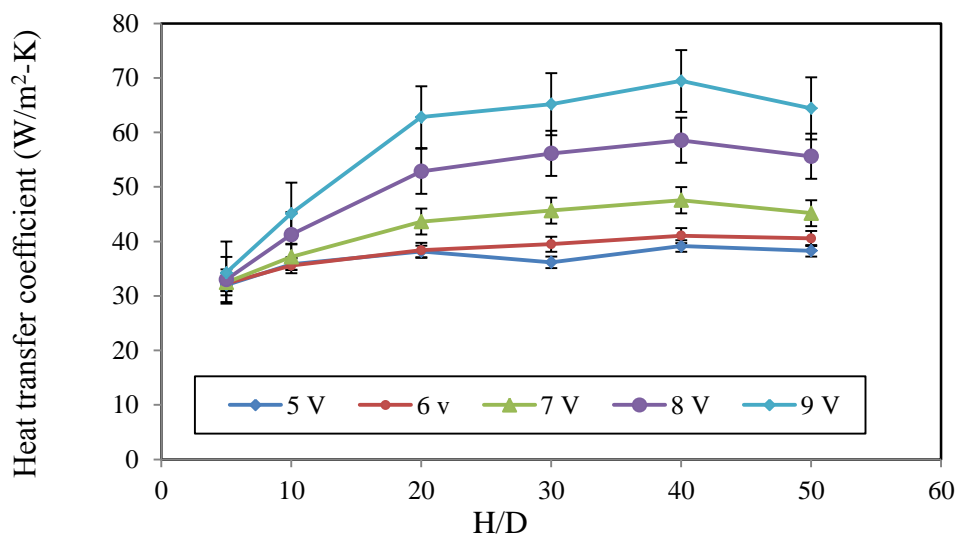

Figure 20: Synthetic jet heat transfer coefficient
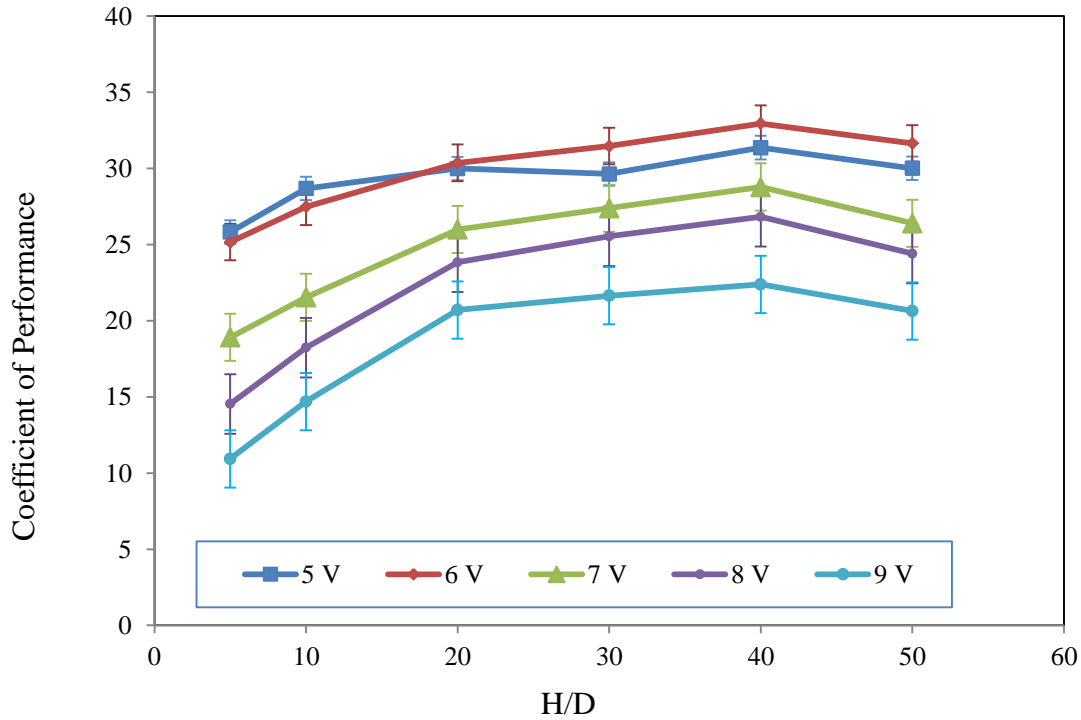
Figure 21: COP variations for synthetic jet

The heat transfer coefficient also follows the same pattern of the Nu as shown in Figure 20. This phenomenon has been studied before [24]. This is due to the vortex formation, which travels away from the nozzle and then improves the heat sweep at the target. The effect of vortex formation is studied fully elsewhere [24]. Figure 21 shows the variation of COP for the synthetic jet. Complying with the previous figures, the COP also indicates a peak value at H/D=40. After this point the COP drops thus there is only one optimum point of operation for the synthetic jets. This point for the specific tested jet is happening at H/D=40, but for the different types of the jets this value should be empirically acquired. The conclusion is that for the case of the synthetic jets, the behavior is not consistent as a trend. There is an increasing state till the peak. After that state there is decay in the heat transfer.

2.4.3 Test results for piezoelectric fans

Piezoelectric fan is an oscillating cantilever beam that induces flow to sweep heat and cool the targeted heat source. The ability of the piezoelectric fan to cool depends on the amount of the

beam deflection. This presumption has been proven to be correct by the experiments done on two different types of the piezoelectric fans. The studied piezoelectric fans are made from two types of materials. One of the tested piezoelectric fan's blades is made from mylar and the other one has a metallic blade.

2.4.3.1 Test results for metallic piezoelectric fan

The metallic piezoelectric fan was tested following the same procedure used for the previous cooling devices. In the case of piezoelectric fans, the distance is not presented with a non-dimensional number. The distance is directly reported in millimeters. The setup is shown in Figure 22. The fan was placed in various distances to understand the heat transfer characteristics. The aim of these tests was to investigate the effect of distance on the heat sweeping method of the fan. The effect of distance on the vortex formation quality, Nu and the heat transfer coefficient are shown in the following figures.
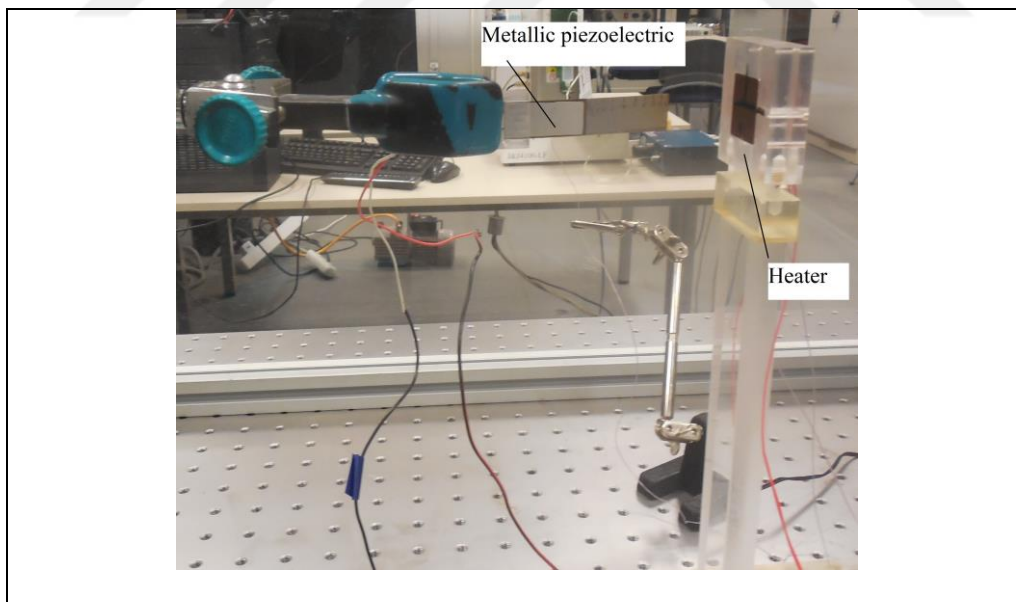
Figure 22: Metallic piezoelectric fan test set up
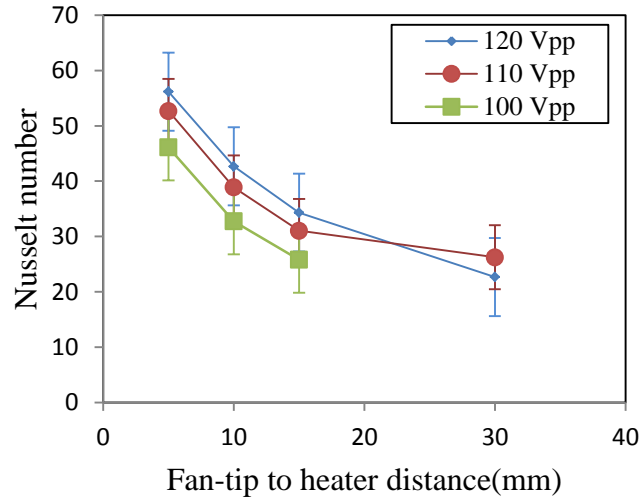
Figure 23 : Nu number for metallic piezoelectric fan

The effect of the distance on the Nu is shown in Figure 23; the best results were achieved at the minimum H/D. Nu number was drastically decreased by increasing H/D. It can be concluded that the vortices made by the fan from its oscillation cannot reach the heater at the high H/D thus the fan is not suitable for the places where the heat source may be away from the location of the fan.
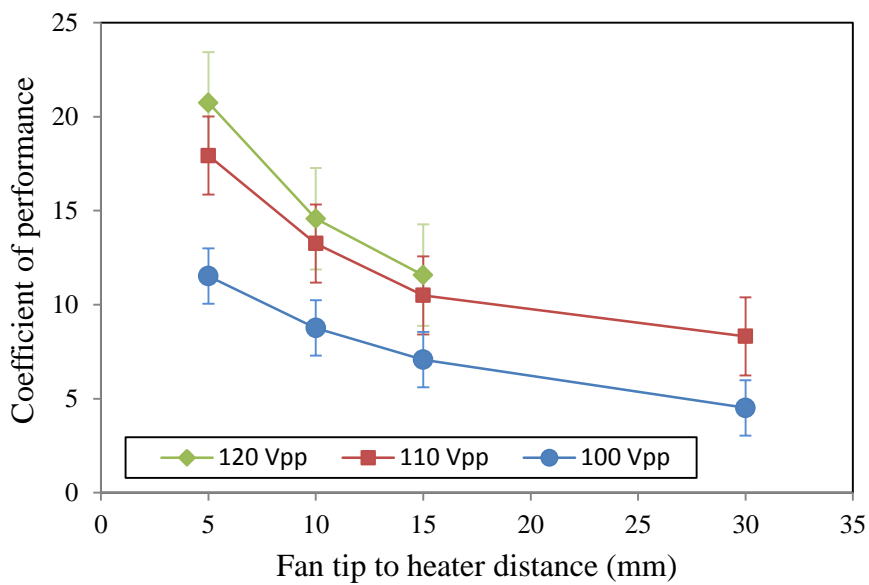
Figure 24: COP of metallic piezoelectric fan

The performance of the fan suffers, while the device is placed at the distance higher than 15 mm away from the heat source. Though the maximum performance achieved at the 5 mm distance is quite satisfactory (Figure 24).
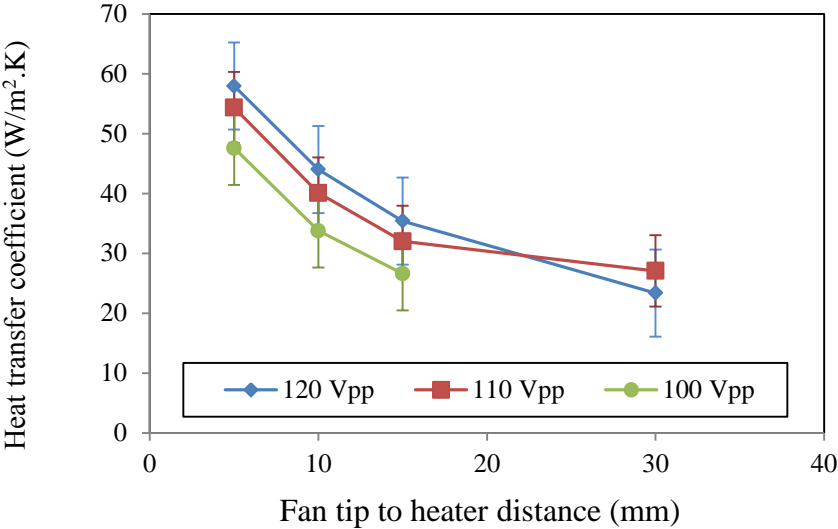
Figure 25: Heat transfer coefficient of metallic piezoelectric fan

In the case of the piezoelectric fan, there is no peak/optimized point seen as there for the synthetic jet. The mechanism of the vortex formation is quite different in the case of the piezoelectric fan. This is clear from Figure 24 and Figure 25. The vortex generation in the case of piezoelectric fan is in a way that the formed vortices are not capable of traveling far away from the tip of the fan. The heat transfer is declining as the distance is increased, as seen in Figure 25. If being compared with Figure 20 it can be concluded that the flow induced by the piezo is acting more like a common rotary fan rather than a synthetic jet. The oscillation of the slab is expected to have a modifying effect on the heat sweep since the maximum heat transfer coefficient is near 60 (see Figure 25), which is nearly 5 times more than what is achieved with the muffin fan. (see Figure 16). In the case of piezoelectric fan, the oscillation amplitude is a factor with high contribution in the heat sweep. Thus, in the following section another type of slab material will be examined.

2.4.3.2 Test results for mylar piezoelectric fans

The mylar piezoelectric fan exhibits a lower deflection. It is used as a test apparatus to observe the heat transfer for a lower range of oscillation. The expectation is to observe a lower heat transfer coefficient. As seen in the Figure 26 the maximum Nu of the mylar fan is approximately 20 while for the metallic fan this number is 56. Clearly the deflection is a factor that can extremely affect the heat transfer. Though in terms of practicality the mylar fans exhibits a more flexible configuration and the slabs do not undergo unwanted deflection.

As seen in Figure 27, the heat transfer coefficient has the same behavior of decreasing with distance. The distance that the generated vortices are capable of traveling for mylar fans is not far away. The heat transfer coefficient associated with the natural convection is usually around the margin of 9 to 10 W/m^2-K. In Figure 27 it is seen that at the distance of 15 mm away from the heater the fan is no longer effective.

Nu for the metallic piezoelectric fan is 56 while as exhibited in Figure 28 at the same point the value for the mylar piezoelectric fan is approximately 20. This decline is the result of the lower range of deflection. Mylar piezoelectric fan deflection is 50 percent less than the metallic fan. Lower deflection concludes slower vortex formation and less heat sweep. This concludes that for the case of mylar slabs some innovative methods should be approached to improve the deflection of the slab with the same material.
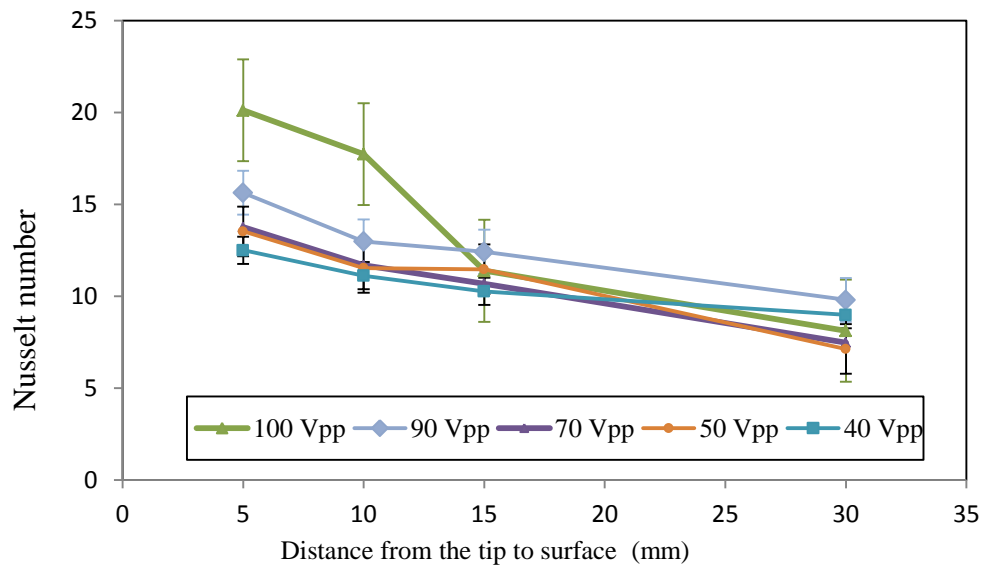
Figure 26 : Variation of Nu number versus fan to heater distance for mylar piezoelectric fan
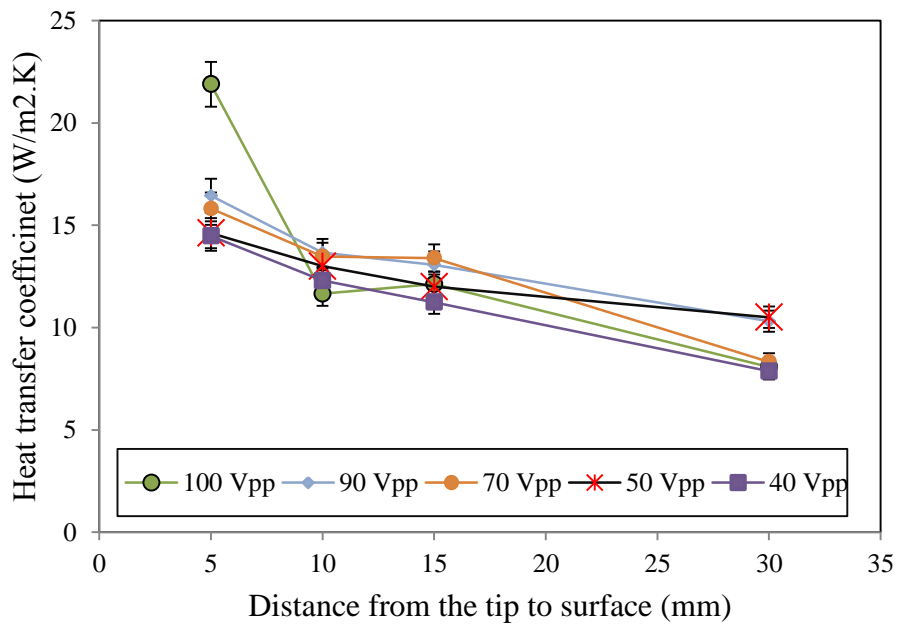
Figure 27: Heat transfer coefficient distribution for mylar piezoelectric fan
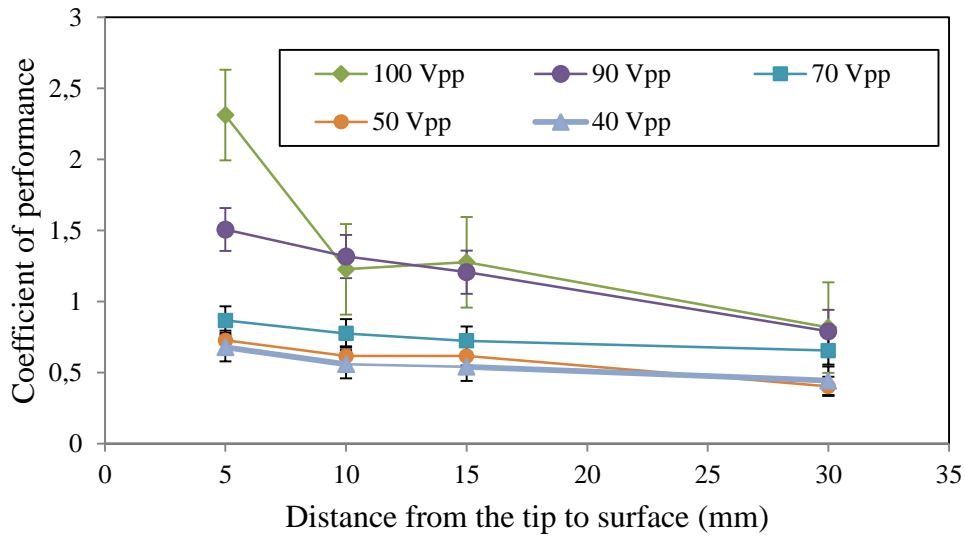
Figure 28: COP for mylar piezoelectric fan

Figure 28 exhibits the performance coefficient of the various operational voltages for the mylar fan. As expected and described in the previous paragraphs, the mylar fan cannot produce flows that can reach the distance of 15 mm with the ability of the heat sweeping. It is like that there is no fan at that distance, so it is highly recommended to make some tip modification to improve the heat transfer abilities.

CHAPTER III

3. FLOW VISUALIZATION

3.1 Flow visualization steps

3.1.1 First attempt for revealing the flow nature

Computer vision is a major that is significantly concerned about the ability of capturing various physical phenomena. Increasing the number and development of tools for this proposes lead to acquisition of more precise data from the experiments. At the beginning of the heat transfer study at the meso scale of cooling devices, the need for visual based data was obvious. The first attempt of approaching the problem was to record a video by the use of a high speed camera. The Phantom camera with the highest capturing rate of approximately 500000 frames per second was available at the lab. The maximum frames per second that used for capturing the sequence of operation for the devices were 2000 frame per second. The highest frame rate could not be used due to the technical difficulties of the image capturing. The highest capturing rates were not used, since the required light source for illumination should be more than the available lightening equipment in the lab.

The first idea for visualization was to copy the flow by help of smoke visualization method with the help of the high speed camera. The needed smoke was made by a smoke pen. The smoke pen produced the fairly dense smoke, while the specific cooling device was operating. The aim was to follow the flow regime under the influence of the cooling device, to understand the formation of the vortices and so on.

The next step was to find a tracking algorithm capable of finding the moving smoke in the captured video. This part of data acquisition was quite time consuming since the captured images did not have enough density of smoke. A motion tracking algorithm was implemented on the videos to check the possibility of using applying approach to extract the required data.

3.1.2 The first algorithm: The optical flow function (Lukas-Kanade approach)

In computer vision, the Lucas–Kanade technique is commonly used as a differential based way of optical flow estimation. This was developed by Bruce D. Lucas and Takeo Kanade [25]. The major considered assumption in the method is the constant flow in a local neighborhood with the radius of a pixel. Thus this assumption was used to solve the basic optical flow equations for every pixel in the specified neighborhood by the least square method. There was an ambiguity in the solution of the optical flow; this could be solved by the interpolation of the data of the nearby pixels. This local method was less sensitive to the noise in comparison with other methods but due to locality it cannot provide any analysis on the interior of uniform regions of the image.

The LK method assumes that gradient of the image variables within the two sequences (frames) of a set is significantly small that can be approximately considered constant within a neighborhood of the suspected point (this point is designated with P). Namely, the local image flow (velocity) vector (V_x, V_y) must satisfy the following conditions:

$$I_x(q_1)V_x + I_y(q_1)V_y = -I_t(q_1)$$

$$I_x(q_2)V_x + I_y(q_2)V_y = -I_t(q_2)$$

$$I_x(q_n)V_x + I_y(q_n)V_y = -I_t(q_n) \tag{6}$$

Where q_1, q_2, q_n are the pixels inside the window, and I_x, I_t, I_y are the partial derivatives of the image I with respect to coordinate designators of x, y and time t, evaluated at the point q_n and at the current time. These equations were the basic of the used algorithms in the visualization of a flow, though the technical problems in this field made it rather time consuming to pursue [25].

3.1.3 Flow visualization results based on LK motion tracking method

The sequencing of the tracking that was performed in the program will be followed step by step to show the output of the code.

The right square of all the upcoming pictures are the captured video of the synthetic jet and the other windows are the various types of possible tracings.
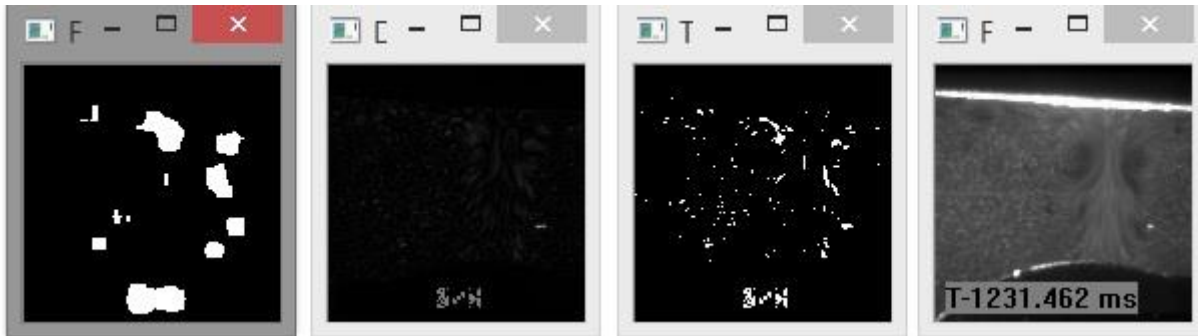
Figure 29: Sequence 1 from the real time flow visualization

In the Figure 29, 4 windows are shown. The right window is the sequence of the captured video with no processing. The other 3 windows are results of applied image processing algorithm. From left to right 4 different forms of motion tracking was used to see the possibility of applied if this method for revealing the movement of the particles and thus the resulting vortices.

Figure 30: Sequence 2 from the real time flow visualization

Figure 31: Sequence 3 from the real time flow visualization

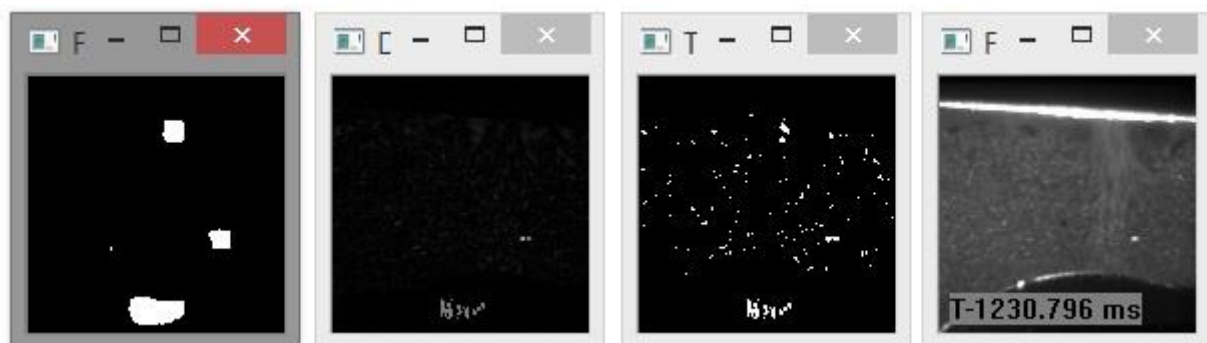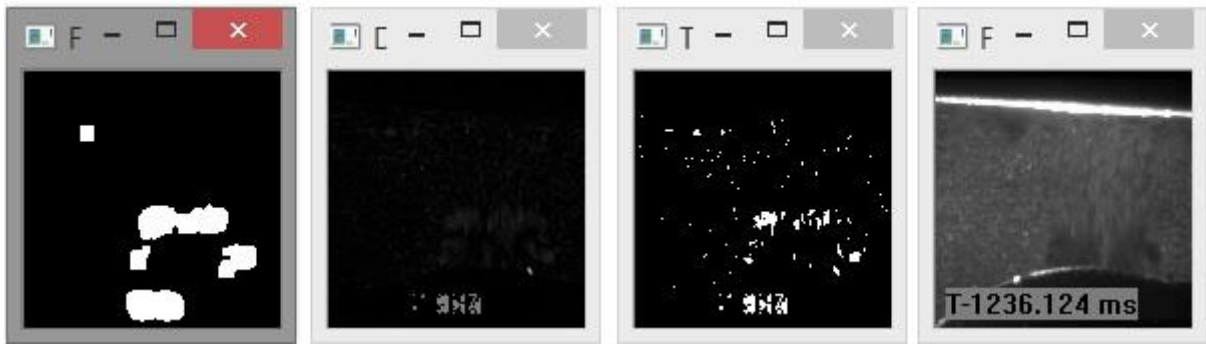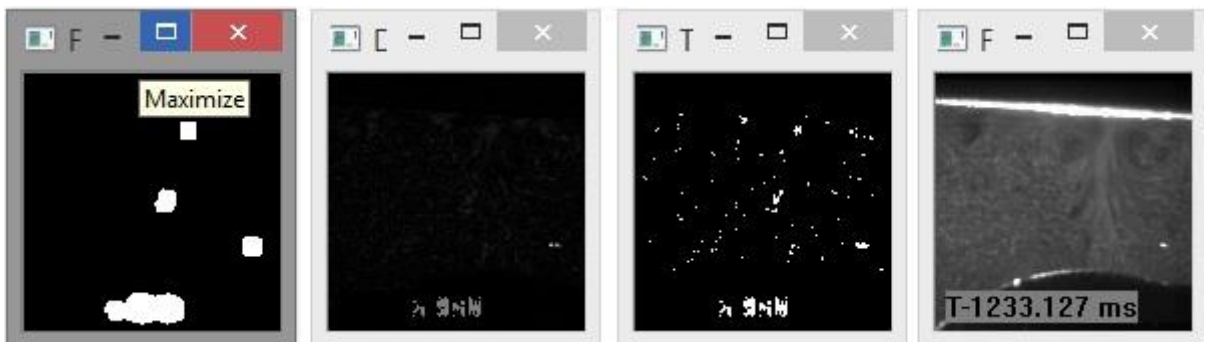Figure 32: Sequence 4 from the real time flow visualization
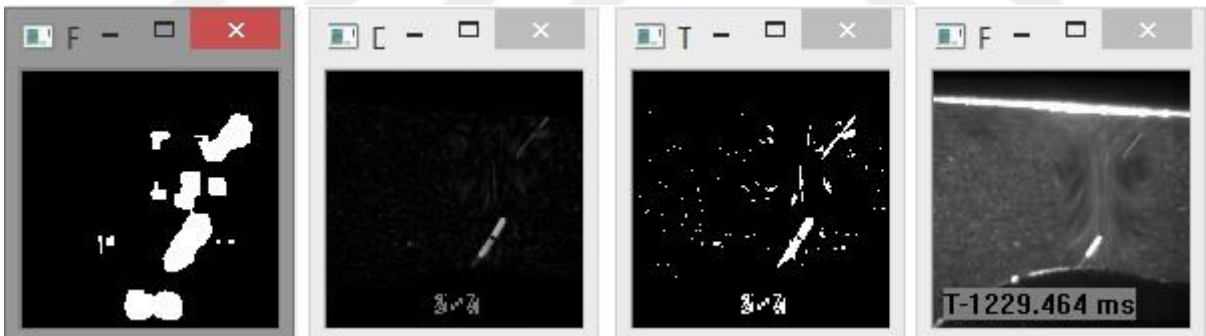
Figure 33: Sequence 5 from the real time flow visualization

Figure 34: Sequence 6 from the real time flow visualization

Figures 29 to 34 show the sequential change in 4 different windows. Movement is shown in these cases and by differentiating these image, many parameters could be gained through openCV. Getting this code working was time-consuming. The code has been written using C language and it has open source image processing library [25].

As seen in the Figures, motion could not be completely tracked and only the particles are partially detected, so this method proves to be insufficient for this specific application.

3.1.4 Analysis methods

The gained data can be analyzed as dots or field of dots. The main target of this phase was to achieve a working code which was done and afterwards the modification was possible without limit. This approach was not enough for the purpose of this study. Since the visualization was not clear and broad enough. Thus a second approach was made to see if the results can be modified and show a better resolution of the flow regime.

3.2 Open source PIVlab software

After the search among the flow visualization methods, an open source software named as PIVlab was found to analyze the specific motion of the fluids. For this matter the sequence of images was still needed. Thus the high speed camera captures were put into analysis by this software to check if the results would be reasonable to use.

The first set of visual result is shown in Figure 35. As it is evident there is no visible pattern available at the picture. Thus it seems second approach would not give a very pristine set of flow visualization results. This means that the quality of input is not compatible with the software abilities. To solve this problem the images should be extracted from the real PIV apparatus. There was an opportunity to perform the PIV test on mylar piezoelectric fan in Washington State University, Vancouver.

In the following parts the results will be shown.
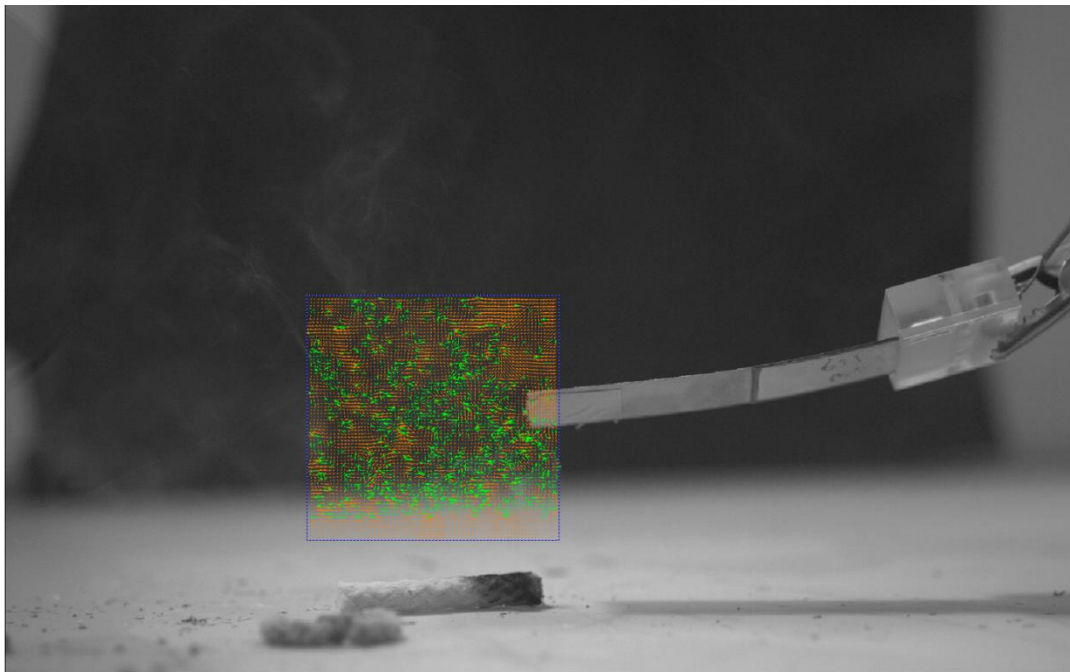
Figure 35 : Analysis of high speed camera images with PIVlab-first trial

3.2.1 Introduction to PIVlab

Digital particle image velocimetry is a qualitative and quantitative flow visualization technique in which there is no intrusiveness introduced. The implemented method in this study is a MATLAB based open source software with a graphic user interface (GUI). The analysis algorithm is quite close to Lukas Kanade (optical flow) that was mentioned earlier. In digital particle velocimetry motion of a fluid is visualized by sheet of fluid with a high density

of reflective and neutrally buoyant particles. The illumination particle should be neutrally buoyant since if not the results of the velocity and vorticity contours might not be accurate enough. Although in practice achieving the density of illumination particle is not a theoretical fact but it is an empirical trial and error practice. Among the 9000 captured images of the PIV only a few could explicitly depict a precise set of contours.
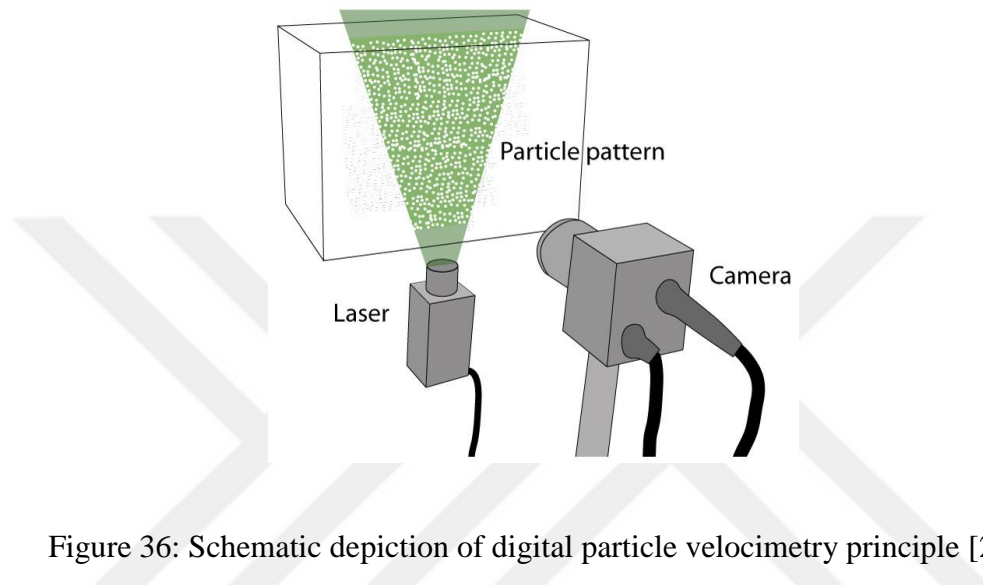
Figure 36: Schematic depiction of digital particle velocimetry principle [26]

Figure 36 shows the concept of the PIV imaging system roughly. A laser plane which is made with a set of optical lenses radiates the particles which are seeded in the fluid. Then a high speed camera captures the sequence of particles movements.

In most DPIV analyses, a pair of images is captured at t_0 and $t_0+\Delta t$. The velocities of the particles in the sheet can be found from the displacement and time increment Δt. It is noteworthy to consider the displacement is calculated for groups of particles by evaluating the cross correlation of many sub images. These sub images are called interrogation areas. The different correlation may result in variations in the velocities achieved. The complete description of the image processing is done in[26].

The precise analysis of the piezoelectric fan was done only for one type of piezoelectric fan with the mylar slab material. The reason was the limits of the time and equipment which were all based in USA and had to be shipped in a small time.

3.2.3 PIV flow visualization for mylar piezoelectric fan

The PIV apparatus used for the mylar piezoelectric fan is depicted in Figure 37, which shows the test chamber, a laser for illumination, a fog generator for seeding, and a camera for visualization.
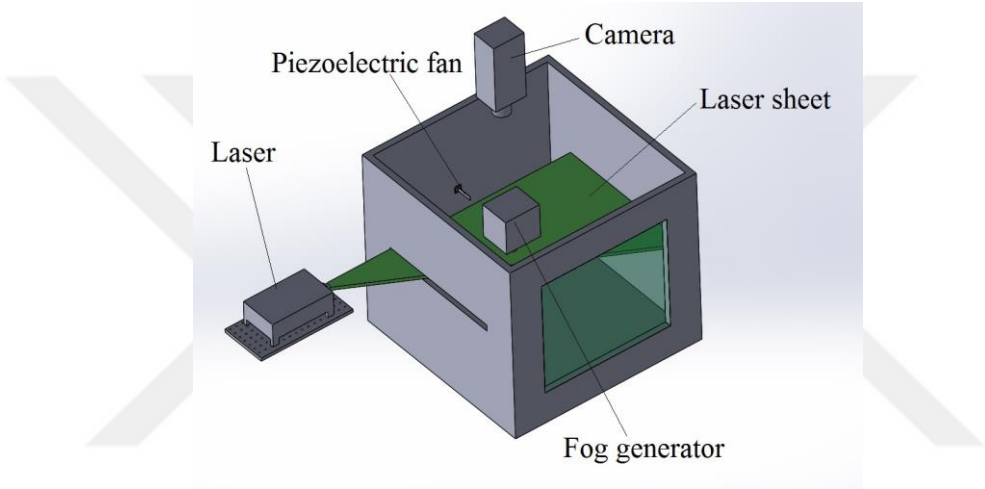
Figure 37 : Isometric view of the PIV setup

The chamber is nearly cubical, with side dimensions of approximately 60 cm. The tank is constructed from rigid aluminum plates, with the top surface open for the placement of the camera. On one side wall, there is a slot to provide access for the PIV laser sheet. This slot is sealed with acrylic plate.

The piezoelectric fan is placed inside the test chamber, with the tip oriented vertically and parallel to the side wall. The piezoelectric fan is fixed tightly inside the enclosure. When studying impinging piezoelectric fan flow, a thin Plexiglas plate is also placed inside the tank as a target. When there is no plate inside the tank, this is referred to as free flow.

In the PIV experiments, two laser pulses are applied in close succession with a dual-head laser. These pulses are converted into light sheets using a pair of lenses, and the sheets enter into the chamber to illuminate the seed particles. A fog generator produces micron-scale oil droplets, which act as tracers. A digital camera is positioned vertically above the tank, which captures images simultaneously with the pulses. During testing, an acrylic plate closes the top of the chamber, isolating it from the rest of the laboratory. An elaborate description of the PIV system is provided elsewhere [27].

The image pairs are processed using the open-source, MATLAB-based software PIVlab 1.35 [26]. This code divides the image pairs into smaller interrogation regions. These are cross-correlated to determine the local displacement of the particle distribution, which is converted to the local velocity. This software tool iteratively decreases the region size to improve the spatial resolution of the vector field. For all cases, the smallest interrogation region was approximately 1 mm by 1 mm.
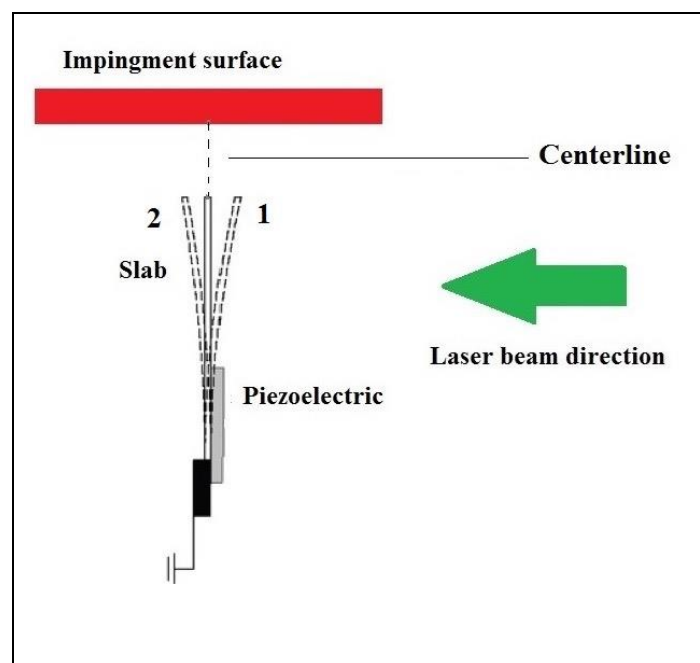

Figure 38 : Schematic depiction of fan positions. Position 1 shows the maximum deflection position to the right side, while position 2 shows the maximum to the left.

Around 7000 sequences were captured for the case of mylar piezoelectric fan. The sequences were dived into the groups of 100 or 150. The first 2000 set of the images are rather not good enough or mainly used for the sake of calibrating the images. The contours of the velocity are captured for the 2100 to 7000 images.
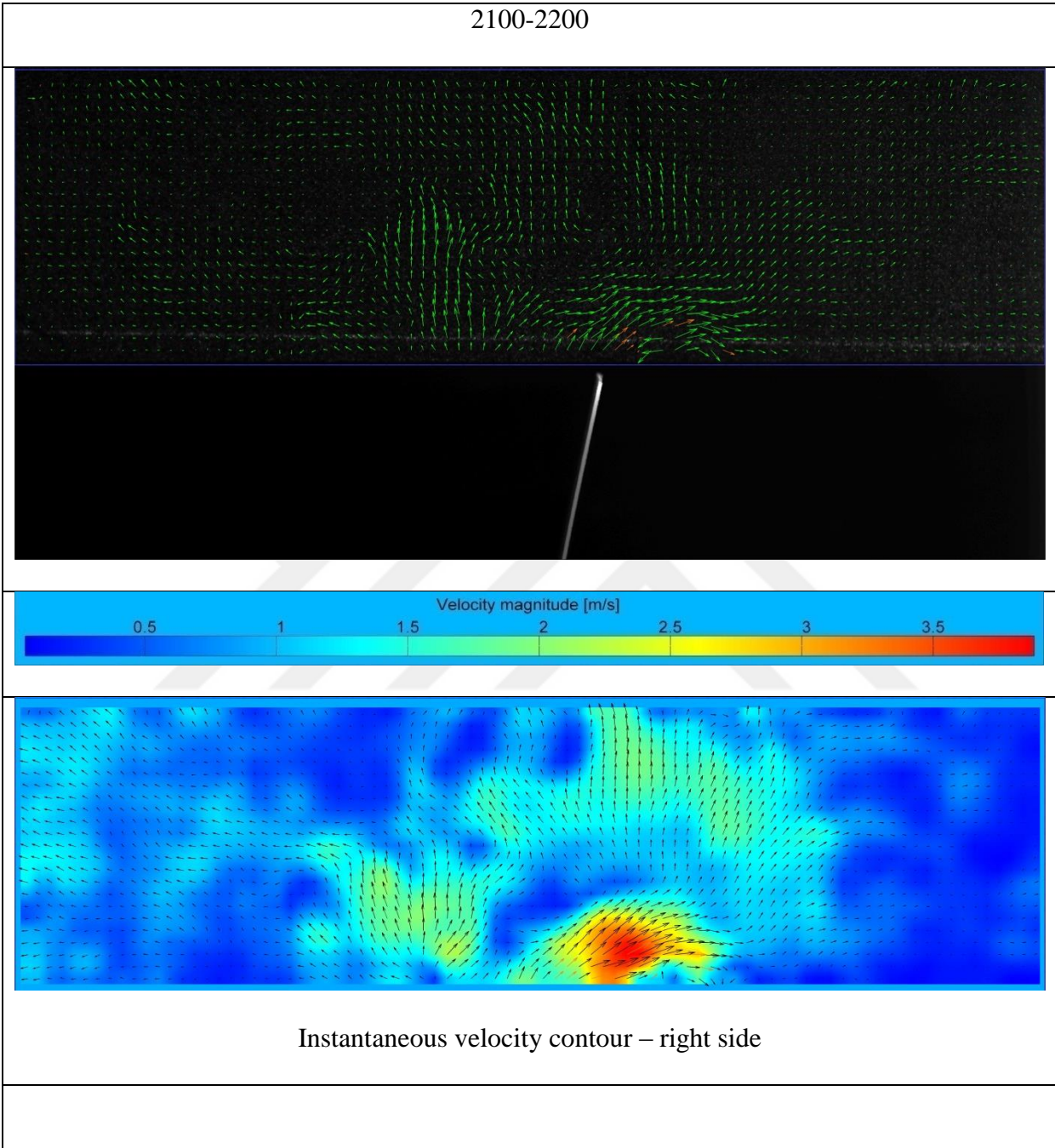
Table 6 : Sequencing number sets and the operational condition

Sequence set	Piezoelectric fan operating condition
2100-2200	Free operational mode
2300-2350	Free operational mode
2350-2450	Free operational mode
2550-2650	Free operational mode
2650-2750	Free operational mode
4000-4100	Impinged piezoelectric operational mode
4100-4200	Impinged piezoelectric operational mode
4600-4700	Impinged piezoelectric operational mode
4700-4800	Impinged piezoelectric operational mode
6000-6100	Impinged piezoelectric operational mode
6100-6200	Impinged piezoelectric operational mode
6200-6300	Impinged piezoelectric operational mode
6600-6700	Impinged piezoelectric operational mode
6700-6800	Impinged piezoelectric operational mode
6800-6900	Impinged piezoelectric operational mode
6900-7000	Impinged piezoelectric operational mode

Table 6 shows the sequence ranges and the operational conditions of the piezoelectric fan.

 The free operation mode is the condition that piezoelectric fan is operating without no constrains (plate) in front of it. The Impinged piezoelectric operational mode contains a plate

which limits the distance that the fluid can travel away from the tip. The second mode was tested to see the mechanism of the flow in the close distances.

2100-2200
Instantaneous velocity contour – right side

Instantaneous velocity contour- fan at the right side

Instantaneous velocity contour-fan starts to move towards left side

Instantaneous velocity contour-fan at the right side
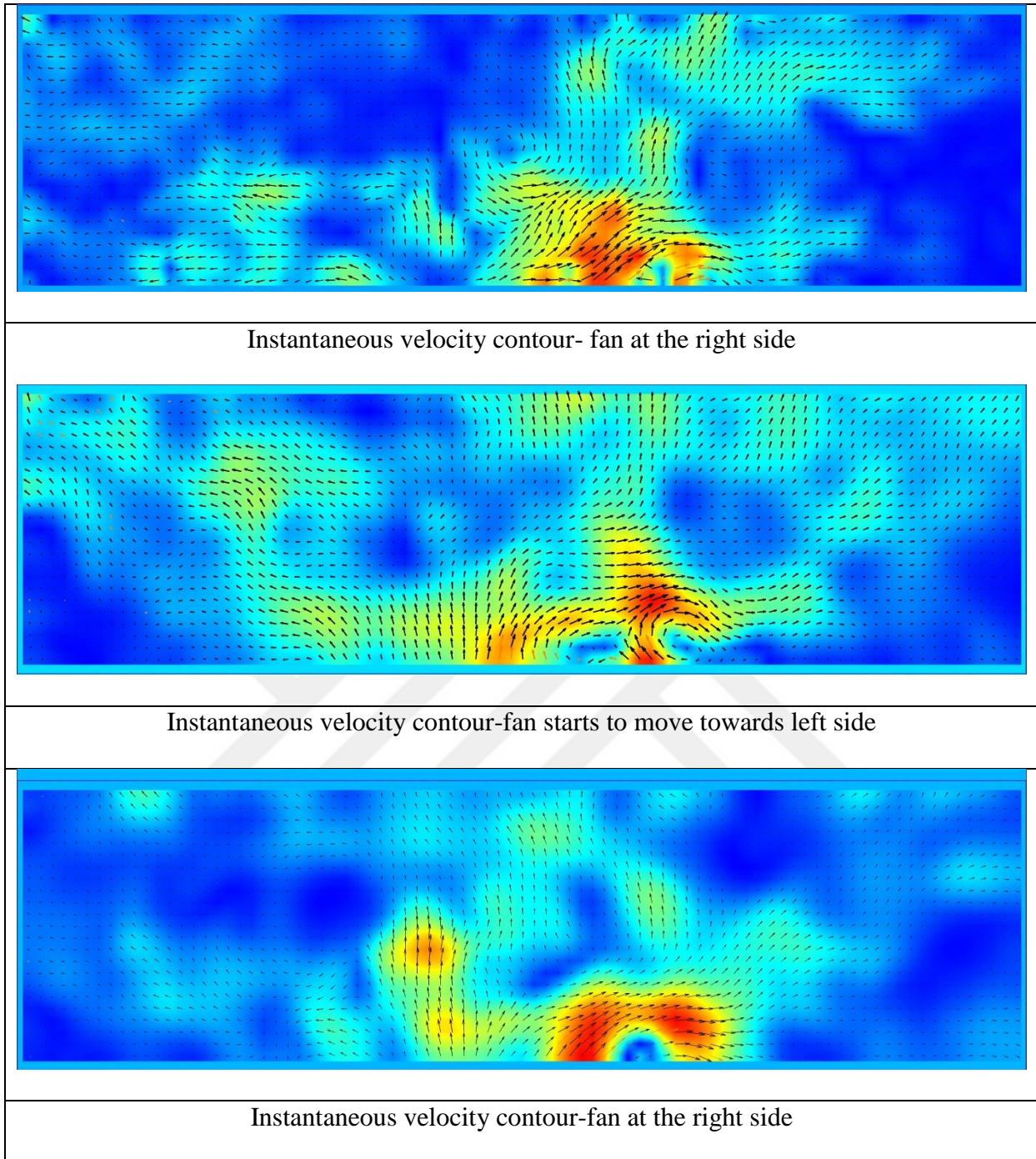
Figure 39: Mylar fan in the mid-right side operational positions

Figure 39 shows the formation steps of a vortex on the right side of the operating mylar fan. The fan is at the stage which is shifting towards the right side. This is the reason that the vortex is about to form in this side. The air is pushed in this direction and the contours of the velocity in the various frames are complying with this movement as well.

2300-2350
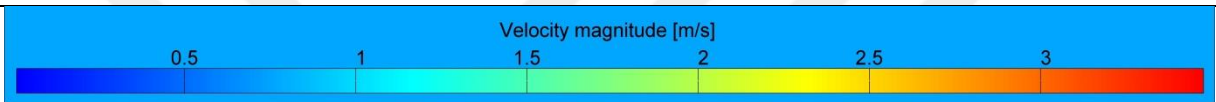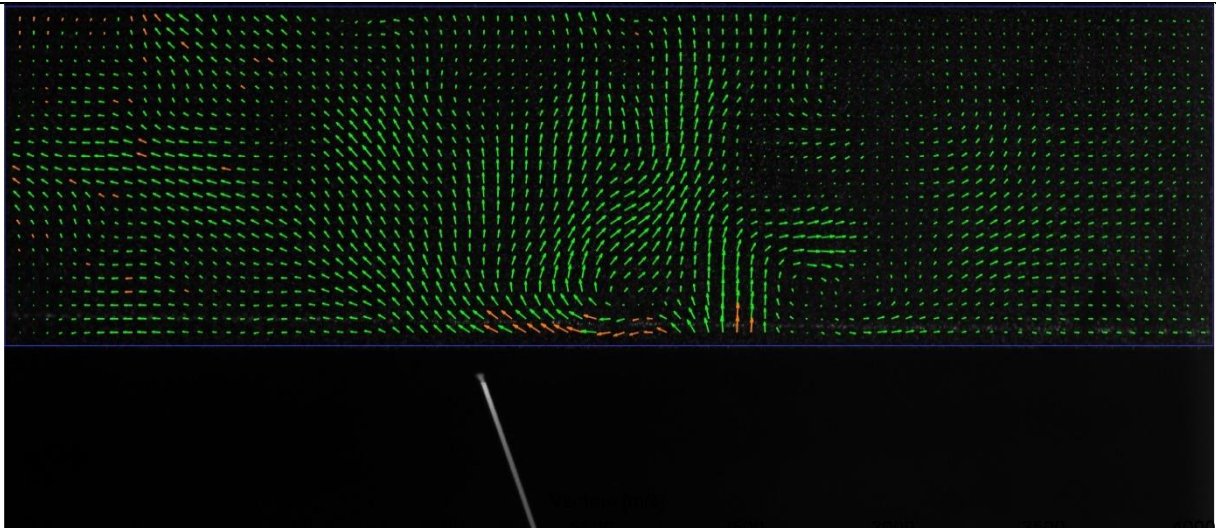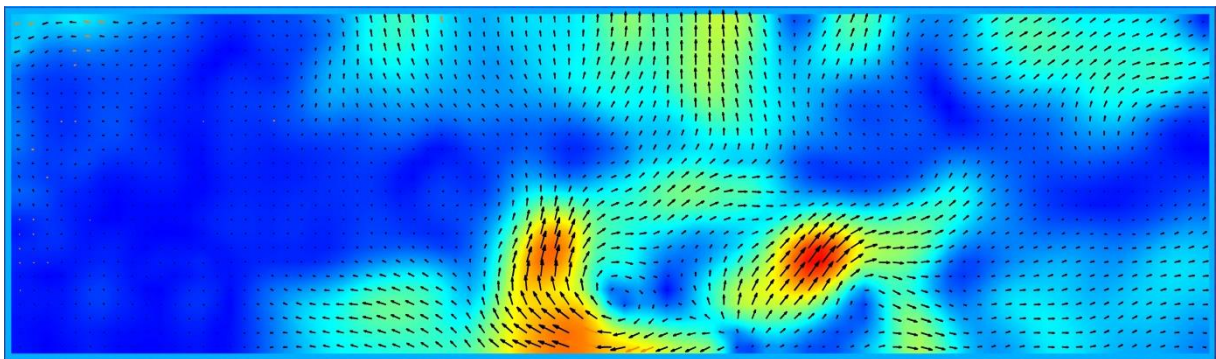
Velocity magnitude [m/s]

Instantaneous velocity contour

Instantaneous velocity contour

69

Instantaneous velocity contour

Instantaneous velocity contour

Average of 20 pairs of images

Instantaneous velocity contour

Instantaneous velocity contour

Instantaneous velocity contour
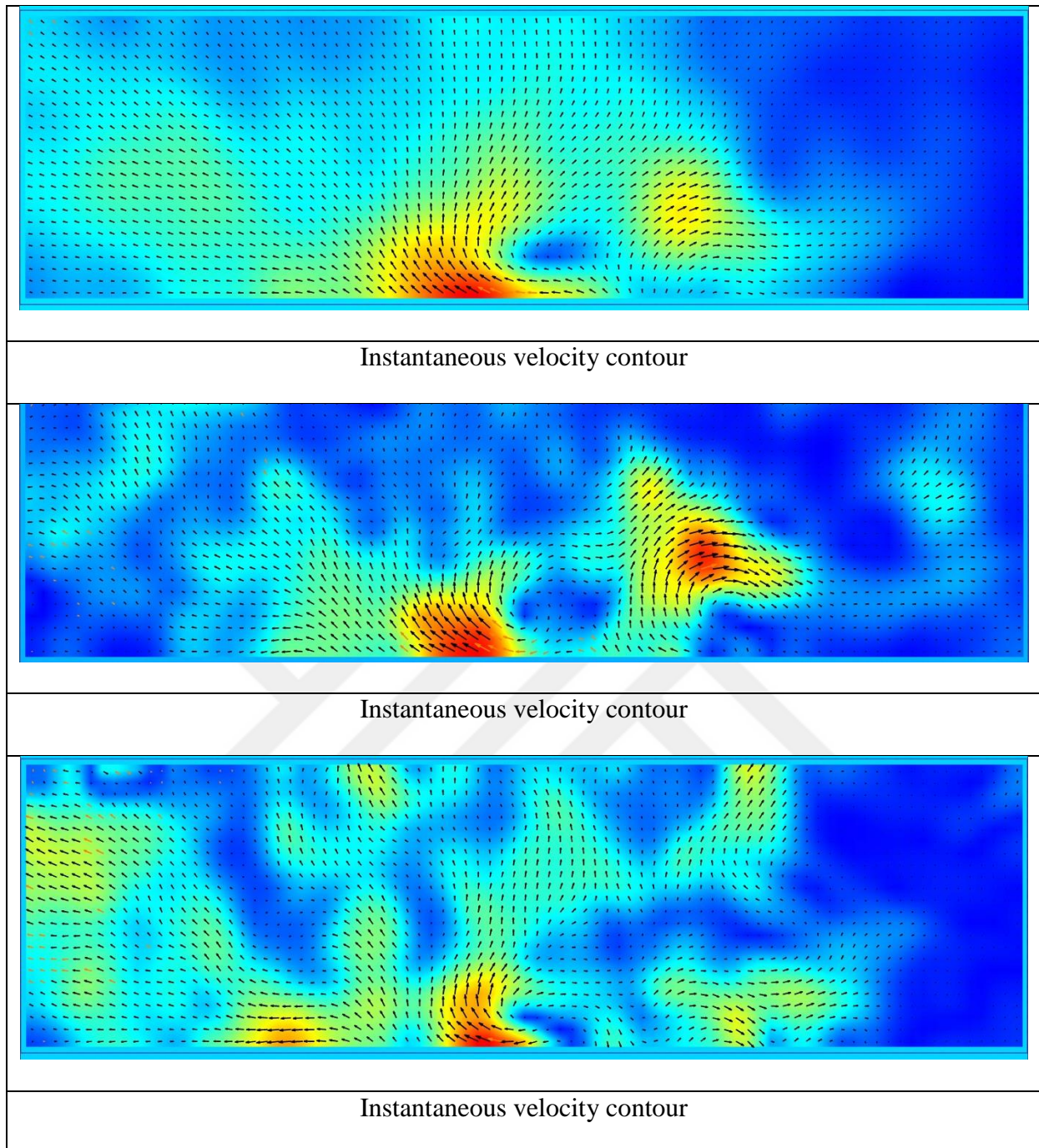
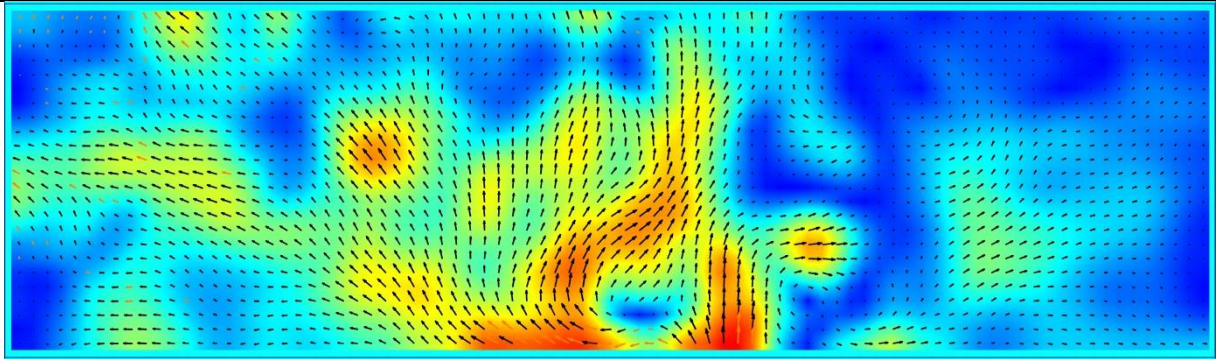Figure 40: Mylar fan in the mid-left side operational positions

In Figure 40, the fan is in the left side, contours of the velocity shows that the previously formed vortex at the right side is now dying, while on the left side the gradient of the velocity is depicting a start of a new formation. It is important to note that this is very time consuming to use all the available sequences, and only some of the sequences are shown to understand the trend of the flow and the formation of the vortex.

2350-2450

Velocity magnitude [m/s]
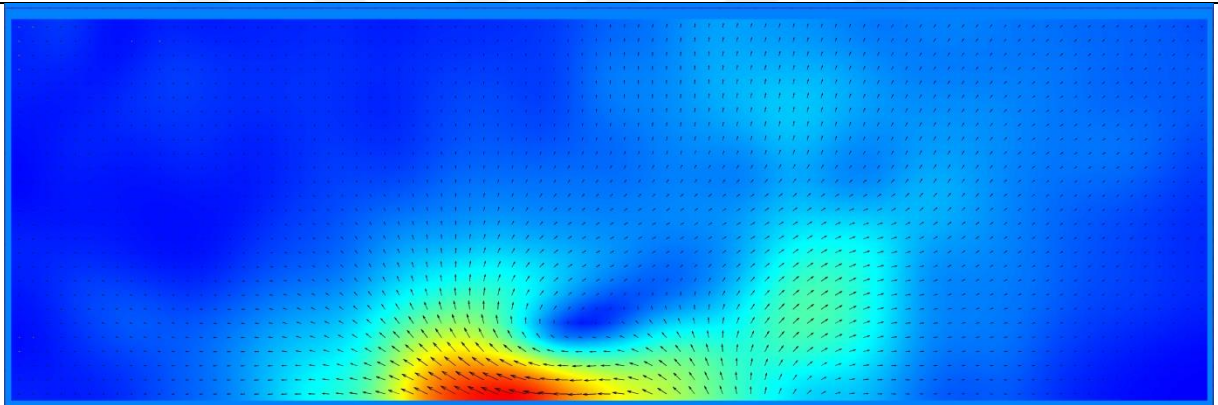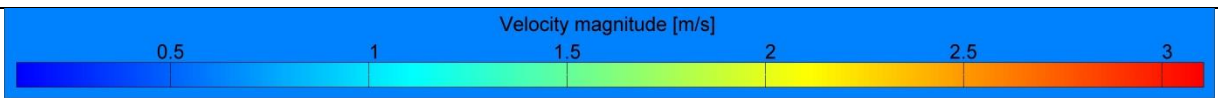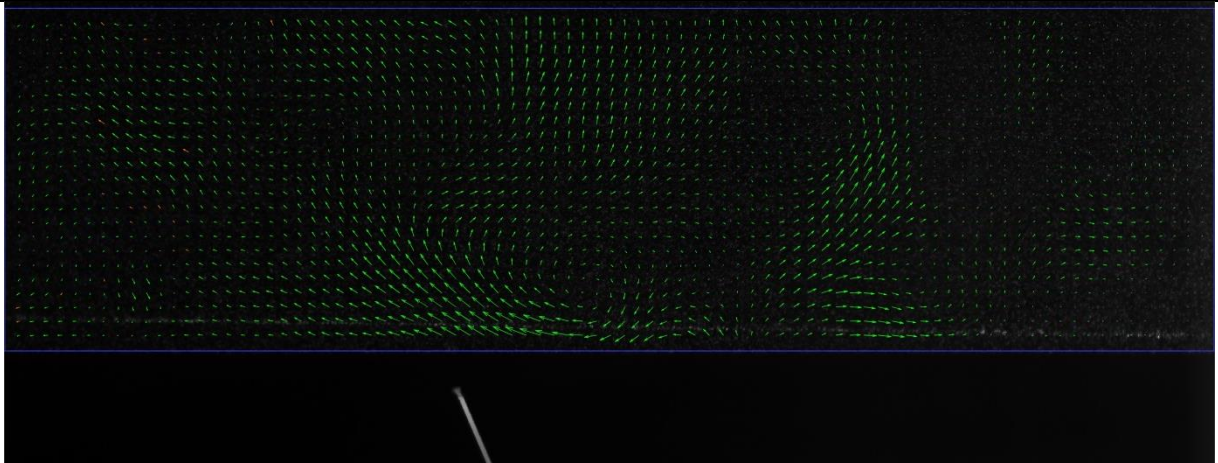
Average over 30 pairs of images
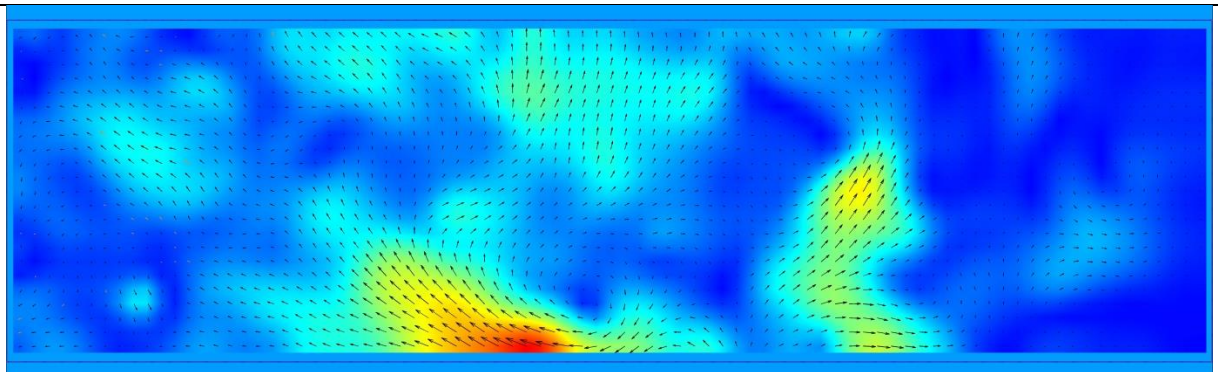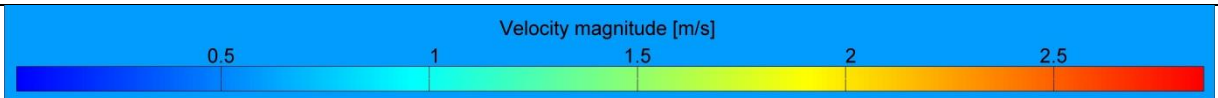
Velocity magnitude [m/s]

Instantaneous velocity contour

Instantaneous velocity contour

Instantaneous velocity contour- fan at the left side

Instantaneous velocity contour

Instantaneous velocity contour

Instantaneous velocity contour

Figure 41: Mylar fan in left side operational positions
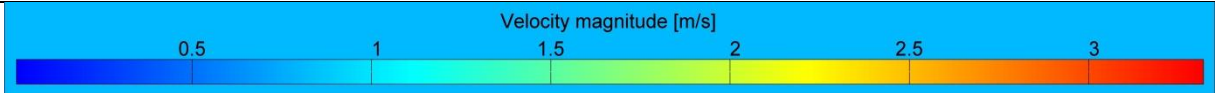
Instantaneous velocity contour
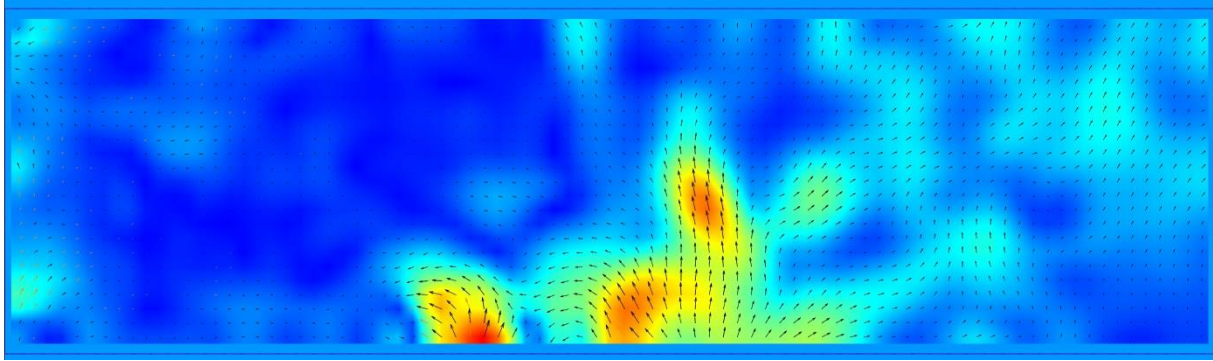
Instantaneous velocity contour

Figure 42: Mylar fan in transition from left side to right side operational positions

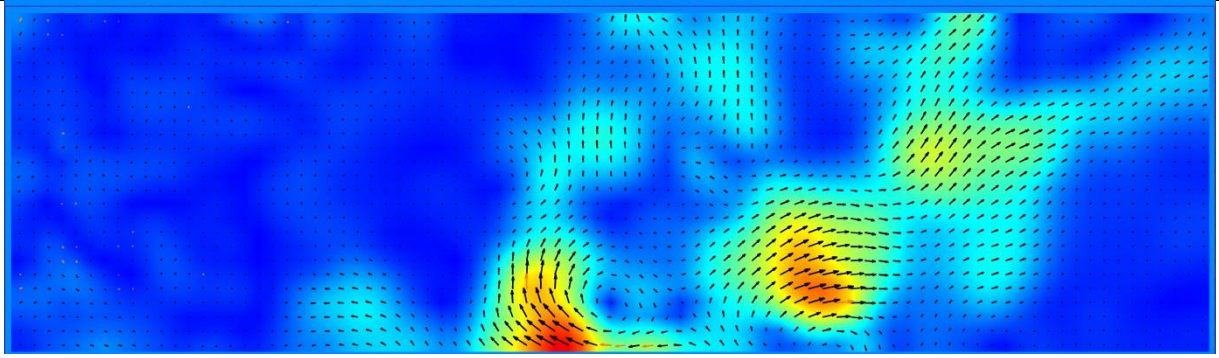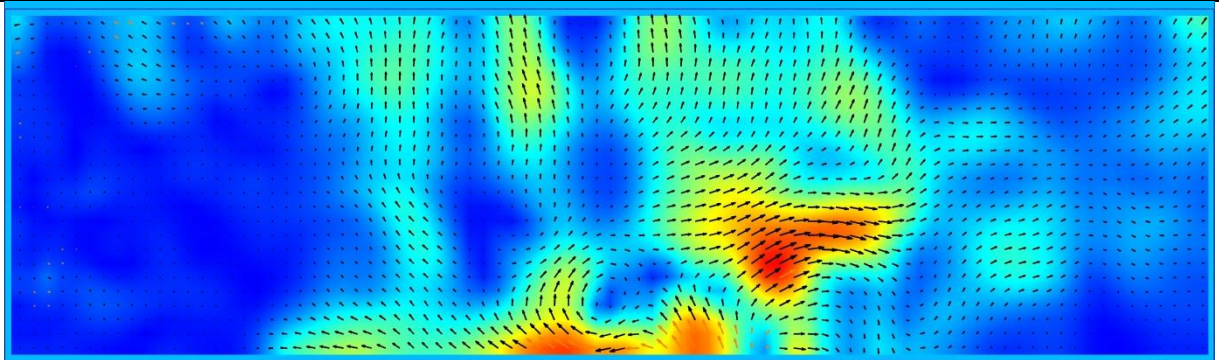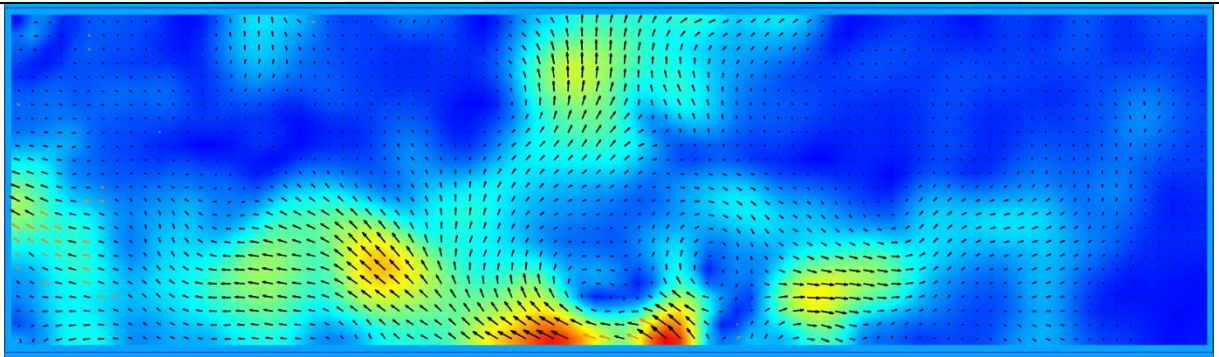| 2650-2750 |
|---|

Instantaneous velocity contour

Instantaneous velocity contour

Instantaneous velocity contour
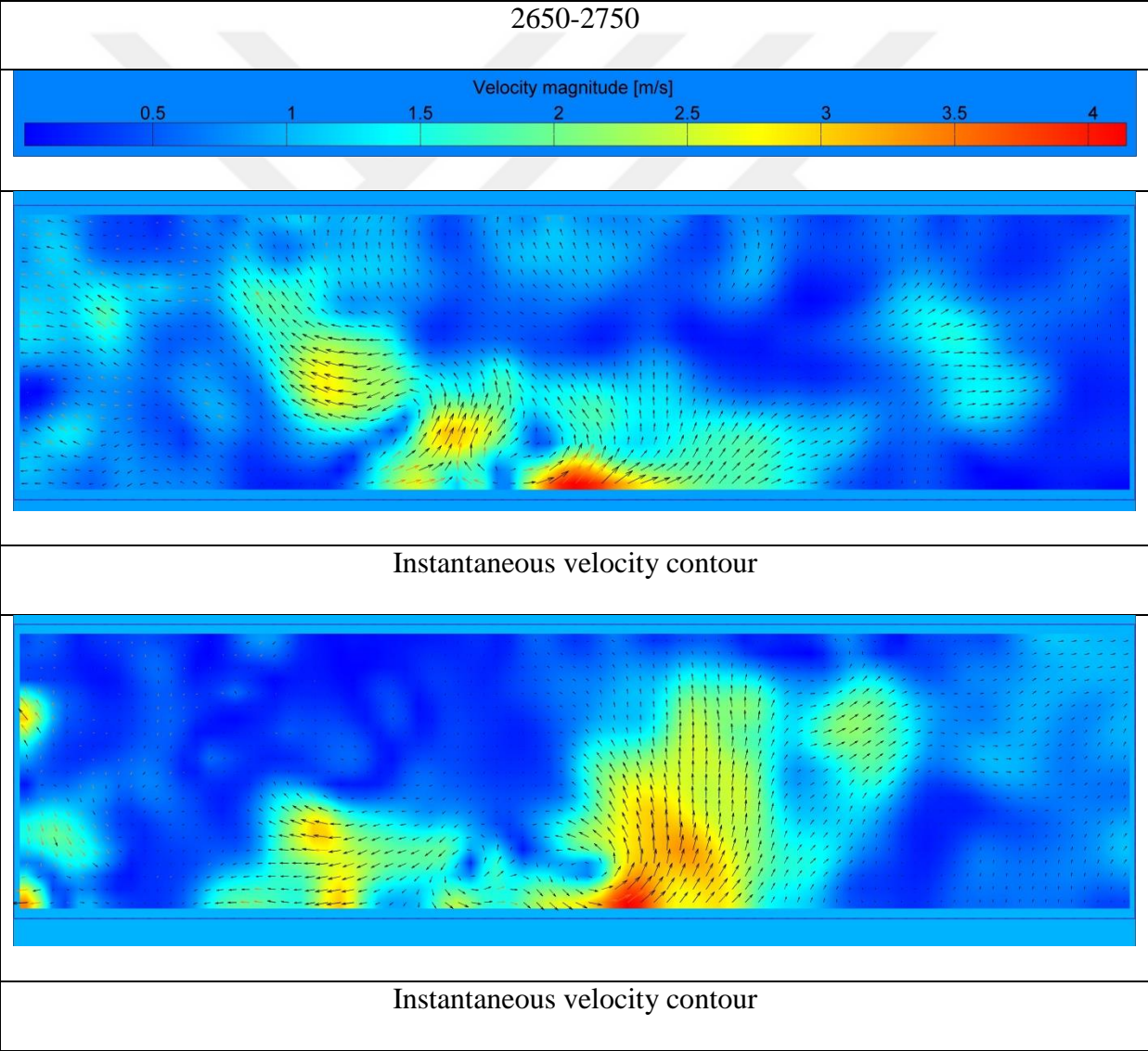
Instantaneous velocity contour

Instantaneous velocity contour
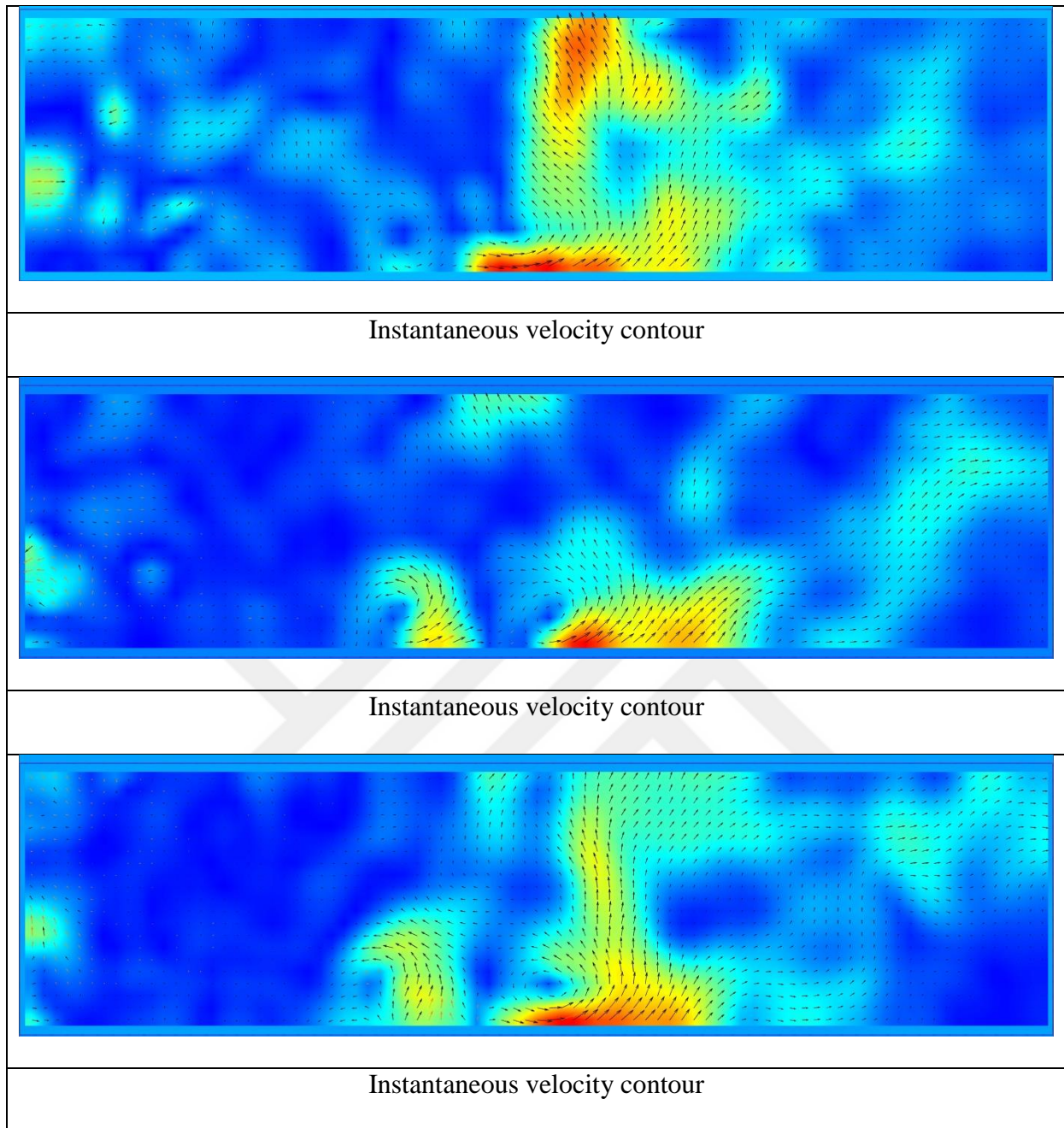
Figure 43**:** Mylar fan in mid-right side operational positions (time dependent sequences)

Figures 40-43 are selected to show the pathways of the flow in the various phases of the mylar fan operation. The high gradients which are the red zones are the flow regions which are affected the most by the cooling device. One can see the far away regions are mainly blue, which can be interpreted as the untouched area by the device.

2750-2850
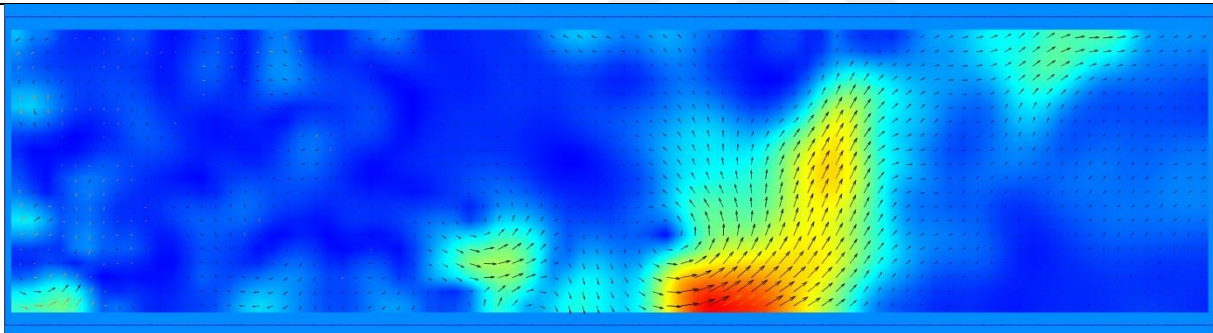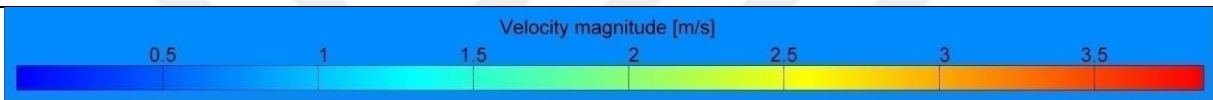
Instantaneous velocity contour
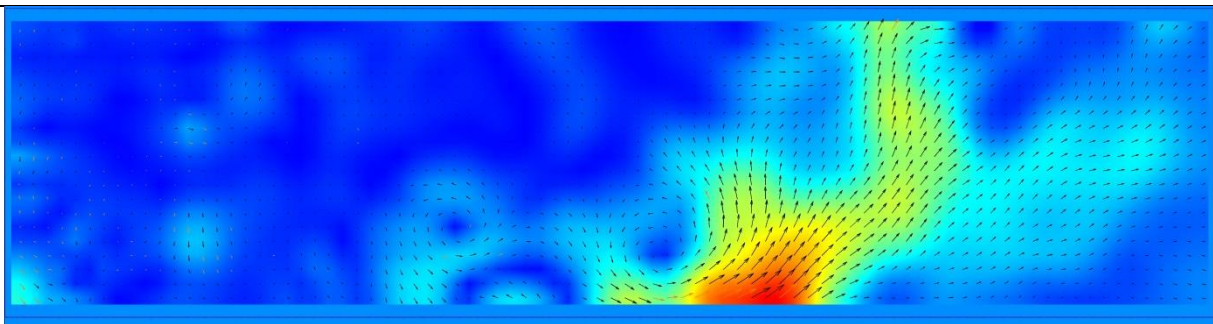
Instantaneous velocity contour

Figure 44**:** Mylar fan in the extreme right side operational positions

Now at its extreme right position, shown in Figure 44, the red zone is seen very clearly. The maximum velocity level is achieved at this phase of the operation by the mylar fan, providing a full vortex on the right side.

4000-4100
Instantaneous velocity contour

Instantaneous velocity contour
Instantaneous velocity contour
Instantaneous velocity contour
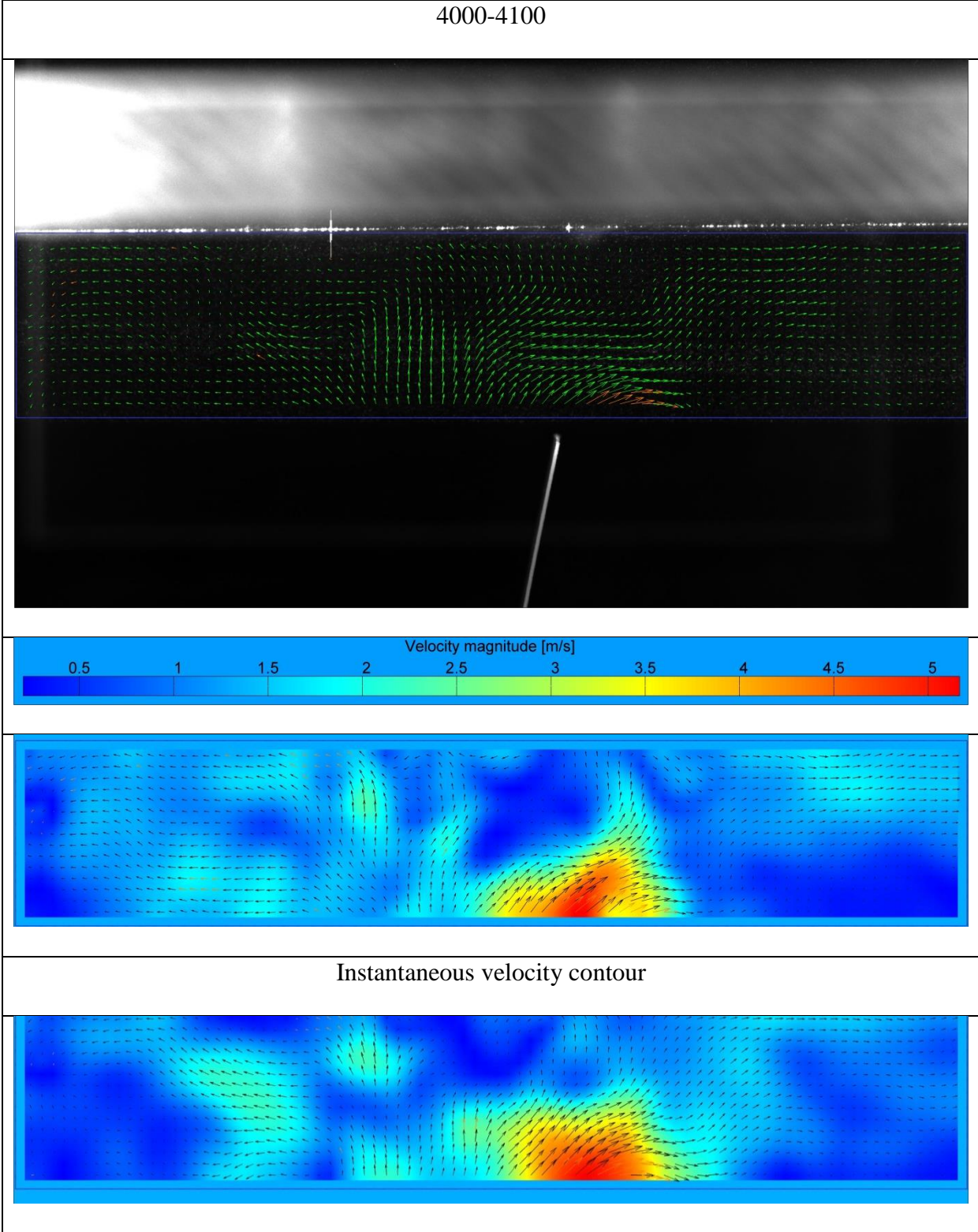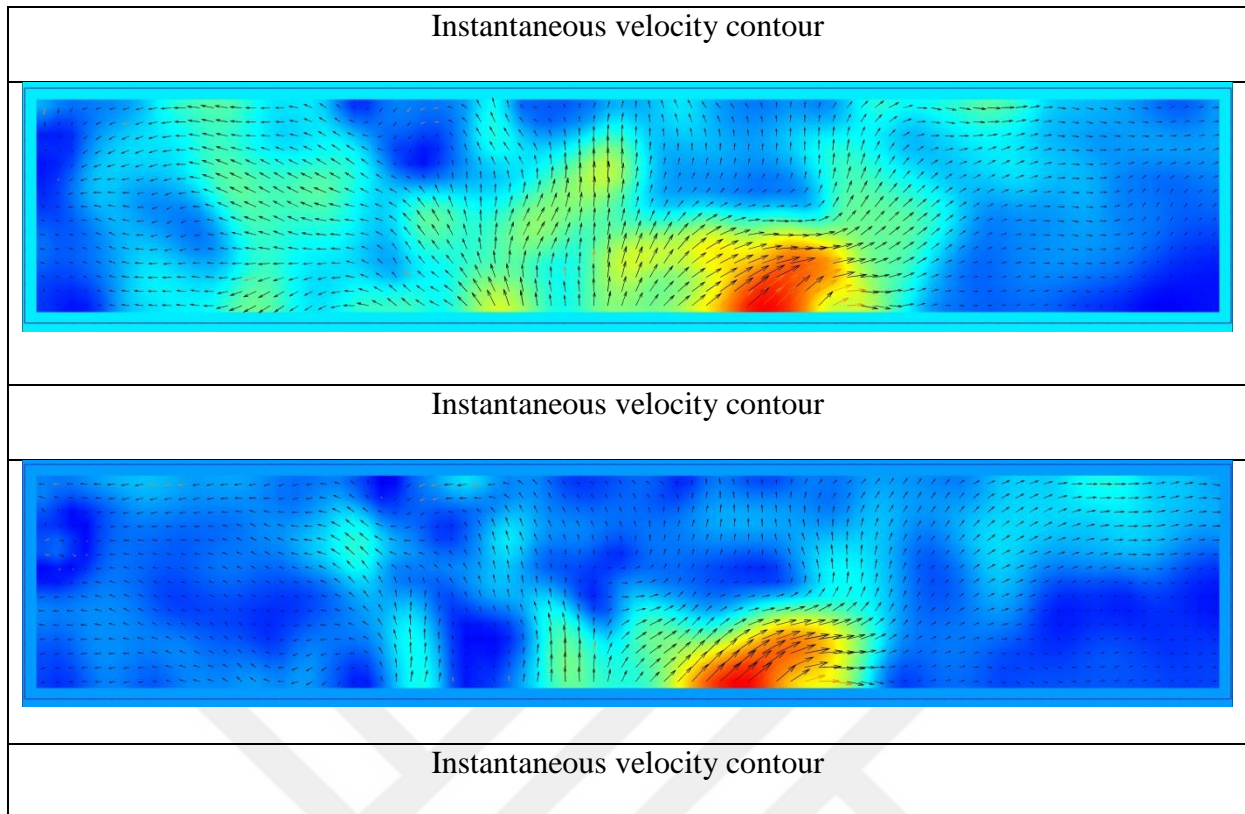
Figure 45**:** Mylar fan near neutral positions (leaning a bit towards right side)

Figure 45, depicts a position of the fan, near to the centerline or the neutral operational mode. The red high gradient zone is now about to fade, since the flow direction is now inclining towards the left side. Now the right side vortex is decomposing.

Instantaneous velocity contour

Instantaneous velocity contour
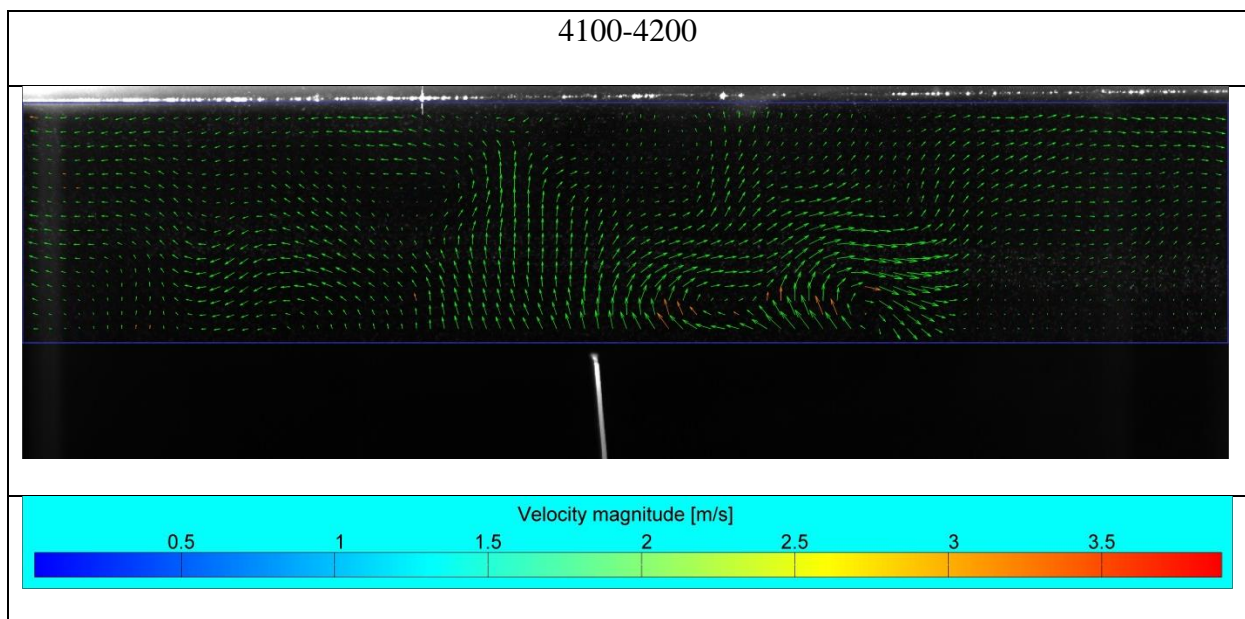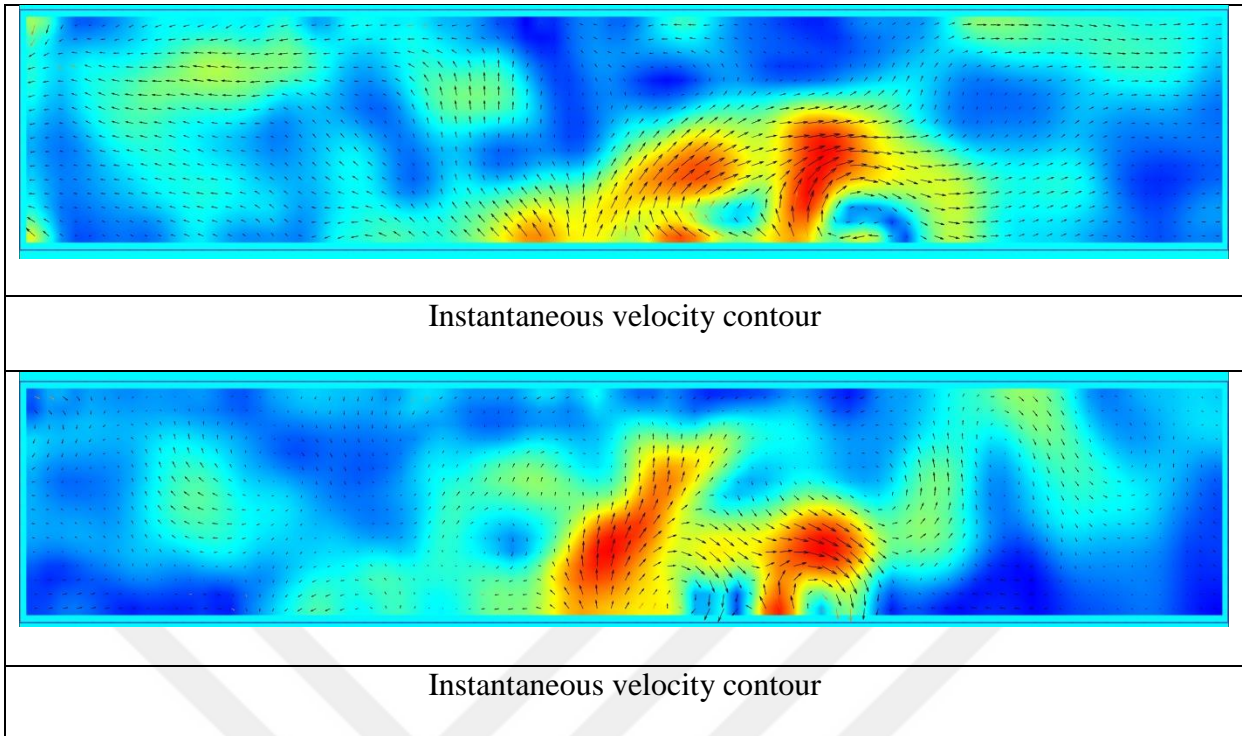
Figure 46: Mylar fan near the neutral operational positions (tip leaning a bit towards left side)

As it is seen in Figure 45, the position of the fan in Figure 46 is now near to the neutral center line, but inclined towards left side at this stage. A red zone with a bigger area is forming on the left side while the previous right side is eventually losing the power.

4600-4700

Instantaneous velocity contour
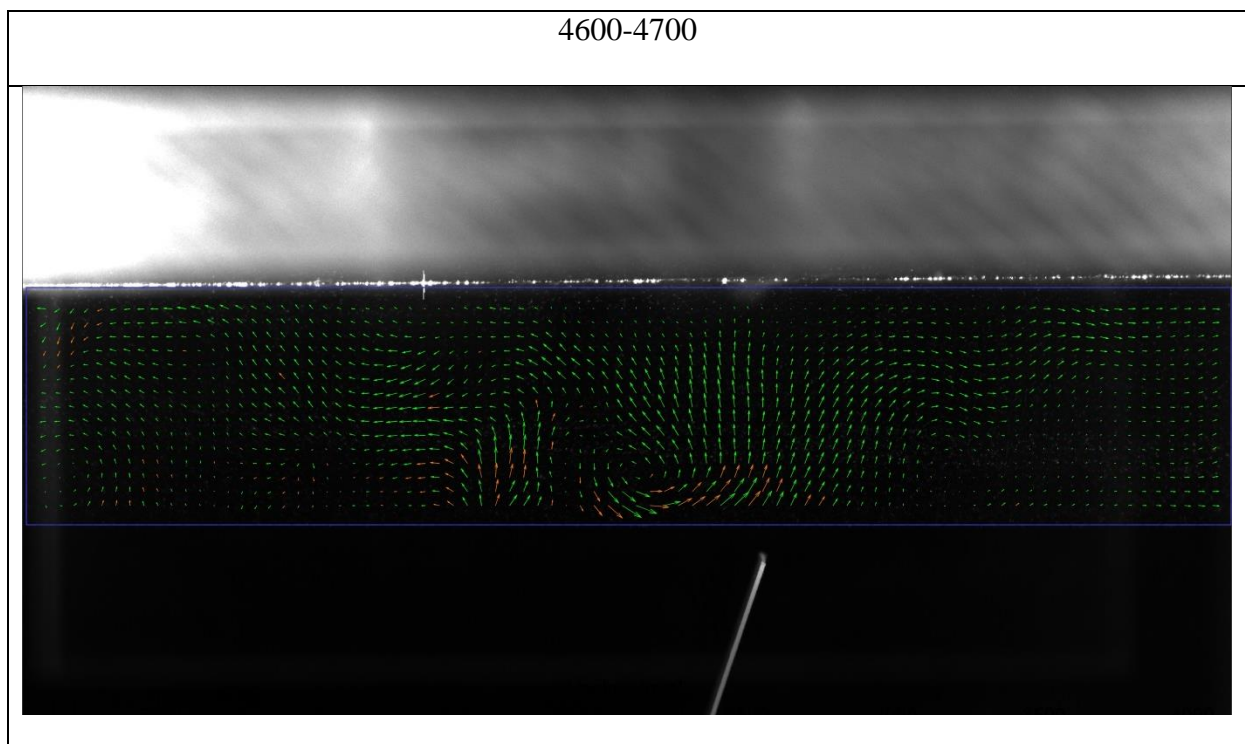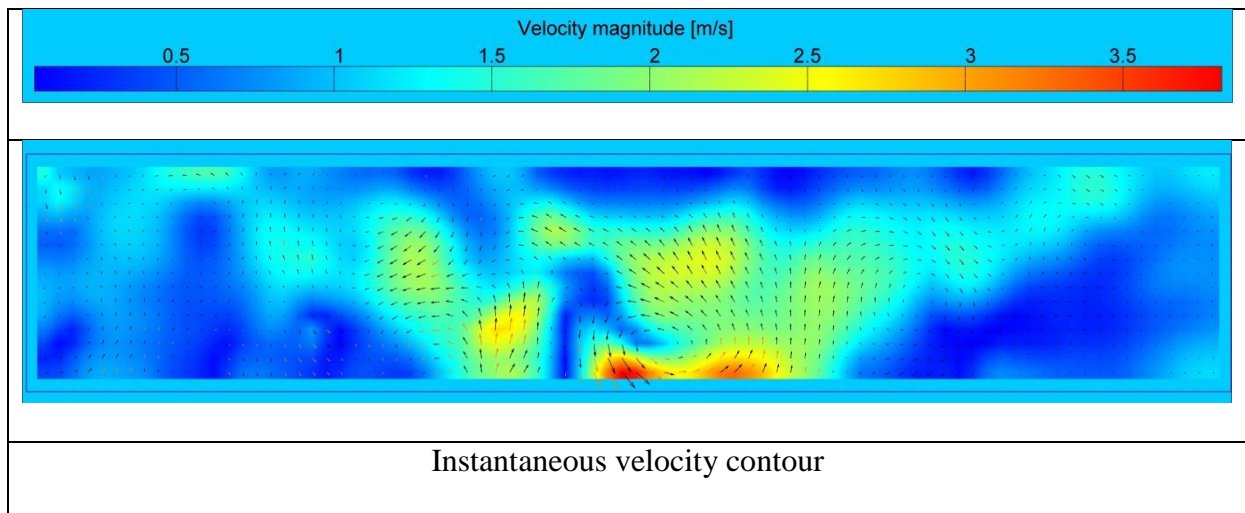
Figure 47: Mylar fan in the right side operational position

4700-4800

Instantaneous velocity contour
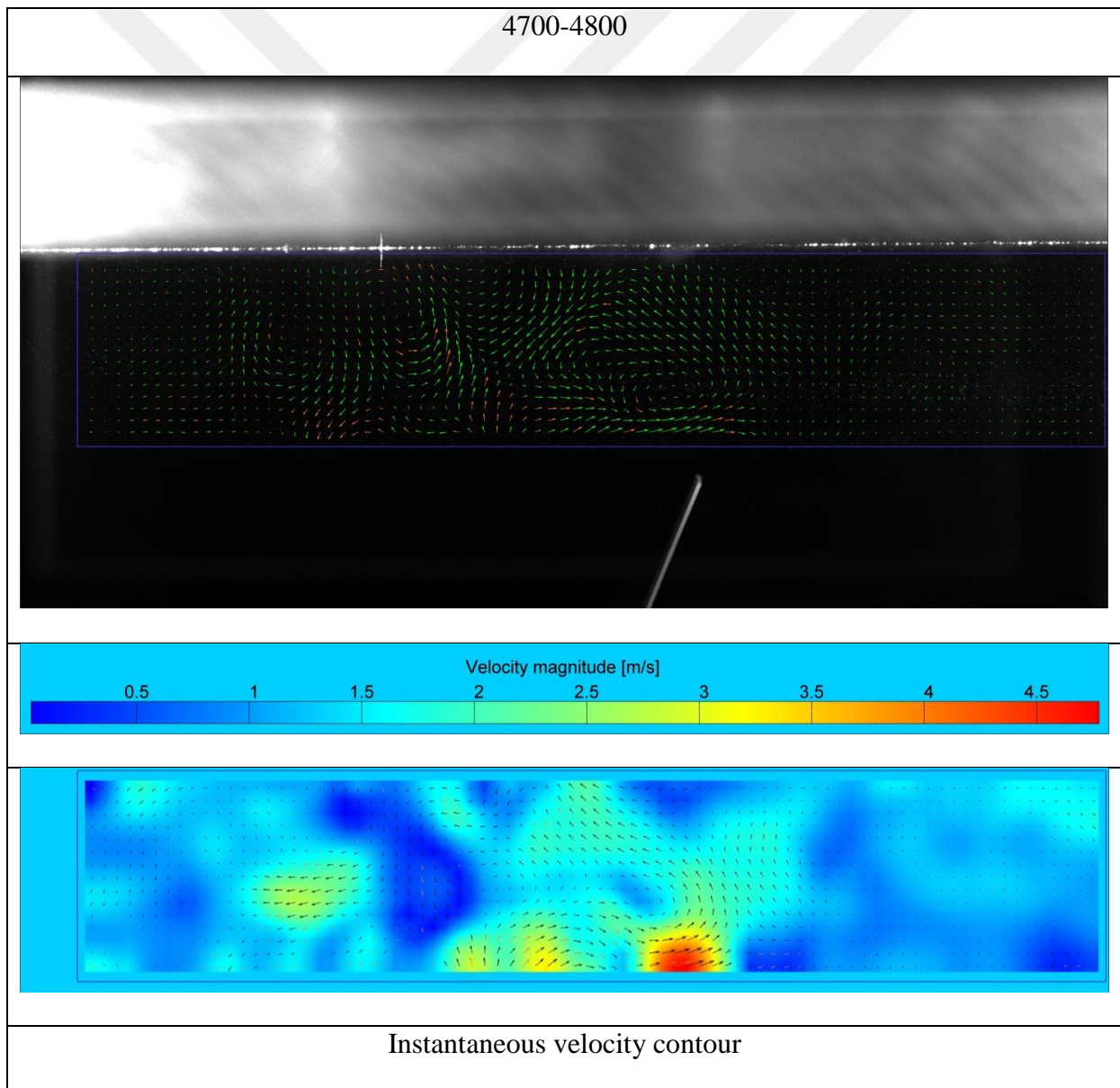
Figure 48: Mylar fan in the right side operational position

Figures 47-48 are quite similar, since they are from the two very close sequences of the frames. The same high power red zone presence is detected in these pictures. And this is logical since the tip is now acting on the right side.

6000-6100
Velocity magnitude [m/s]
Instantaneous velocity contour
Instantaneous velocity contour
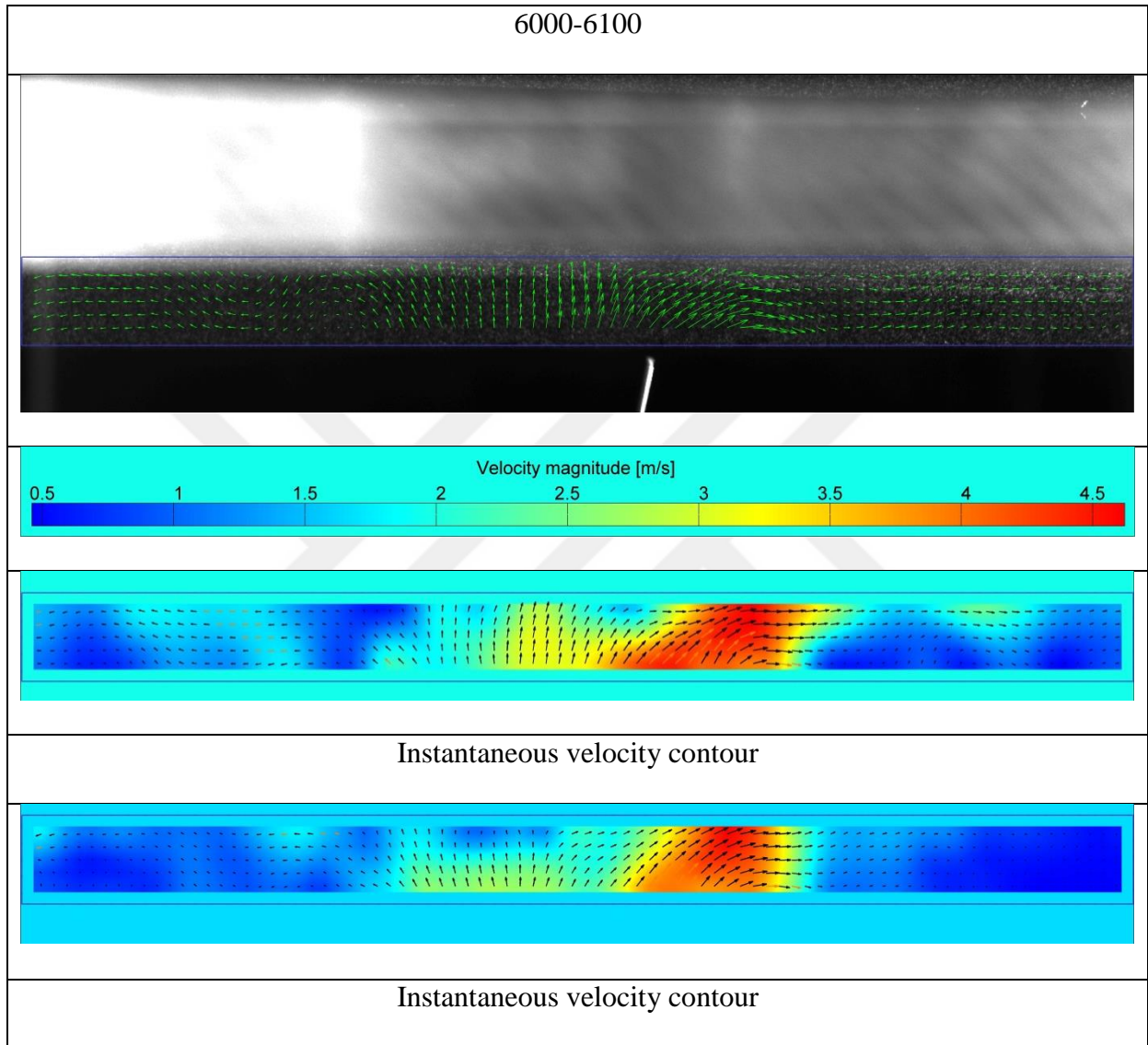
Figure 49**:** Mylar fan in the right side operational positions (Impinged)

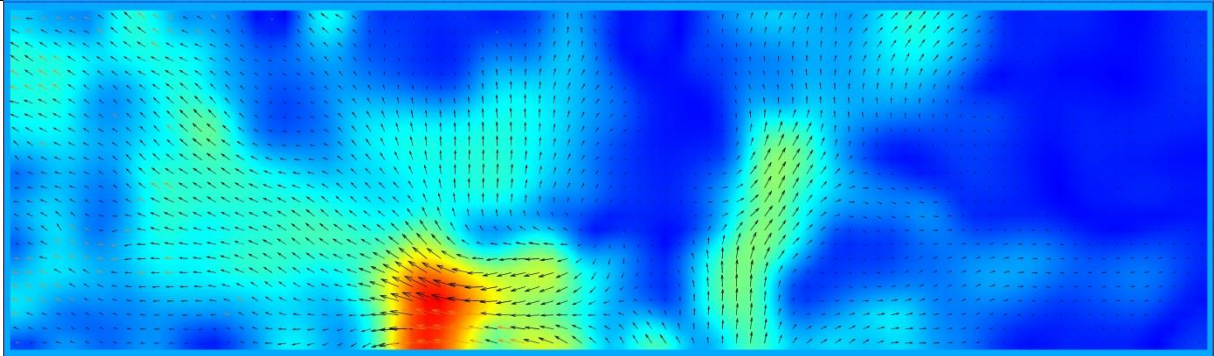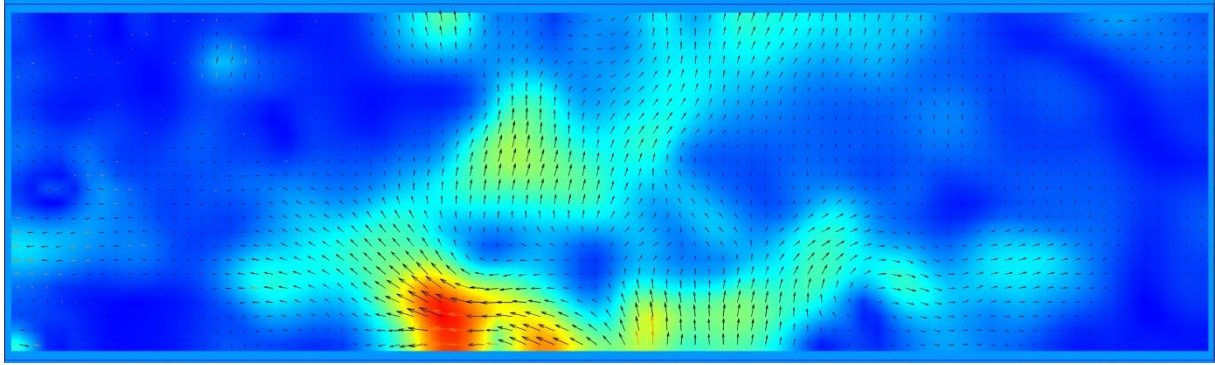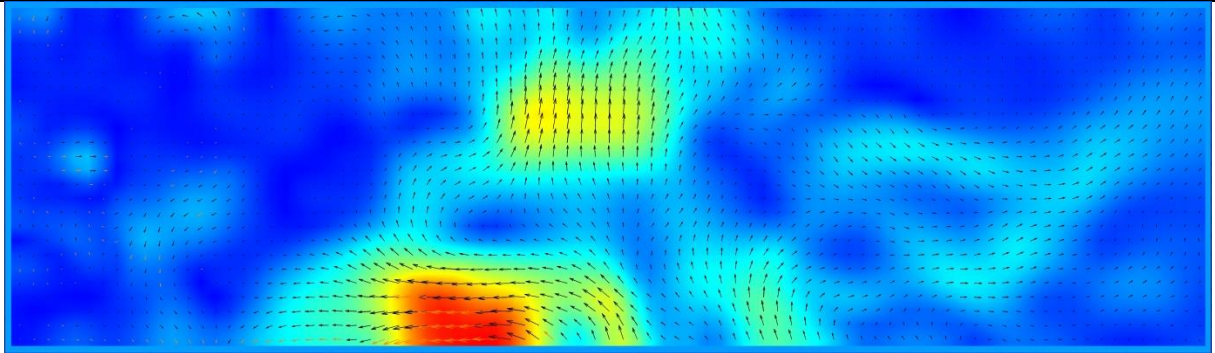| 6100-6200 |
|---|
| |

Instantaneous velocity contour

Instantaneous velocity contour

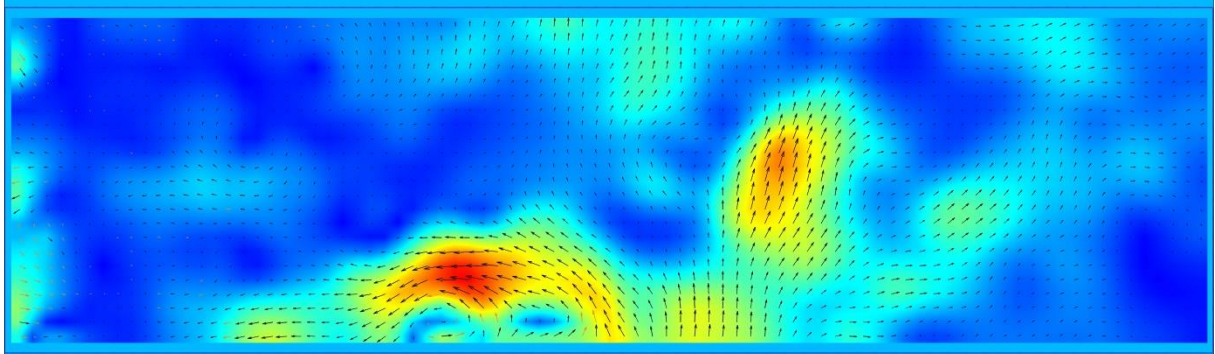Instantaneous velocity contour

Instantaneous velocity contour

Instantaneous velocity contour
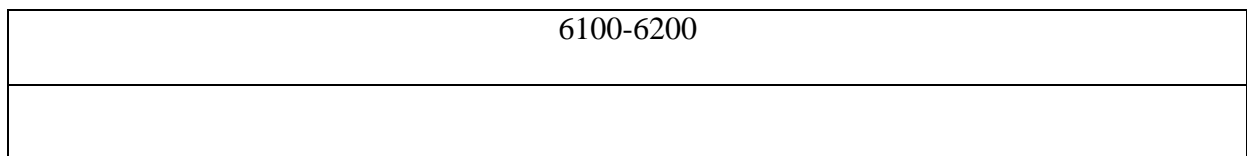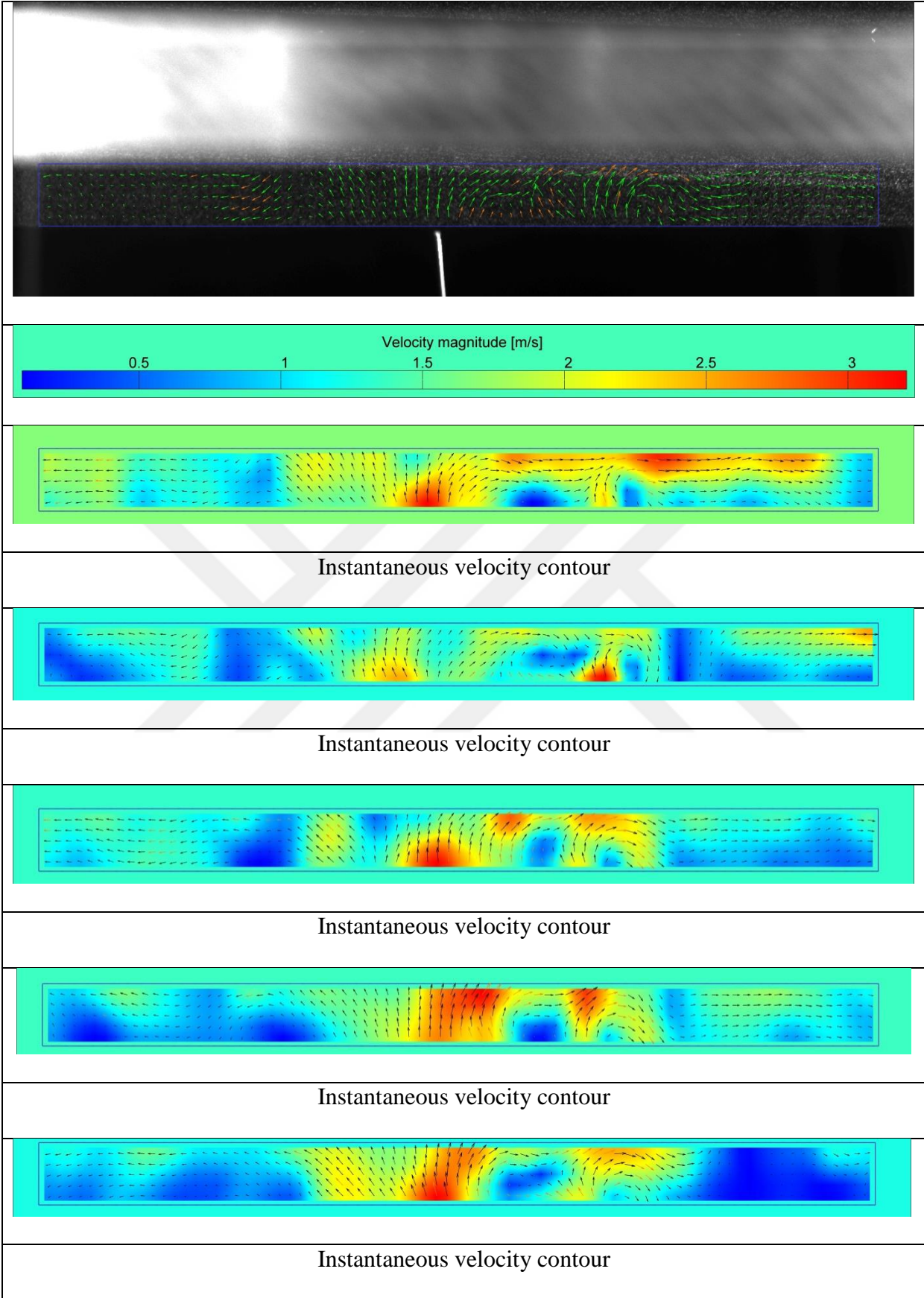
Figure 50: Mylar fan in neutral operational positions (Impinged)

Now the fan is operating in an impinged area, the distance is reduced and the results show that the quality of the formed vortex is not high enough. At least based on what is visible in Figure 50, at the positions near the neutral center line the vortex formation is not strong, although there is a strong forward flow which can be seen the figure and that is what makes the mylar fans effective in the close distances.
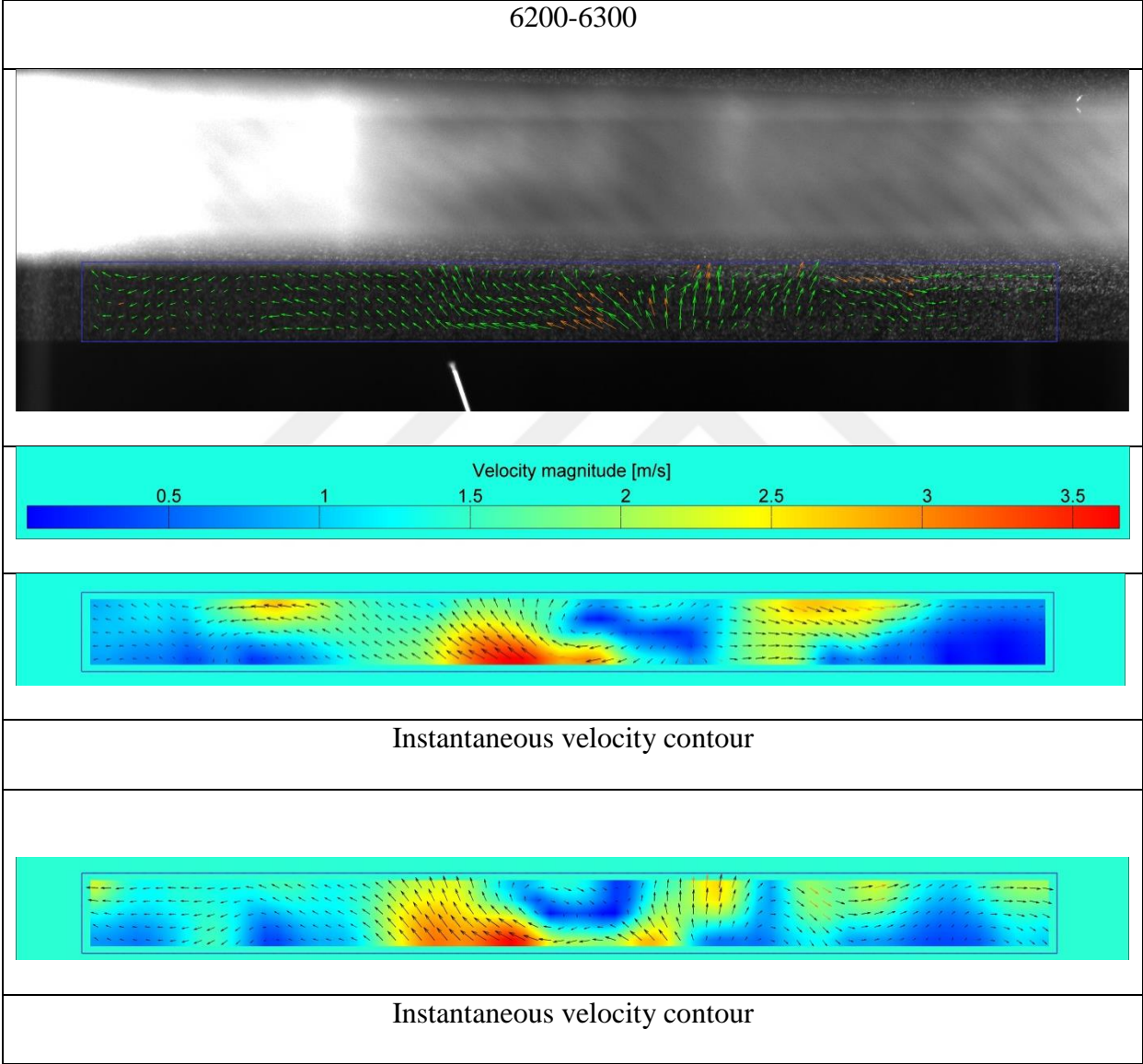
Figure 51**:** Mylar fan in the left operational positions (Impinged)

6600-6700

Velocity magnitude [m/s]

0.5   1   1.5   2   2.5   3   3.5   4   4.5

Instantaneous velocity contour

Instantaneous velocity contour

Instantaneous velocity contour

Instantaneous velocity contour
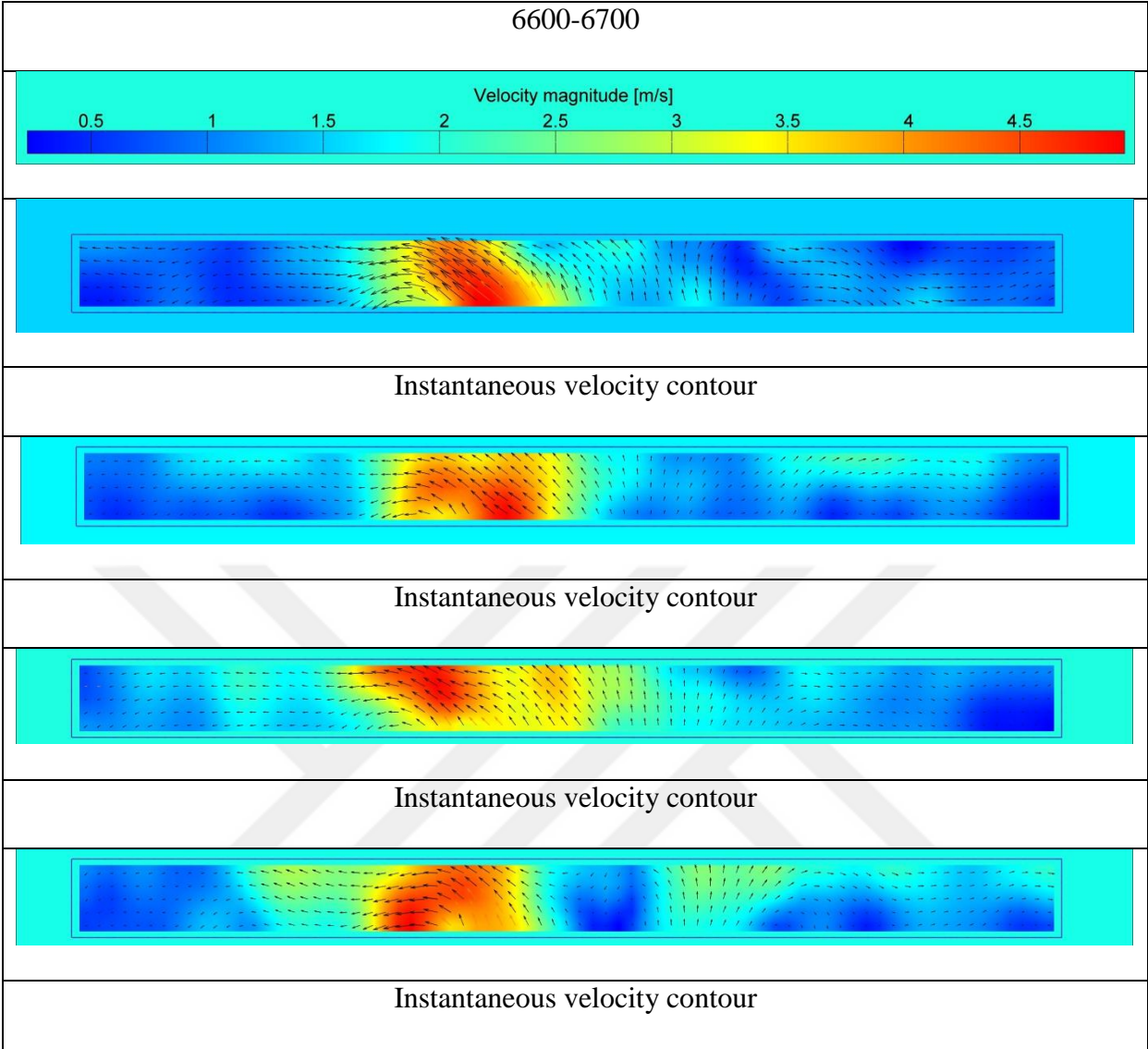
Figure 52: Instantaneous velocity contour on the left side operational positions

6700-6800

Instantaneous velocity contour

Instantaneous velocity contour
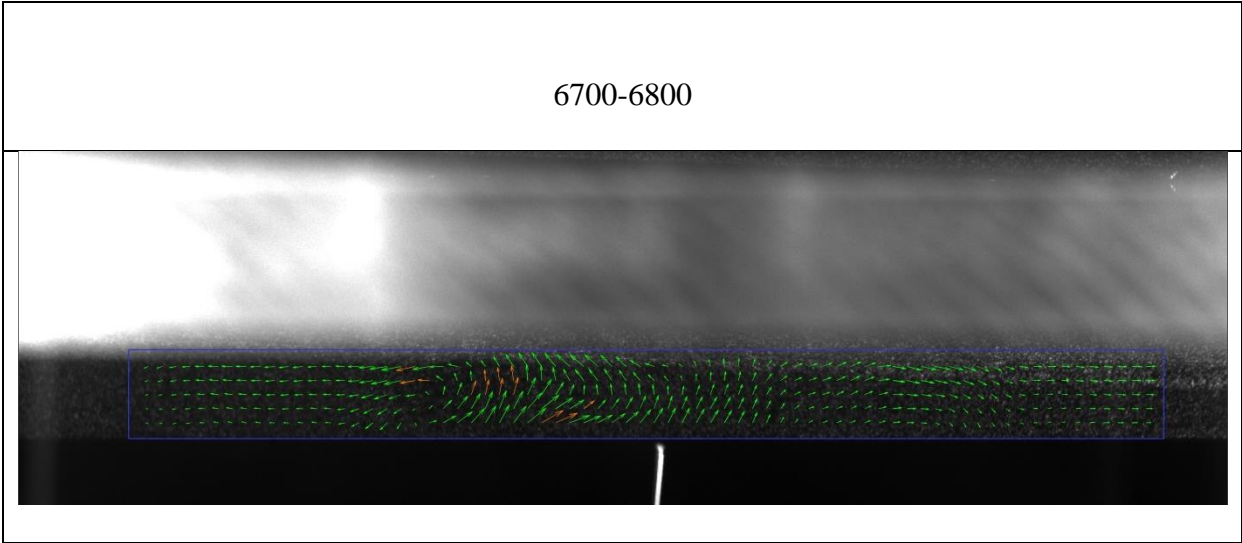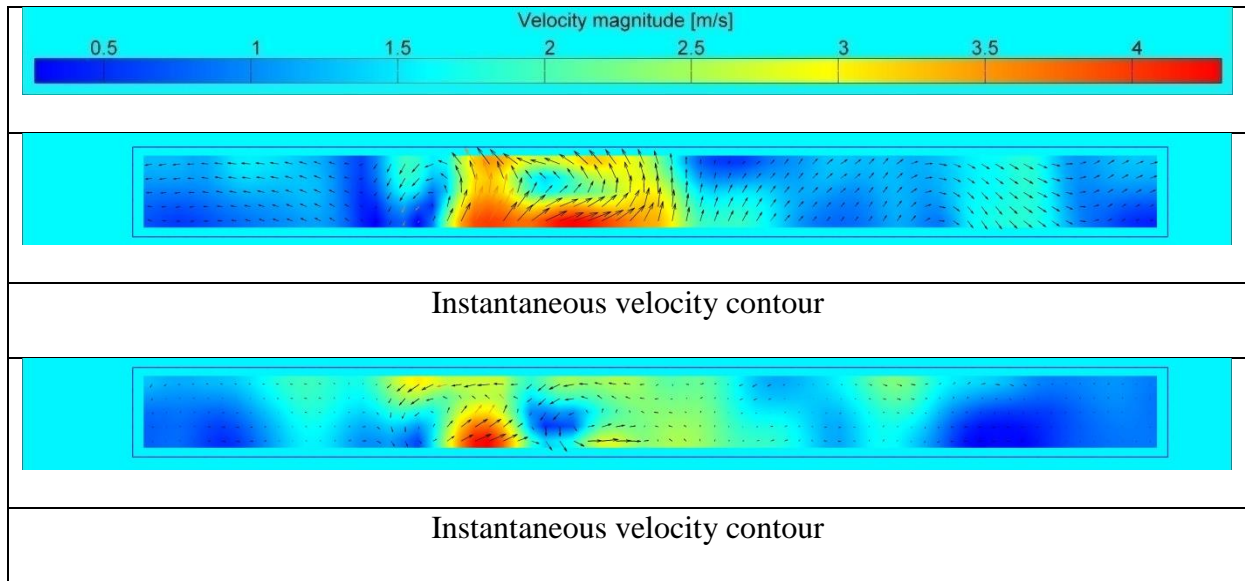
Figure 53: Mylar fan in the neutral operational positions (Impinged)

6800-6900

Instantaneous velocity contour

Instantaneous velocity contour
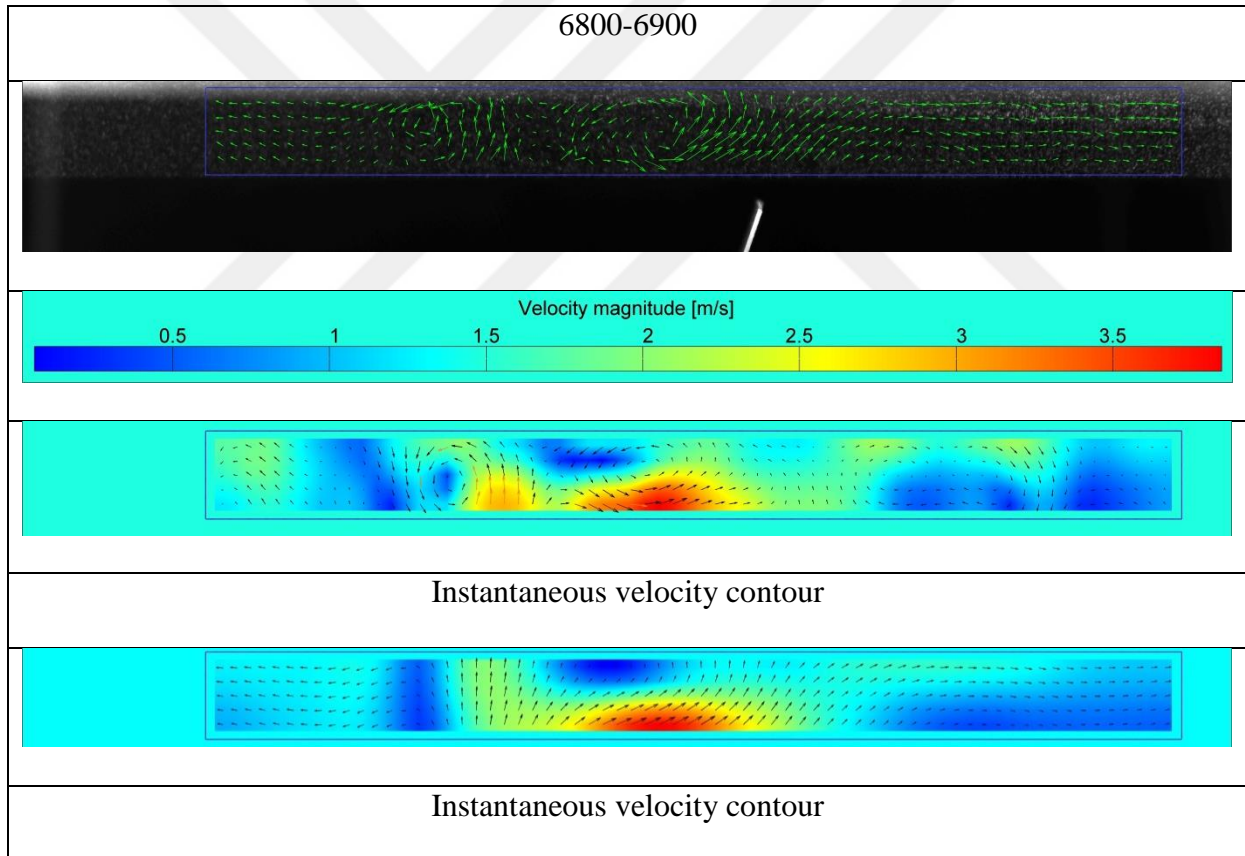
Figure 54: Instantaneous velocity contour on the right side operational positions

6900-7000

Instantaneous velocity contour

Instantaneous velocity contour

Instantaneous velocity contour
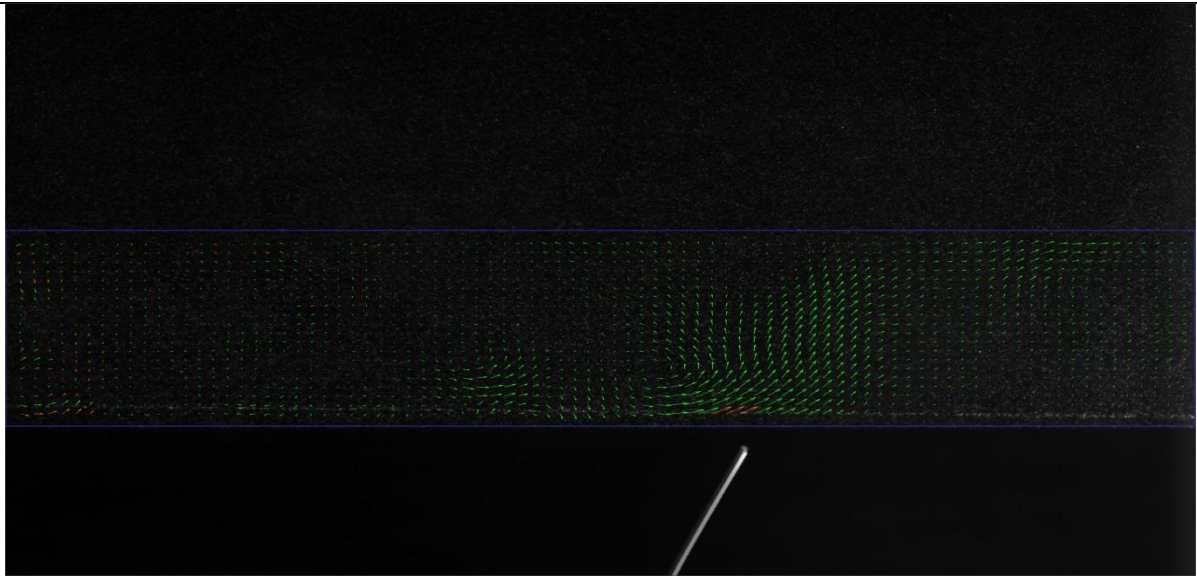

Instantaneous velocity contour
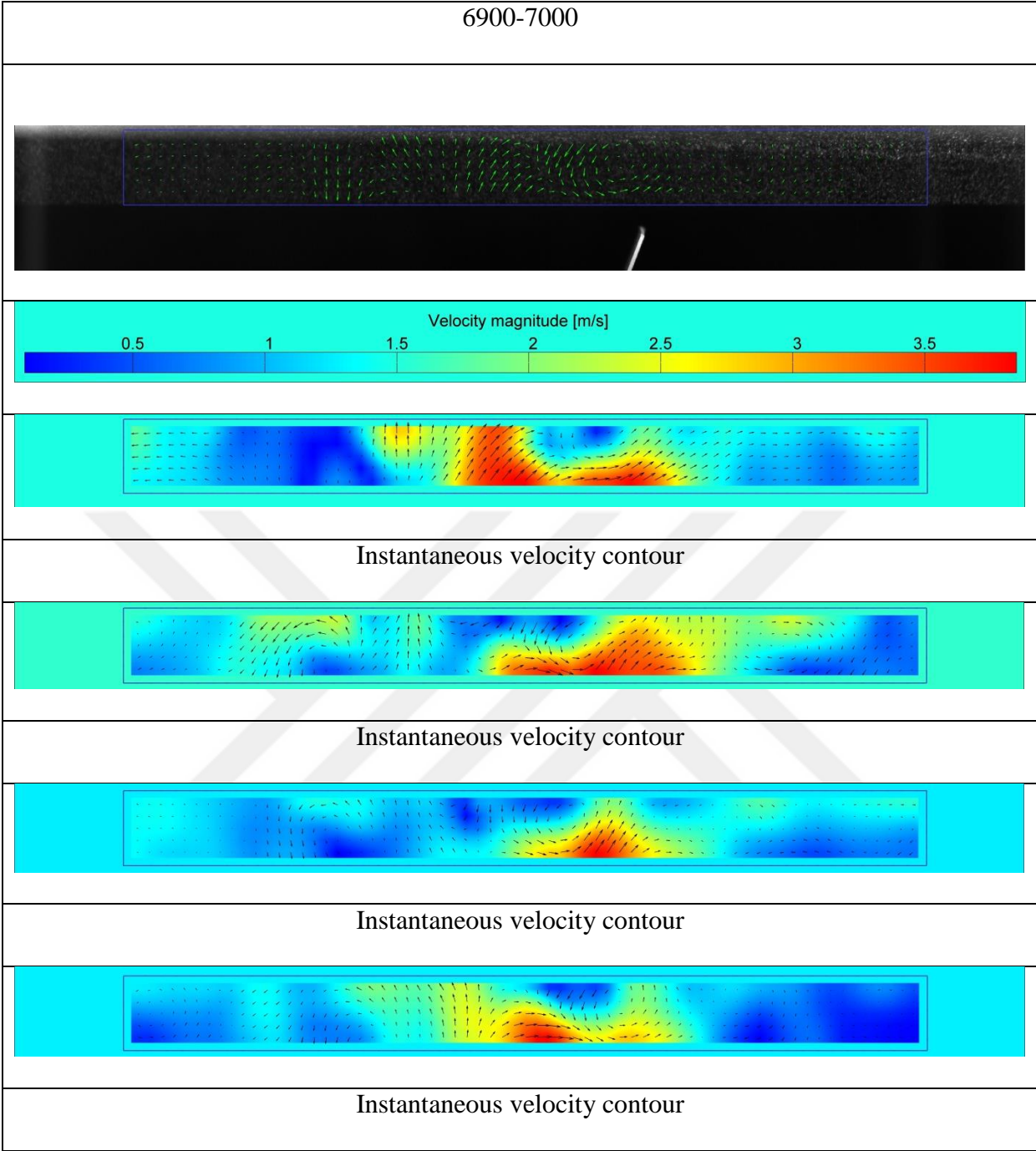
Figure 55**:** Mylar fan in the extreme right operational positions

Figures 51-55 shows the limited area of effect for the mylar fan operating in the impinged areas. The area is limited but the direction of the high power red zone in these cases is not inclined which is a good sign. Since if the induced flow is inclined towards the sides then the cooling performance is wasted. This phenomenon is studied in the upcoming parts of this chapter.

3.2.4 PIV results for mylar piezoelectric fan

Images were collected for two different conditions: free and impinging. In the latter case, the presence of a wall limits the flow field, as shown schematically in Figure 38. This wall is added to study the effect of distance on the vortex generation of the fan. In this section results are shown and analyzed.
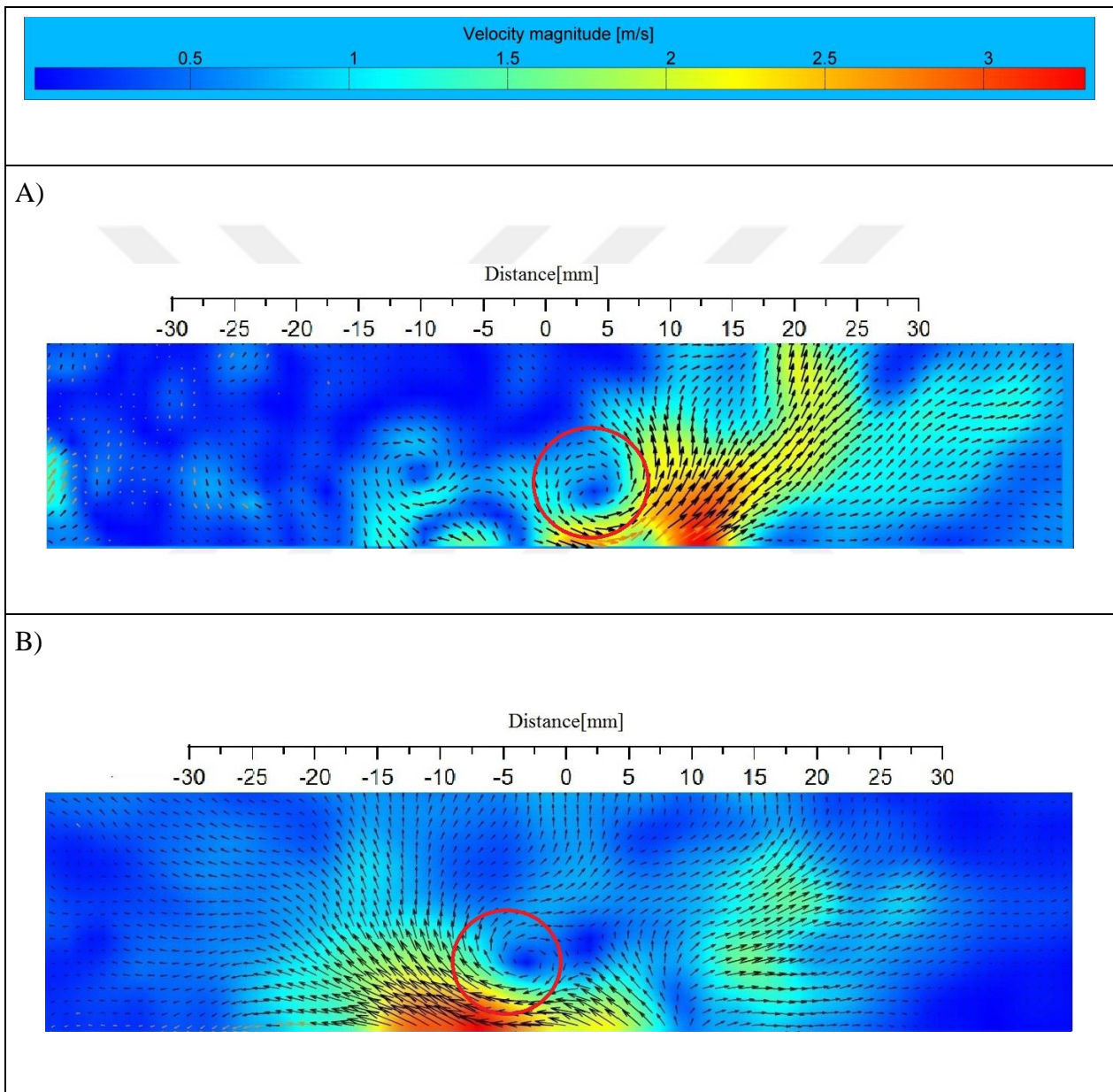
Figure 56: Instantaneous velocity contours and vectors for the free piezoelectric fan , A) Fan is at position 1, B) Fan is at position 2

Figures 56A and 56B show the flow field while the beam is at positions 1 and 2, respectively. In each case, a pair of counter-rotating vortices develops at the slab tip during a cycle of vibration. In Figure 56A, the vortex has been generated (designated with a red circle), and it is about to detach from the tip of the slab. In Figure 56B, this same vortex has moved to the right side of the centerline, and it continues its path while progressing away from the fan. Meanwhile, a new vortex is generated with the opposite rotational direction on the left side of the centerline (again designated with a red circle). This flow behavior repeats due to periodic movement of the slab. It is evident that in the free working condition of the piezoelectric fan, the vortices move towards away from the centerline. This deviation conveys more flow to the sides, meaning that momentum and mass flux are carried away from the impingement target.
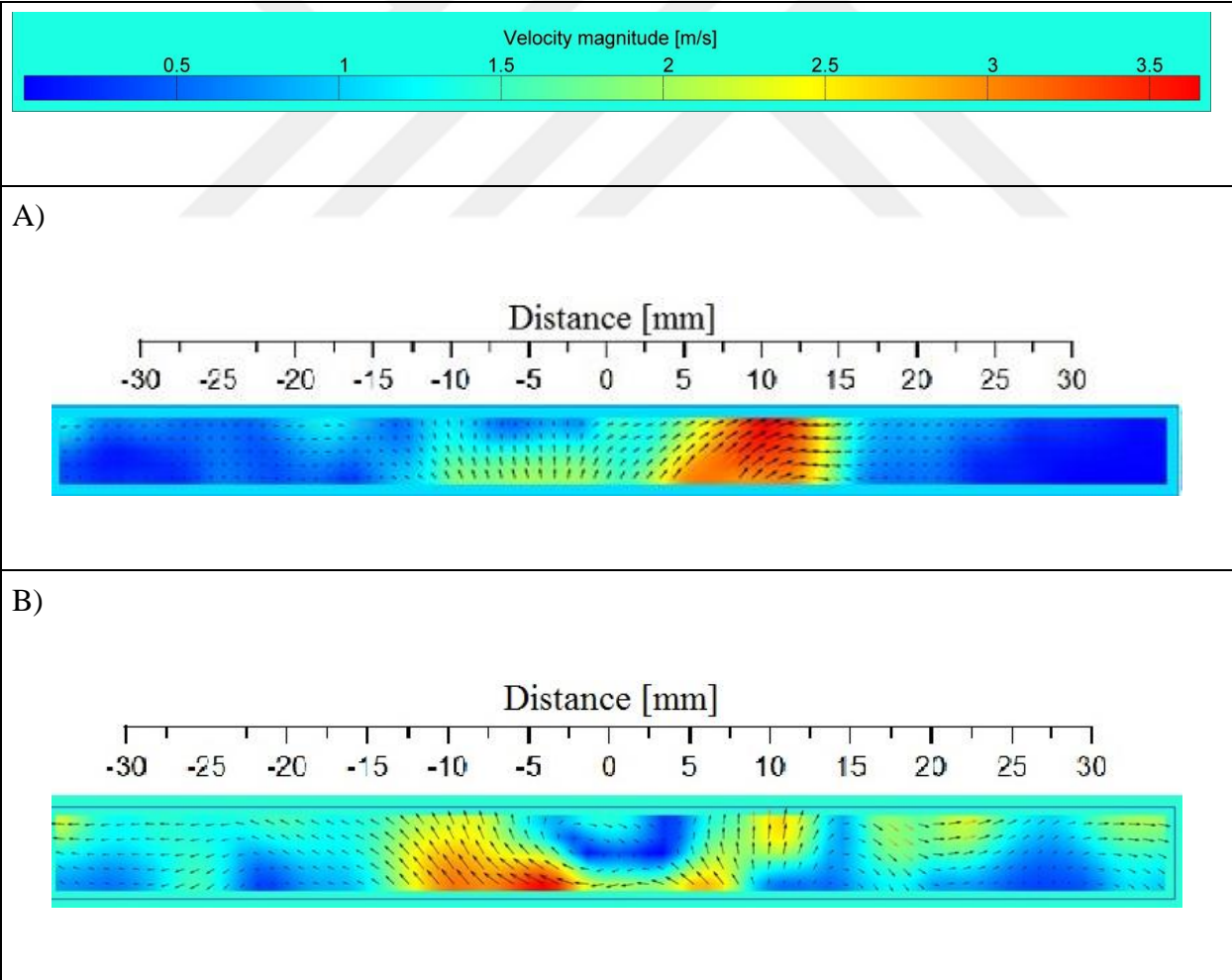
Figure 57: Instantaneous velocity contours and vectors for the impinging piezoelectric fan at

G/A = 1 A) Fan is at position 1 , B) Fan is at position 2

Figure 57 shows the instantaneous flow fields for the impinging case while *G/A* = 1. Here, the vortex from the fan tip reaches the wall before it completely separates from the tip. The existence of the wall prevents the vortex from complete formation.

Figures 58A and 58B depict the time-averaged velocity vectors for *G/A* = 2 and 1, respectively. For the case of the wall placed at *G/A* = 2, a stagnant flow region is observed at -12<*x*<12 mm. In addition, the flow is directed towards regions where *x*>12 mm and *x*<-12 mm, after which it forms a wall jet. Recall that the heater is located at -12.7<*x*<12.7 mm for the heat transfer study. This means that close to the location of the heater, we observed a stagnant flow. As a result, no significant forced convection occurred. This is the main cause of the significant degradation of the heat transfer at *G/A* = 2.
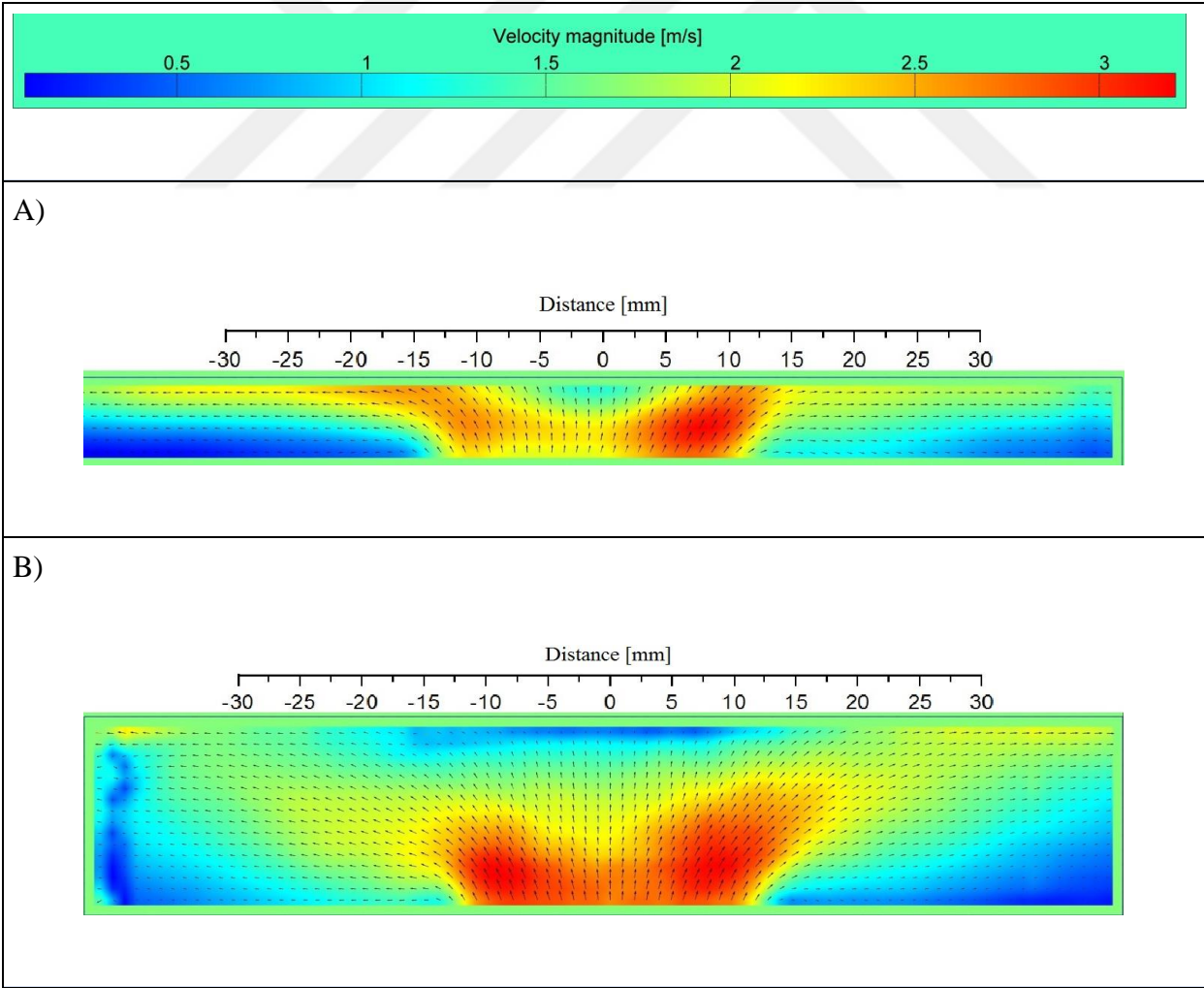
Figure 58: Time averaged velocity vectors and contours for A) G/A = 1 and B) G/A = 2.

At the closer distance with G/A=1, in the region of -7<x<7 mm, there is a low speed flow regime, though speeds are higher than at $G/A=2$. On either side of this region, there is a stronger wall jet, particularly when compared to the more distant position. In this case, the flow impinges much more closely to the heater, rather than diverging on either side. Hence, the heat transfer is improved.

3.2.5 Intermediate conclusions for the mylar piezoelectric fan

An experimental study has been performed to understand the heat transfer and underlying flow physics for a thin piezoelectric fan cooling a vertical surface. Based on these experiments, we have several conclusions:

1. The experimental data show an inverse relation between heater-to-fan distance ratio (G/A) and the heat transfer coefficient.

2. The maximum forced convection heat transfer coefficient is observed at the nearest location, $G/A = 0.5$, and largest voltage, V_{pp}=112 V. The resulting Nusselt number was around 20. This means that at the best operating conditions, the enhancement factor above natural convection is around 2.2, which is low compared to synthetic jets.

3. From the PIV measurements, if the heater is close to the tip of the piezoelectric fan, a higher portion of its surface will be exposed to the induced flow. Thus, the heat transfer should be higher at the closer distances, as seen in the thermal experimental results.

4. For fan-to-heater spacings with $G/A = 2$, there is a large stagnant region around the heater, which would result in reduced heat transfer. This flow features high-magnitude velocity vectors directed towards the sides of the heater rather than its center, which would likely result in non-uniform heat transfer.

3.3 High speed camera flow visualization experiments

Based on the achieved experimental and numerical results, it is evident that the formation and decay of the vortices designate the heat transfer. Thus, alongside with the numerical simulation and the experimental tests, it is decided to investigate the real time operational flow visualization of the piezoelectric fan.

In order to capture the vortices and the eventual decay and re-formation within the flow, two categories of requirements should be facilitated; first a high speed capturing device. The fan tip oscillation is a fast paced movement. In order to capture the various stages of each cycle of operation, a PHANTOM high speed camera is used. The reason is that the high speed camera can capture up to 5000 frames per second (fps). This much of data enables a thorough investigation to be performed on the flow behavior around the piezoelectric fan tip. In the current study the maximum fps used is 1000 fps. The PHANTOM camera captures the sequence of the operating piezoelectric fan as a video. The format of the video is .AVI. This format is then processed via sequencing open-source software (Virtual DUB). By the use of this software, the AVI videos are divided into a series of images. These series are then visually investigated.

The second matter of needed facility is a device to make the flow -around the fan tip- clear for the camera. Since the piezoelectric fan is operating in the air, there is no visible trace for the affected flow around the fan. Thus a set of apparatus is used to make a visible flow. In favor of making the effect of piezoelectric oscillation behavior in a flow visible, it is needed to have an arbitrary flow that is being altered by the operation of the piezoelectric fan. This flow should be captured by the camera. The latter is done by the use of laser, while a smoke pen is used to make an arbitrary flow to be affected by the piezoelectric fan. The laser makes a visible green plane (color of the used laser beam is green). This plane is configured with the flow and makes the changes visible to the camera.

Quality of the captured images is dependent on the lighting and the flow density. A poor lighting or a low density flow might result in blurry images. To avoid this problem the flow visualization is repeated at least 3 times for each case so that the best images can be captured.

Flow visualization test system is shown in Figure 59; Set up is consisted from a Phantom high speed camera. Camera is fixed on a calibrated tripod. The piezoelectric is located in a Plexiglas chamber with a square cross section. This chamber helps the smoke made by the smoke pen to have more intensity in the regions of interest; - which is close to the tip of the piezoelectric fan in this case- while making the capturing more precise. The chamber improves the flow investigation by limiting the movement of the induced smoke.

The Plexiglas is a reflective material and this reduces the quality of the captured images, thus while capturing the operation a piece of mate textile is acting as the background of the image.

The DOE for the flow visualization is set in a manner to investigate the effect of the voltage of operation for the piezoelectric and the resulting manifested flow regime. The results are provided along with the hypnosis of the witnessed changes on the vortices.

Table 7: Design of experiment (DOE) for the metallic piezoelectric fan

Case number	Operational voltage, Peak to peak (Volts)	Operational frequency, sequencing rate
Case 1	30	60 Hz, 20 fps
Case 2	70	60 Hz, 20 fps
Case 3	100	60 Hz, 20 fps

As briefly defined in the above table, the variable in the operation of the piezoelectric fan is the AC voltage of the fan, while the frequency is fixed at the resonance value of 60 Hz. The

image sequencing rate of the captured video is 20 frames per second, this value is the default

value in the VirtualDub software. This VD software is used to convert the captured videos to

a set of images. This conversion is necessary in order to track the vortex regime in each of the

designated operational scenarios (Table 1). In the following part, the images are included with

the hypothesis of the acquired vortex behavior.
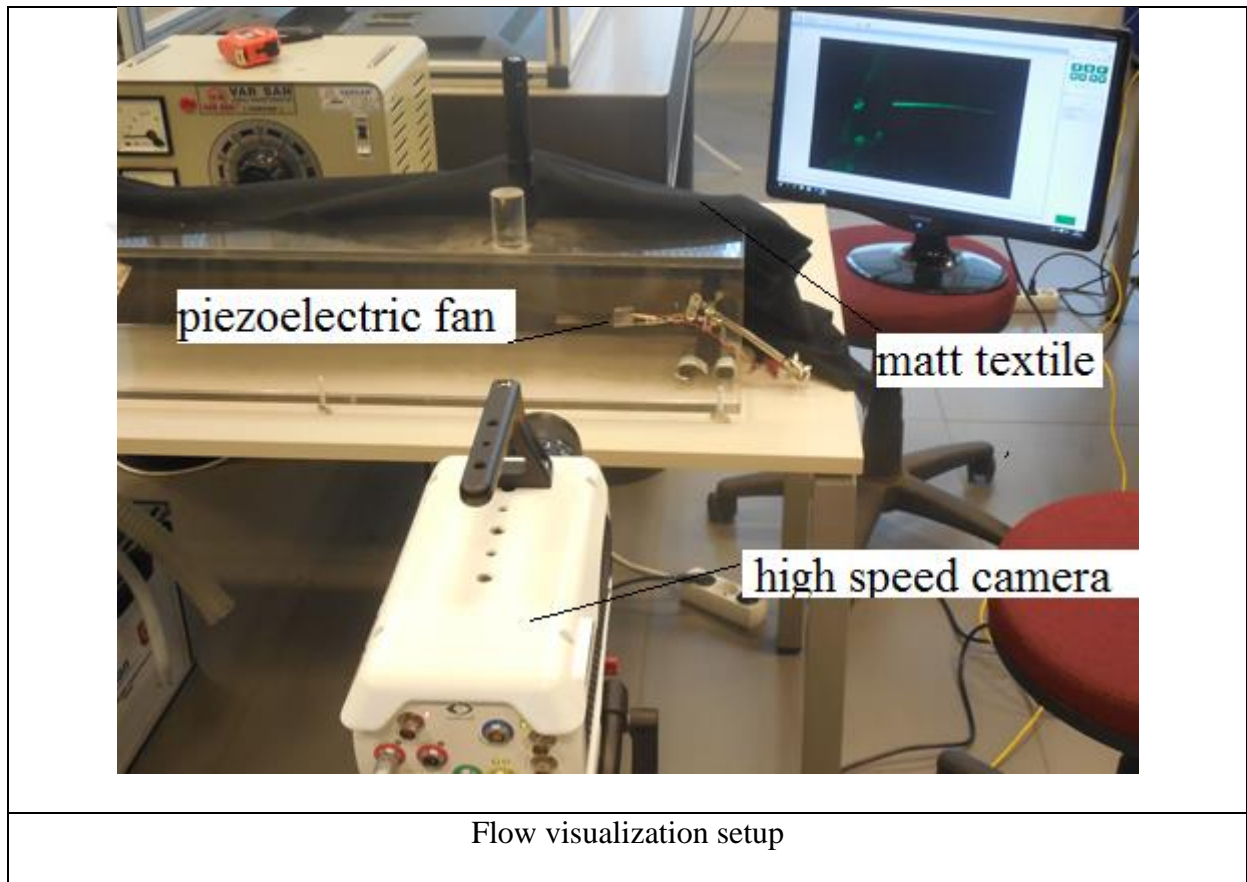
Flow visualization setup
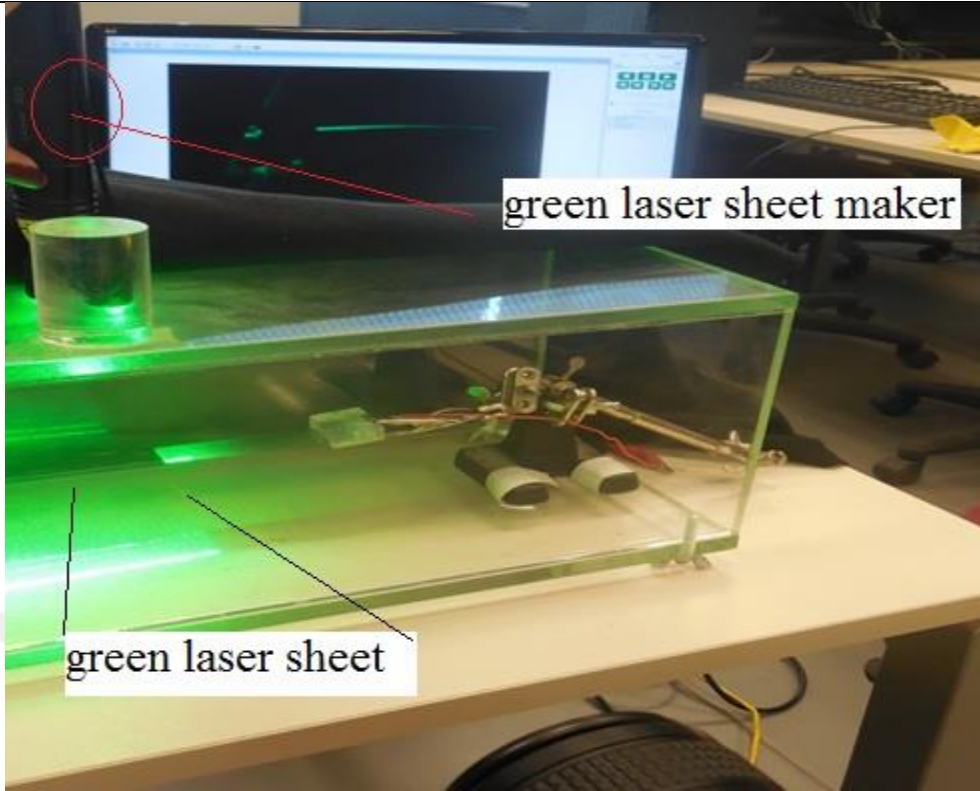
Configuration of the laser sheet maker
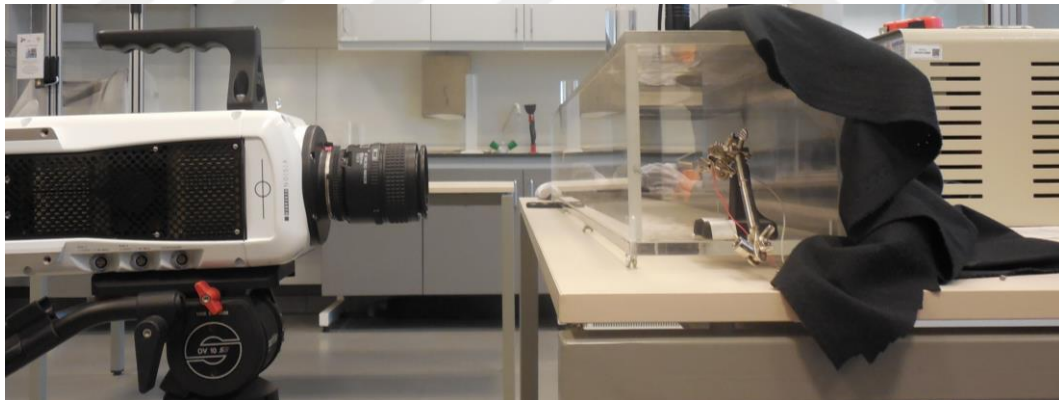
Camera and the chamber configuration
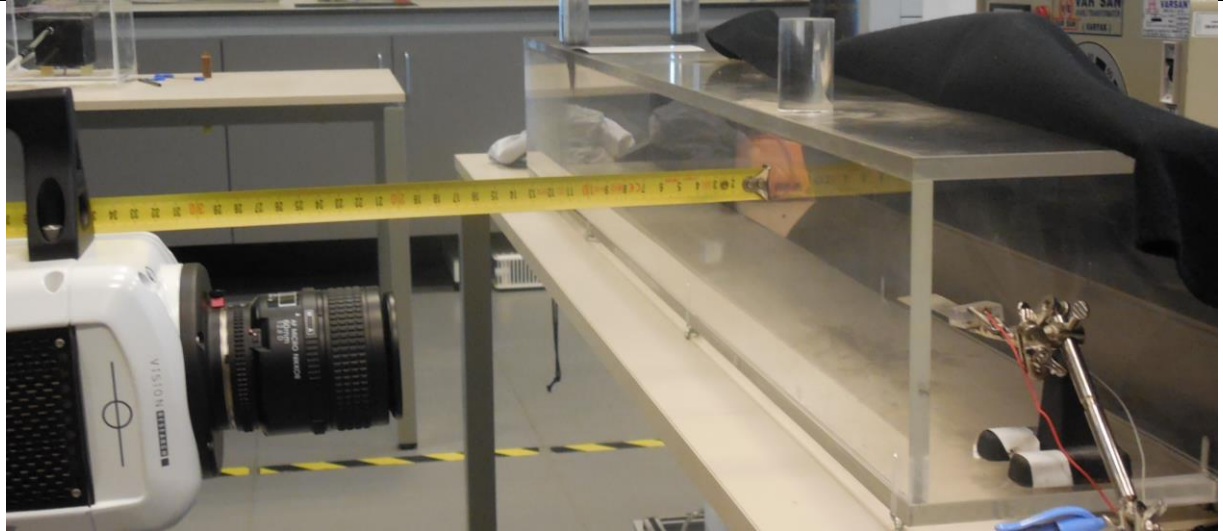
Optimized distance between the lens and the chamber (optimized distance is 20 cm)

Figure 59: Flow visualization setup components

The frame rate is 20 frames per second (fps) for all the captured videos. This means that each image indicates the induced flow in 0.05(1/20) second. The operational frequency of the fan is 60Hz, means the period of full cycle of the piezoelectric fan is 0.02(1/60) second. The investigation is conducted on the sequences based on the period and the visible vortex phenomena quality. Following cases will depict each operational mode exclusively.

3.3.1 Case 1- Operating voltage 30 V_{pp}

The lowest operating voltage in the case of the piezoelectric fan has the lowest deflection respectively. The small value of reflection makes it possible for the camera and available smoke pen to have a good configuration in order to show the vortex behavior.
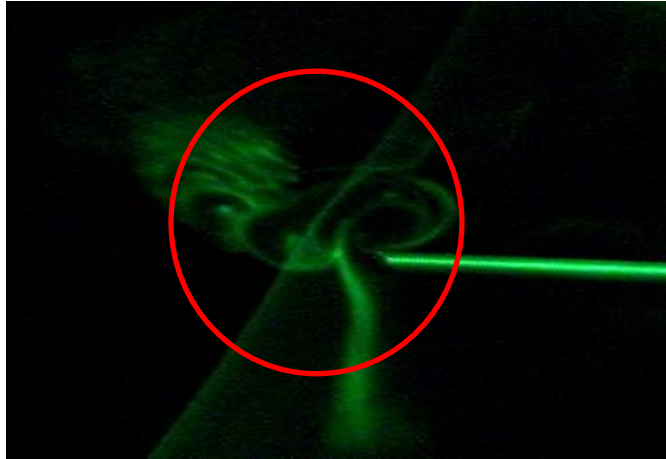
Starting reference image-1

0.5 second later-2
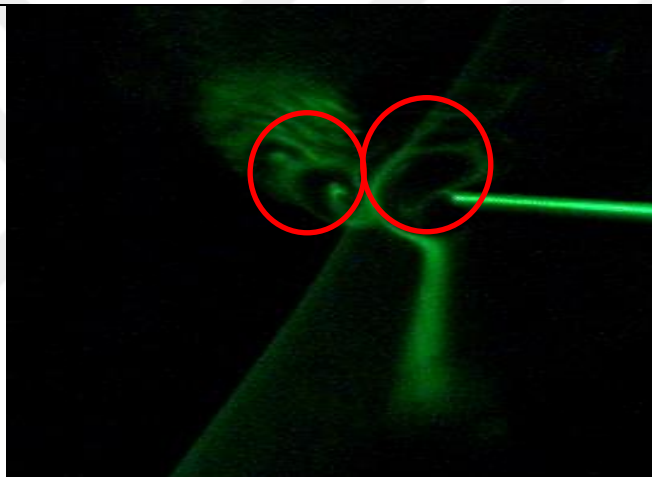
1 second later-3
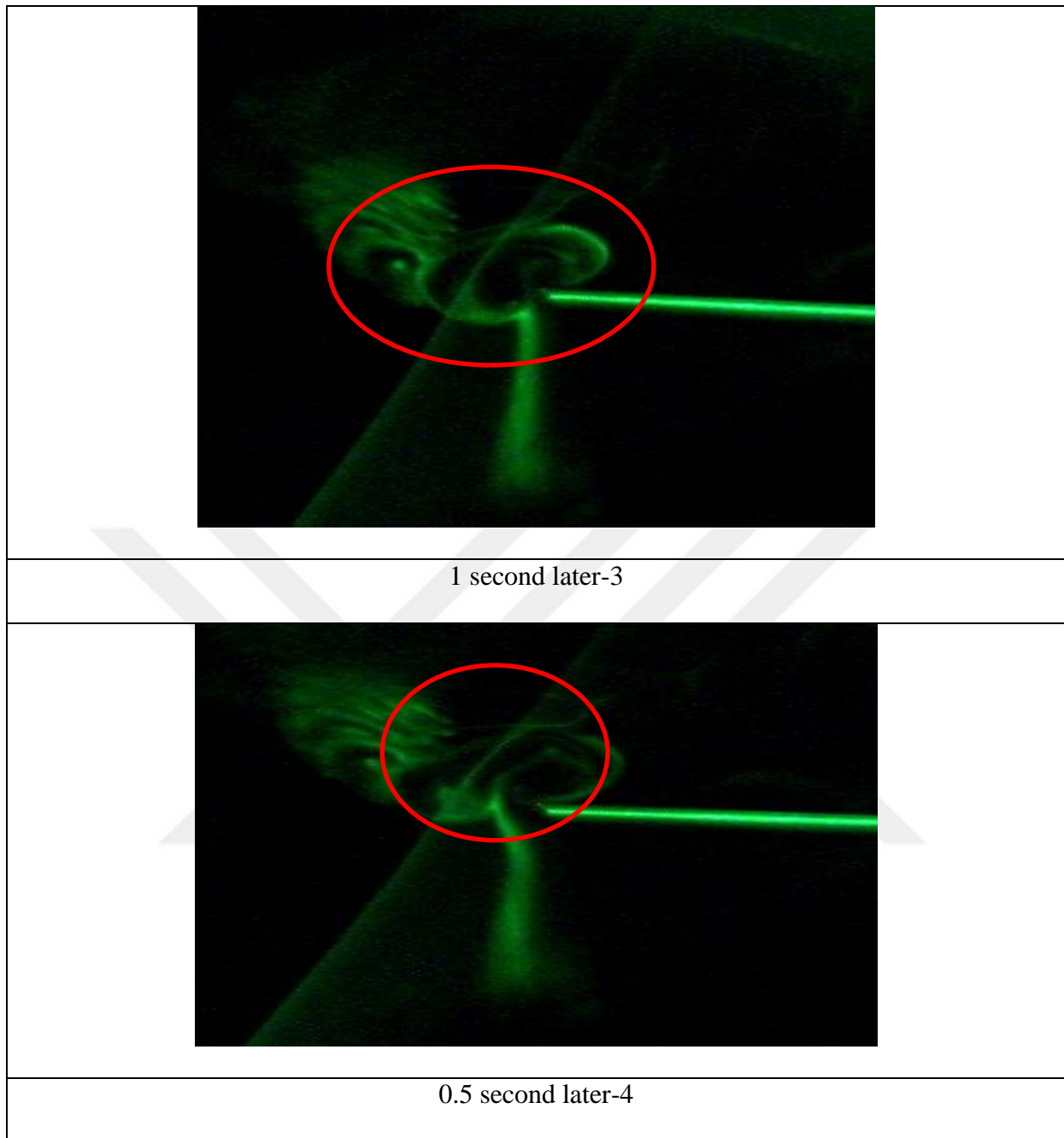
0.5 second later-4

Figure 60: Flow visualization sequence for 30 V_{pp}

Figure 60 shows the cycle of formation and decay of the vortices. In the first image (Figure 60 -1); the vortex is in the midst of forming two independent vortices. 0.5 second later the double vortex, is formed is a symmetric manner. The next pictures repeat the same witnessed behavior of formation.

3.2.2 Case 2- Operating voltage 70 V$_{pp}$

Incremental increase in the next step of the flow visualization is intentionally performed to achieve the goal of observing the effect of voltage variation on the flow regime. It is important to note that the higher deflection due to the higher voltage can cause the image sequencing less accurate in comparison with the previous low voltages. Thus there might be a subtle quality decrease in the performance of vortex capturing.

Starting reference image-1
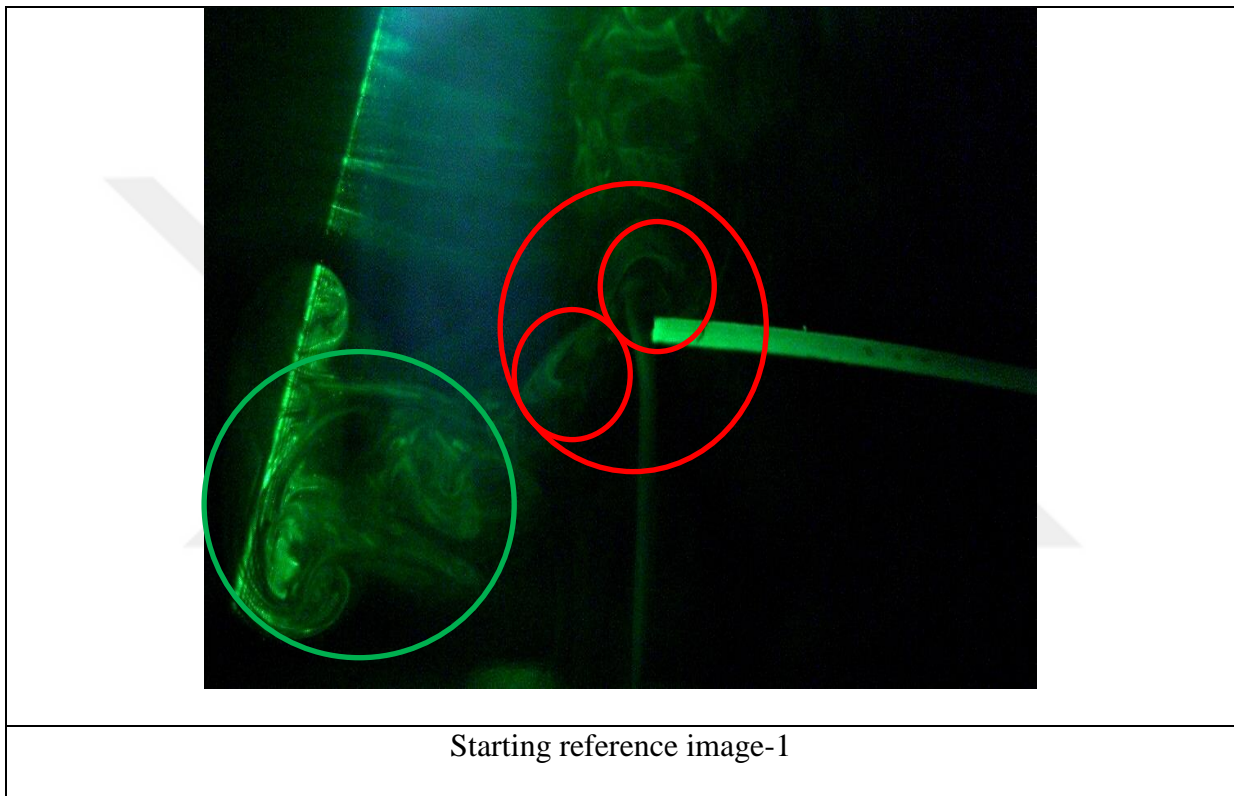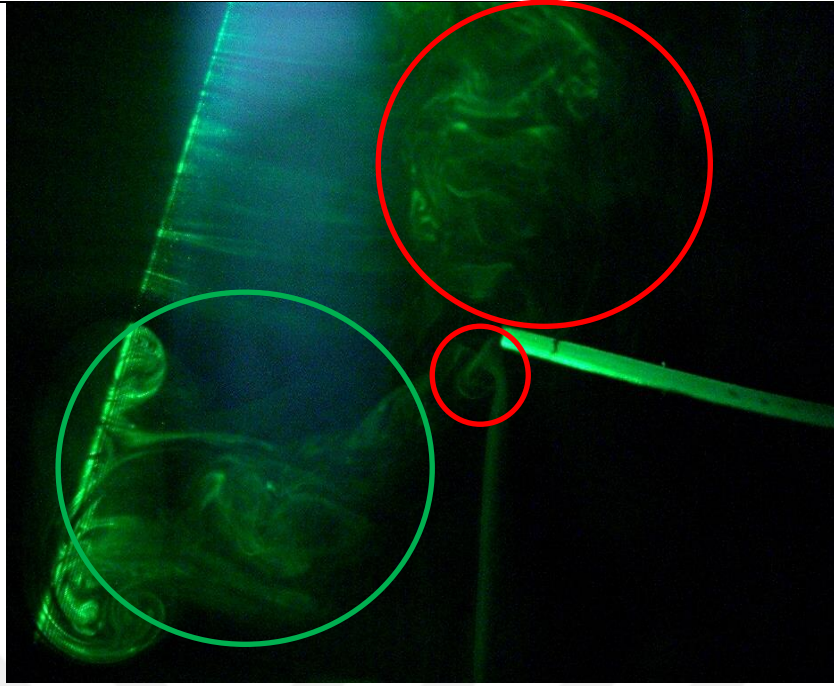
1 second later-2

Approximately 1 second later-3

1 second later-4
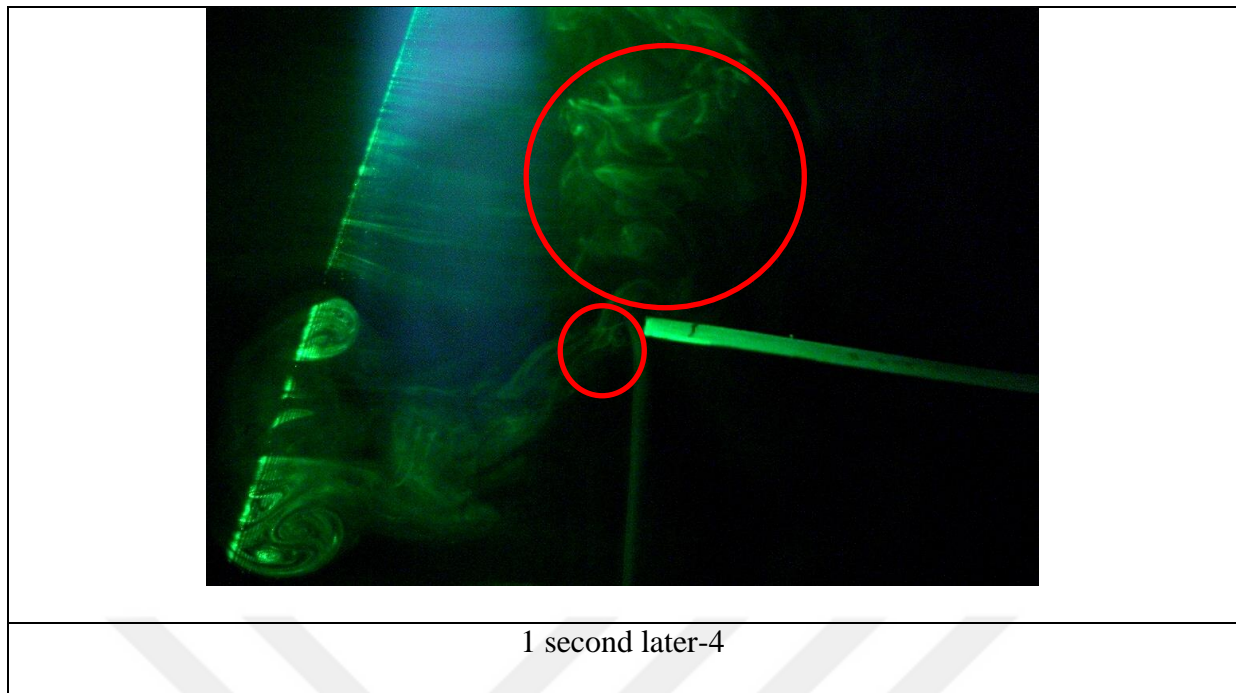
Figure 61: Flow visualization sequence for 70 V_{pp}

Figure 61 summarizes the flow steps captured at 70 V_{pp}. Figure 61-1 depicts two regions designated with red and light green circles. The red circles shows the vortices visible at the starting reference of the operation, while the green circle accentuates the far field vortices made as a residual of the previous operation periods of the fan.

Figure 61-2 shows no change in the green circle area, which means this area, is the result of the smoke pen presence and might not be considered as the region of interest in the next sub-figures. Though this sub-figure depicts decay on the top red circle. Figure 61-3, exhibits the continuation of the decay of the vortices. The button circle which was unharmed in Figure 61-2 is now also decayed. Figure 61-4, confirms the full decay of both of the vortices. The observation on this image shows the pattern made by the top vortex after decay.

The above mentioned images are not recorded based on the single period of the operation, since the generation and decay of the vortices should be visually assessed due to the residual of the previously terminated vortex within the time frame.

3.3.3 Case 3- Operating voltage 100 V$_{pp}$

At 100 V$_{pp}$, it is expected theoretically to have faster behavior that can cause the visual tracking of the flow to be less visible. Although within the acquired images that are shown below the vortex on the top shows the pattern in an acceptable visual way.

The reference-starting image which is designated as 1 in Figure 62 shows two semi-symmetric vortices around the operating fan tip. In the next Figure 62-2 which is 2 seconds later the decay is started and in Figure 62-3 the decay is complete. The last image is the starting of the formation again as the regime is periodic and one vortex is visible on top.
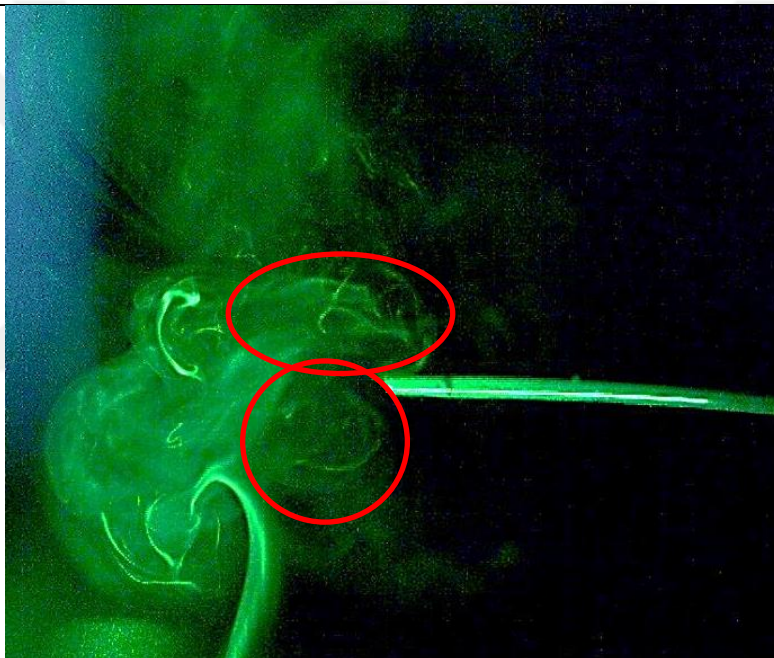
Starting reference image-1

2 seconds later-2

2 seconds later-3

1 second later-4
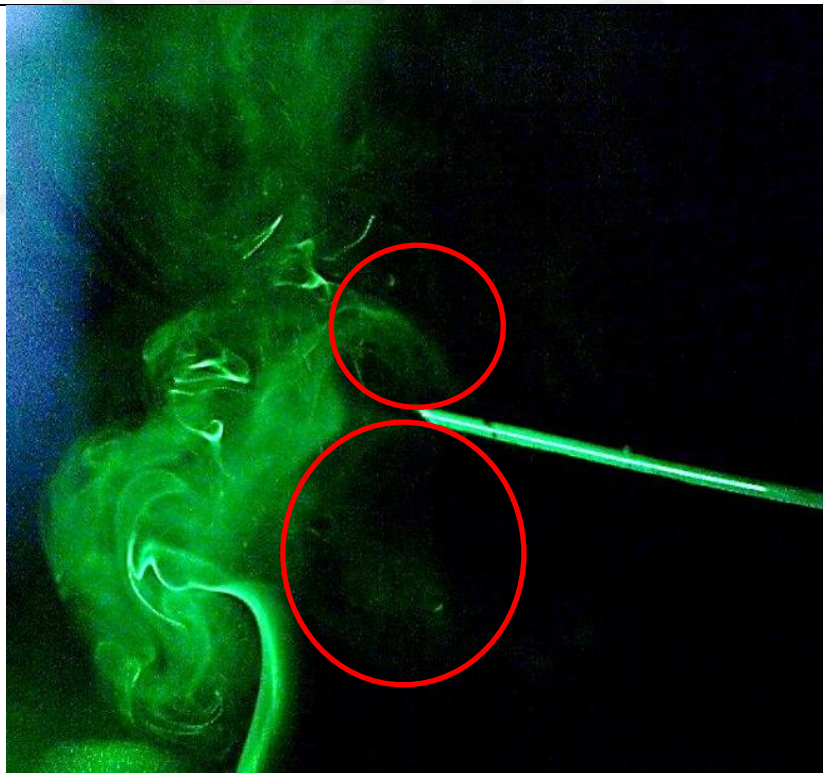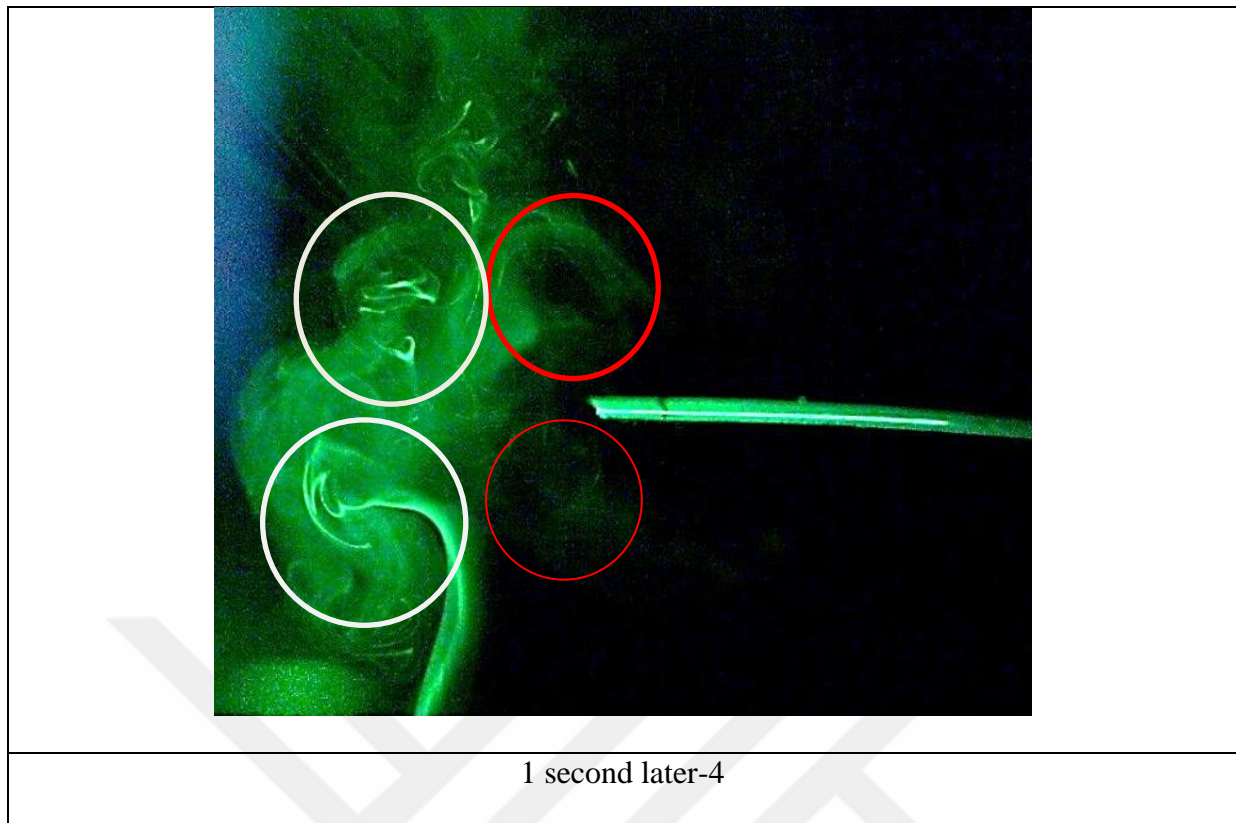
Figure 62: Flow visualization sequence for 100 V_{pp}

One important aspect to note is that the formation-decay also affects the flow after the region around the tip. As exhibited with white circles the after flow is affected by the decay of the last period vortices while the new ones are on the verge of forming. Comparison of the sequence of the obtained after flows are in accordance with the decay-formation trends, observed previously.

3.4 Summary of the flow visualization experiments

Based on the designed DOE, flow capturing is done on the metallic piezoelectric fan, since the value of the deflection during its operation is in a range that is suitable with the high speed camera range of work. In the observed scenarios within the applied voltages the formation-decay regimes are witnessed.

It is evident that the vortices are formed near the tip of the fan due the oscillation of the slab. This formation leads to an eventual decay. The decay is the trigger of the flow traveling away

from the tip of the fan, also the symmetric behavior that is seen in the obtained images are similar to the contours that are achieved by the use of numerical simulation.

PIV measurements also investigated the flow behavior while being confined in a specific distance. The conclusion was the side cooling phenomena that happened due to the restriction of the vortex movement. In the flow visualization part though the confinement effect is not studied and the aim of the visual investigation was to observe the vortex near the tip.

The major finding in the PIV part was the presence of the side cooling. Which means the flow induced by the piezoelectric fan, does not reach the immediate front area, but instead it is reaching the areas on the sides (shown in Figure 63A). This behavior also is observed in the high speed camera images. As shown in Figure 63 B, the vortices formed in this sequence occupy the side regions eventually, rather than traveling along the fan tip immediate front area.

Aside from the side cooling phenomena, the presence of a double vortex is captured on the processed images from the Phantom camera. The different operational conditions in the DOE, are tested and the results are shown. It is observed that the higher values of voltage, enables the piezoelectric fan to have a higher deflection. The higher deflection, results in higher rates of vortex formation and decay. That is the proof of the acquired experimental data presented in chapter 2 and verified with flow visualization methods.

A)

B)
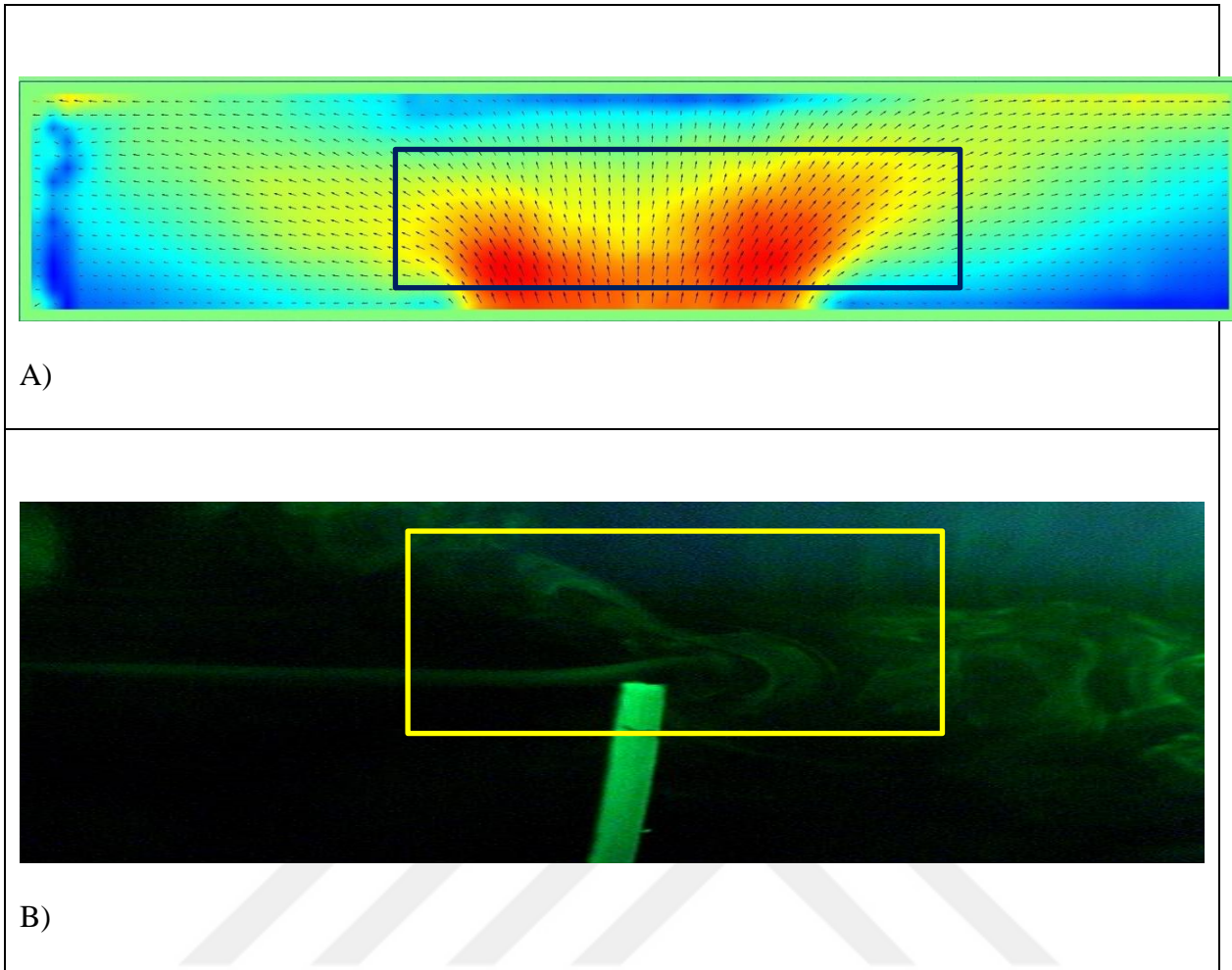
Figure 63: Comparison of the PIV method and high speed camera results
A) Time averaged velocity contours , B) Image sequence acquired with high speed camera

CHAPTER IV

4. COMPUTATIONAL STUDY

The testes that are performed to give a good sense of the margins of the heat transfer characteristics. For having a better understanding of the occurring flow regimes and heat transfer, another approach is to model the operational conditions via numerical models. Computational fluid dynamics (CFD) is a tool which enables us to have a better vision about the fluid related problems. In this chapter the simulation of the mylar piezoelectric fan with the use of the ANSYS-FLUENT software is presented. The simulation is done in 2D to avoid the excessive computation power and the complications associated with the 3D flow simulation.

4.1 Numerical modeling

The piezoelectric fan is modeled numerically to understand its core flow inducement regime. This would depict the heat transfer associated with the related flow fields. In this study, the geometry is assumed to be two dimensional, thus the needed geometry is simplified as shown in Figure 64. The deployed model indicates a surface that has an oscillating line at the center.
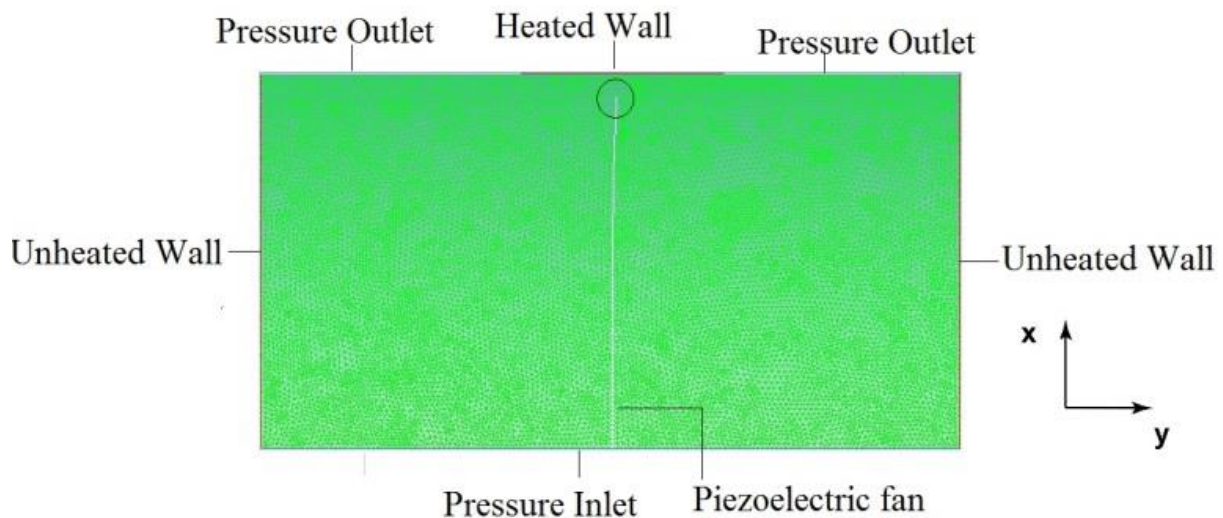
Figure 64: Computational domain, grid and boundary conditions in the CFD study.

The mesh structure for this problem is tetrahedral. Tetrahedral mesh allows a smooth piezoelectric displacement in the numerical flow field. Mesh structure has been generated via using the ANSYS-MESH software. Mesh attributes are being reported in Table 7. The assumptions in the two-dimensional computational model include laminar, incompressible flow with no buoyancy or radiation. The used pressure-velocity coupling scheme was SIMPLE method. To capture the piezoelectric oscillation precisely, a very small time step was deployed. For all the results presented, a time step of 2×10^{-5} s was assigned to the solution.

Table 8: Meshes used in heat transfer model

Mesh attributes	Description
Number of nodes	7560
Number of elements	14028

Mesh sizing is a variable in the modeling problems which should be monitored very precisely in the numerical analysis. The two extremes of the mesh types are coarse and fine. If the mesh is coarse the numerical domain is big so that the precision of the final results might include more error. On the other hand if the mesh is fine, there might be the problem of a high computational power need which will be so expensive to perform. So finding the optimum mesh size, with the highest accuracy possible is a crucial matter for the simulations to be valid.

For this matter various mesh sizes were tested, to see the change in the results. The optimum mesh size is then chosen based on these tests. Although it is important to note that in the problem of the oscillation which is assigned to the slab via the use of the user defined

functions, the mesh size is very critical, a very coarse mesh cannot bear the imposed movement and thus there might be the problem of the negative mesh. This negative mesh does not let the iterations to converge and thus the simulation is not done. On the other side the very fine mesh also has the same problem; the mesh size in this specific problem is linked with the movement definitions. The velocity is the output needed; the mesh sensitivity is then shown in Figure 65.
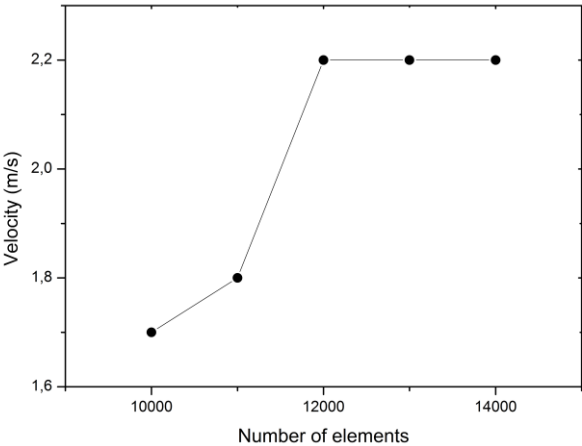
Figure 65: Mesh sensitivity analysis

4.1.1 Numerical findings

The maximum heat transfer coefficient is observed at the region tangent to the tip of the piezoelectric fan; the maximum value is 28 W/m^2-K. This occurred at the centerline of the target plate as shown in Figure 66. This position is where the tip of the fan is at its neutral phase, which means the angel of the oscillation is zero. Heat transfer coefficient shows a symmetric behavior at both sides of the centerline.
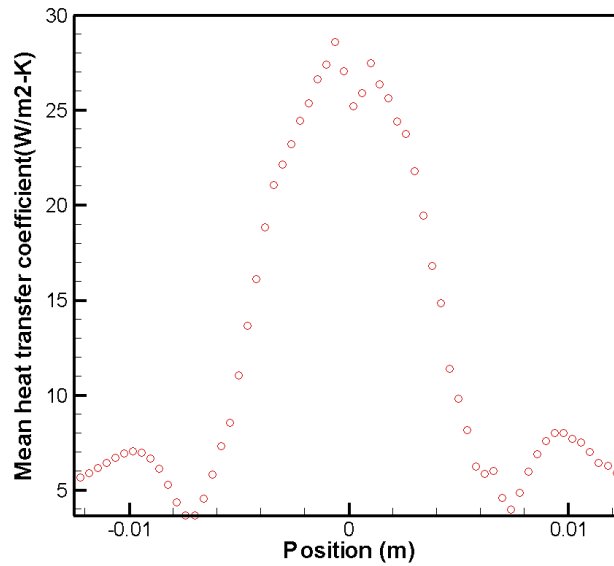
Figure 66: Heat transfer coefficient distribution

The previous data sets depicts that the heat is swept better at the close distances. The heat transfer coefficient distribution also accentuates this test result, which was fully presented in Chapter 2. Figure 66 shows that the maximum heat transfer coefficient is observed at the near fields around the piezoelectric fan tip. Meanwhile at the positions away from the fan tip (as Shown in Figure 66) there is a sudden reduction in the heat transfer coefficient. The symmetric heat transfer coefficient distribution is because of the periodic nature of the slab movement. In Figure 66, there is slight difference between two peaks. This might be because of the oscillation cell definition done in the UDF.

Figure 67 presents the time averaged pressure coefficients on the target plate (heater). It is found that pressure coefficient is the maximum at the centerline. This is due to the symmetric vortex formation in the flow field.

As shown in Figure 66, the maximum achieved heat transfer coefficient is 28 W/m^2-K. This value is observed near the tip of the piezoelectric fan. Along the fan's slab axis. As discussed

in the experimental part, the heat transfer coefficient was collected experimentally around the

value of 21 W/m²-K in the distance of 5 mm away from the heater.
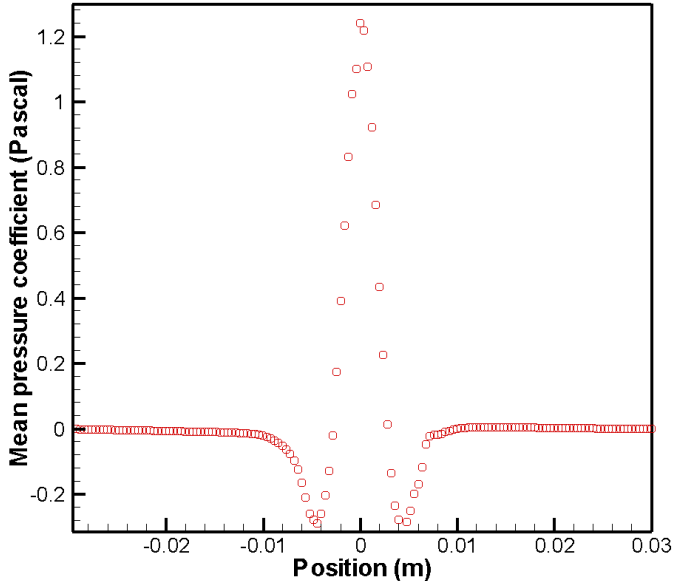
Figure 67: Distribution of the pressure coefficient
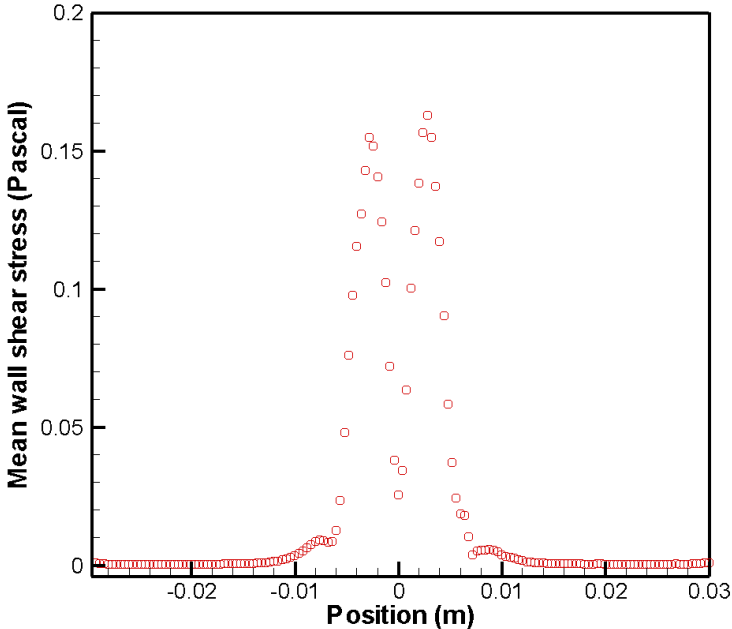
Figure 68: Shear stress distribution

Shear stress designates the achieved velocity gradient at the location that is calculated, Figure 68 shows the mean shear stress at the wall. The position dependency depicts that the shear stress rate is higher at top and bottom of the piezoelectric. This is the reason that there are two peaks in this figure.

Vorticity contours-The vorticity contours have three stages. The neutral stage is where the piezo fan has zero angle of oscillation. The Other two stages are the maximum deflection at the right and left side the neutral line accordingly.

In order to see the vorticity gradient, the neutral position was at the zero angle. Three different stages were studied to obtain a trend in the phenomena of the vorticity with more details.

C)
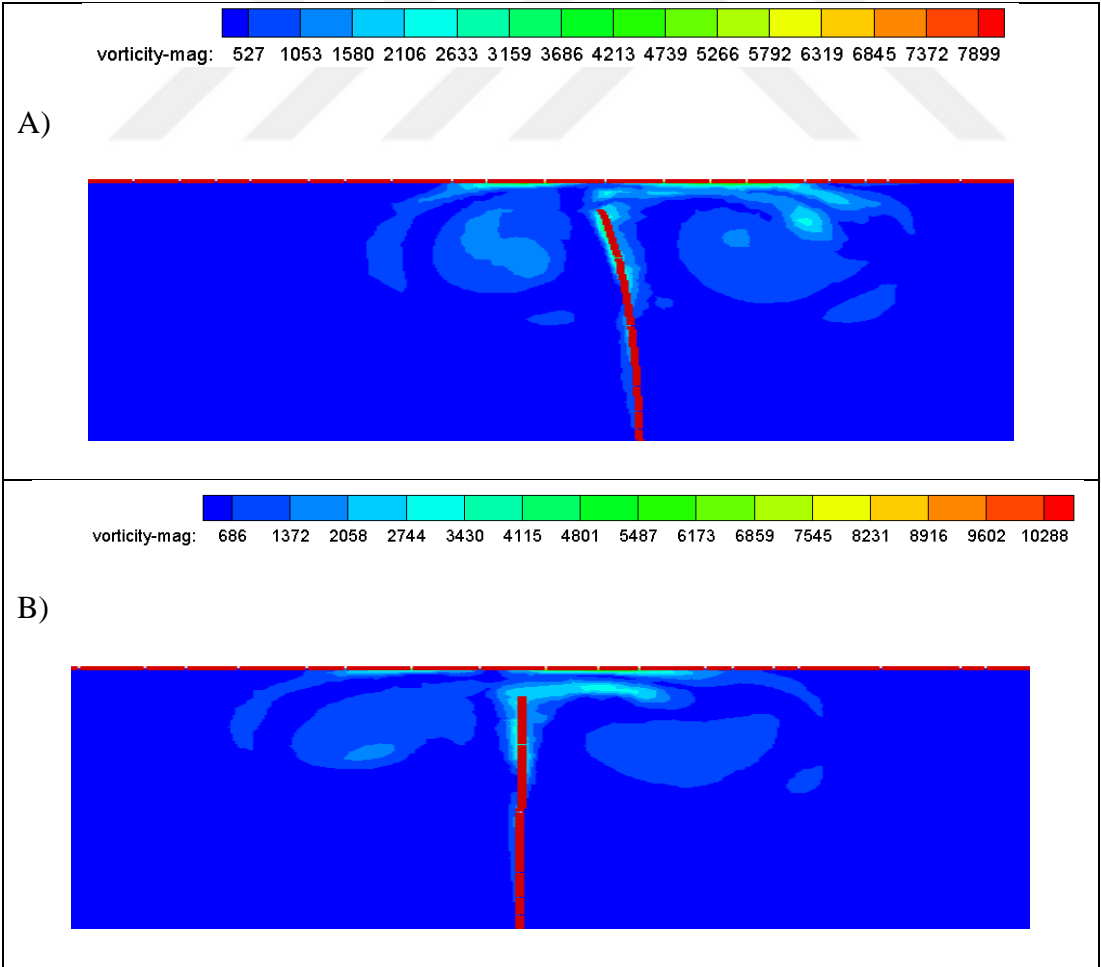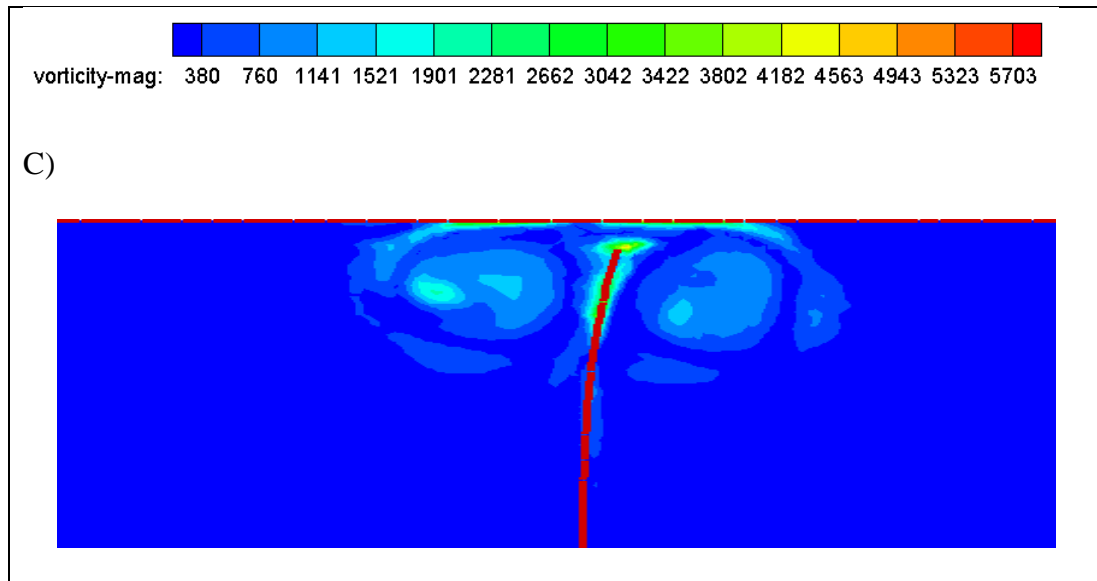
Figure 69: Vorticity contour plots from single cycle of oscillation

A) Fan at the right-side, B)Fan at the neutral position, C) Fan at the left-side

The vorticity gradient has been presented in Figure 69. Vorticity is the measure of speed of rotation. Its unit is one over second (1/s), similar to that of frequency. The reduction in vorticity means that the time needed for the vortex to move is increased, thus less flow will move in a specific time. The less flow will result in lower heat transfer. The highest achieved heat transfer coefficient is near the tip of the fan, which has the highest vorticity.

The highest vorticity happens along the neutral position line (Oscillation angle 0). As the tip oscillates, the vorticity is decreased causing the heat transfer coefficient to drop (See Figure 69). The higher vorticity means higher heat transfer coefficient. Since the value of vorticity is associated with the speed of the vortex, and the low values suggest that the vortex might be slow to travel. A stagnant vortex is not beneficial for the purpose of removing heat, thus this quantity is an indicator of the flow effect on the nearby fields. A high value of vorticity makes the flow nearly turbulent. The degree of turbulence enhances the heat removal due to fast paced flow. The value of vorticity being higher while the fan is at the middle neutral position

(not left nor right) indicates that while the two vortices are coexisting the heat removal is higher than the left or right position. When the fan is operating one of the vortices might start to decay and the heat removal also reduces.

Velocity contours- Understanding velocity distribution is the key to perform heat transfer augmentation. The velocity contours were divided into three stages. These stages include the neutral position, the change in vorticity on the right and left side of the neutral line.

The convective heat transfer is related to the velocity. The understanding of the velocity field gives precise details of the possible range of heat transfer.
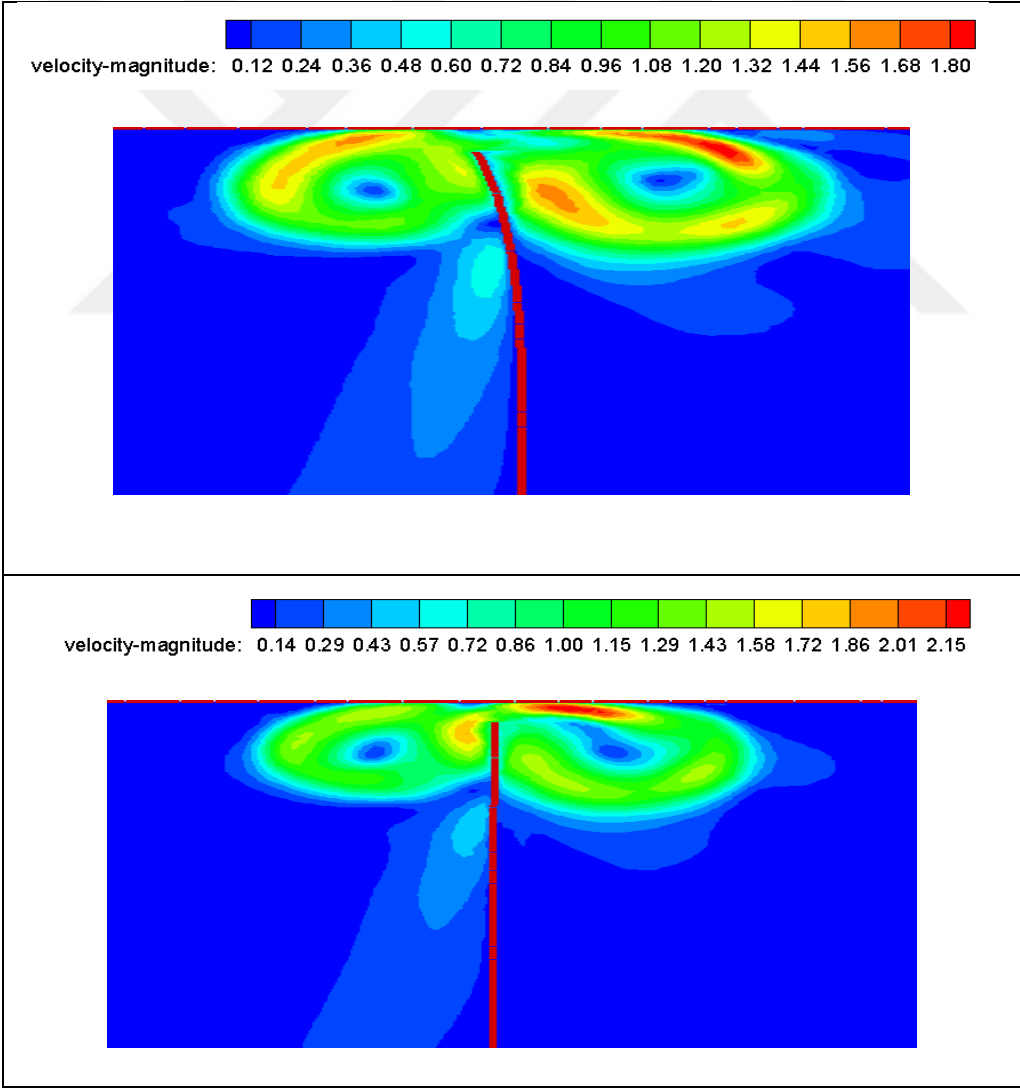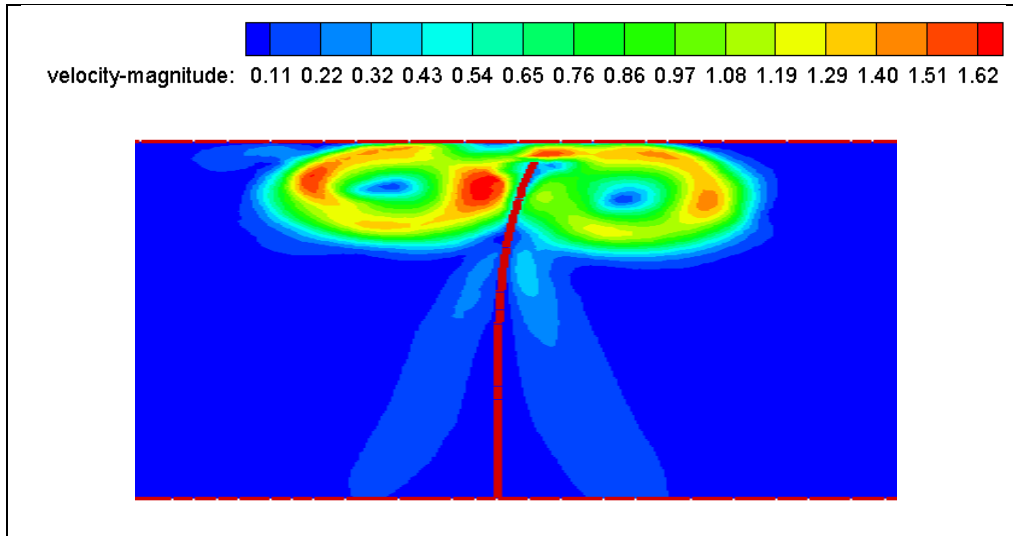
Figure 70: Instantaneous velocity contour plots from single cycle of oscillation. From top to bottom: Right, neutral and the left side position of the piezoelectric fan.

The instantaneous velocity contours show two fully formed vortices around the tip of the piezoelectric fan. The red zones are the high velocity regions. These regions are where the heat transfer happens at its peak. As discussed in the experimental part the areas with the lowest distance value, have the highest heat transfer coefficients.
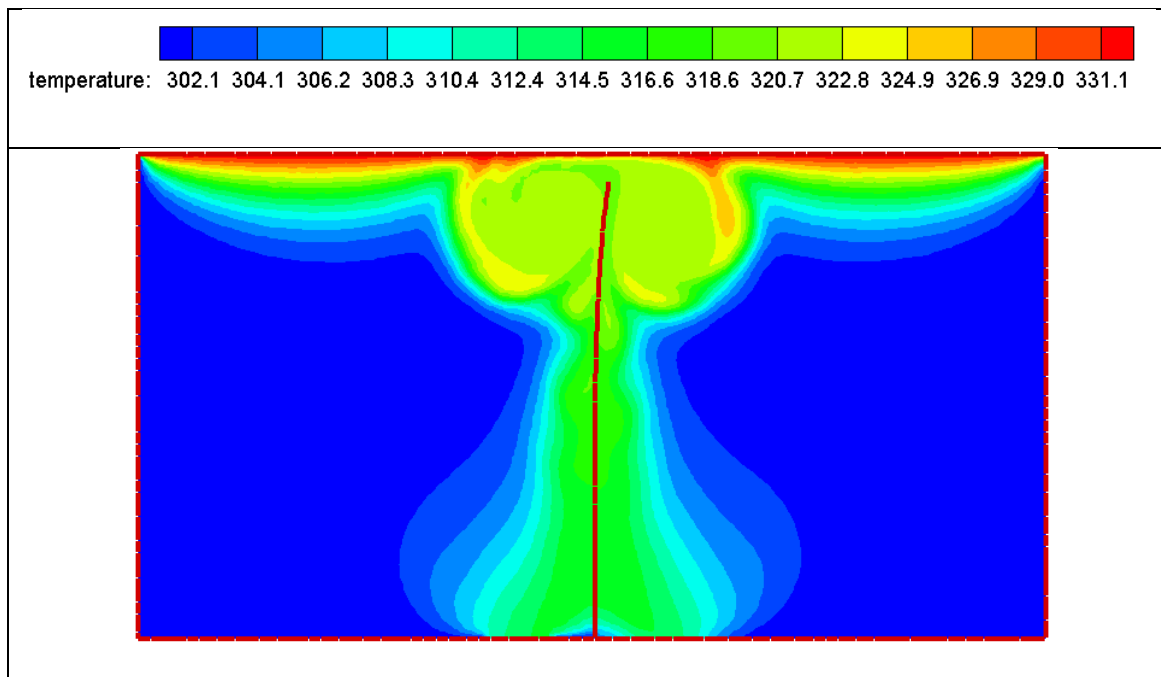
Figure 71: Local temperature distribution contour

As shown in the previous vorticity and velocity contours (Figures 69-70), the tip oscillation creates two vortices around the piezoelectric fan tip. The double vortex form of the flow, dictates the heat to be swept from the heater in the same manner. This means the expected temperature drops should also be symmetric around the fan tip region. The resultant temperature distribution of the operating piezoelectric fan is depicted in Figure 71.

The peak temperature drop happens exactly along the piezoelectric fan's tip. This is the region where both of the formed vortices coexist. As seen in Figure 71, the temperature is approximately 320 Kelvin. This region is where the vortices are rotating towards the sides. This means that the formation of the new vortices and the start of the decay for the previously formed ones are happening in this region. The flow movement in this region makes the flow the most active in this region. So the peak temperature drop is happening here accordingly.

4.1.2 Summary and conclusions for mylar piezoelectric fan experiments

An experimental and numerical study has been performed for a vibrating cantilever beam. In this study the experimental and numerical studies are presented. In the numerical simulations the contours of velocity and vorticity are exhibited. The shear stress and the mean heat transfer coefficients are also calculated near the vibrating beam.

The following conclusions are drawn based on the current study;

1. Strouhal number is used as an indicator of the rate of the vortex shedding. The values are below 10e-4.therefor, the vorticity shedding is not so fast, as has been seen during the simulation. This would imply that the frequency of the vortex shedding in this case is tremendously low.

2. KC number for this case is below 10, implying that the particles which are part of the flow with low KC numbers are not capable of traveling away from the tip in a considerable order of magnitude.

3. Convective coefficient in the numerical study was found to be 28 W/m^2-K while it is 21 W/m^2-K in the experimental study

 4. Maximum velocity is found to be 1.6 m/s for the mylar piezoelectric fan.

The above mentioned conclusions would suggest that the piezoelectric fans are most profitable when used at close distances from the heat source.

CHAPTER V

5. SUMMARY AND CONCLUSIONS

5.1 Experimental studies

In this study three different cooling technologies have been studied to understand their mechanism of heat sweeping. In the experimental study all three technologies are tested in the designed heat transfer set up.

In the case of the piezoelectric fan the experimental studies are coupled with numerical analysis. The numerical analysis is done with the ANSYS-Fluent software.

5.1.1 Test results for rotating (muffin) fan

The highest achieved Nusselt number is at the nearest distance while H/D is 5. The highest heat transfer is happening at the same H/D and the value is 12 W/m^2-K. Based on the rotating fan theory of vortex formation, the expectation was so see a reduction in the heat transfer as the fan is away from the heat source. This has been verified by the test results. These fans are not applicable when they are far away since the flow they induced at the distance more than H/D=5 are not strong enough, at H/D with the value of 40 the heat transfer coefficient is approximately 8 W/m^2-K.

5.1.2 Test results for synthetic jet

The synthetic jet flow inducement mechanism, which is based on the periodic suction and blow exhibits quite a different mode of heat transfer. As achieved in the tests the distance does not have a bad effect on the heat transfer coefficient; since the turbulence is made by the formation of the vortices. The vortices need time to be formed in a manner that can have the best heat sweep. This means that for the synthetic jet there is an optimized distance which gives the best performance. This is the observation that is seen in the case of the synthetic jet. For the used Murata synthetic jet, the H/D with the value of 40 shows the heat transfer coefficient of approximately 69 W/m^2-K.

5.1.3 Test results for piezoelectric fan

Piezoelectric fans are tested with two different slab materials. This is done to check the effect of deflection range on the heat transfer characteristics. The materials of these slabs are mylar and metallic. The deflection of the metallic slab is 50 percent more than the mylar slab. Highest observed heat transfer coefficient is approximately 57 W/m^2-K. Heat transfer coefficient of the mylar fan is approximately 21 W/m^2-K. This clearly shows the effect of the deflection on the heat sweeping.

5.2 Numerical (CFD) studies

The piezoelectric fan is studied at the operating frequency of 60 Hz. The deflection of 1.5 mm for a half period was inserted in the macro-UDF. The model is 2D to reduce the numerical complications. Vortex formation is observed at the tip of the piezoelectric fan. Formations are completely symmetric. The average speed of the flow at the highest value is about 2 m/s.

5.3 Future research opportunities

The piezoelectric fan, alongside with the piezoelectric fan and muffin fan is investigated in this study. Experimental and numerical results are presented, based on the results it might beneficial to expand the research in the following areas:

- Muffin fans blade materials can be altered to make their power consumption less, also the usage of new materials in the design of these rotary fans might enable them to operate in a wider range of volumes.

- Combination of the three technologies in order to test if a higher heat transfer coefficient is achievable or not.

- Numerical analysis of the piezoelectric fan can be done in 3D to understand the vortex formation in a more precise manner.

- A 3D CFD analysis on piezoelectric fan can help identifying a correlation between deflection, frequency and heat transfer accurately.

- The tip design of the fan can be modified so it can reach a higher velocity at its tip.

- Synthetic jets can be tested while being coupled with a backup muffin/ piezoelectric flow guide system. This might be the advent of the next generation of the cooling systems.

APPENDIX A

User Defined function macros, written in the ANSYS macro language.

/**/

/* UDF to compute the orientation of a rotating valve, based on a

   specified rotational speed.

   Christoph Hiemcke, Fluent Inc.,   12 Feb 2004

      butterlfy_flex_UDF = name shown in Fluent GUI

            dt = thread

         cg_vel = cg velocity (global)

        cg_omega = angular velocity (global)

          time = current time

         dtime = time step

                                    */

/**/

```
#include "udf.h"

#include "dynamesh_tools.h"


#define NODE_POS_NEED_UPDATE(v) (NODE_MARK(v)== 1)

#define NODE_POS_UPDATED(v) (NODE_MARK(v)=2)


#define  omega     1.0      /* rotational speed, rad/sec      */

#define  R1        150      /* radius of the arc, meters      */

#define  R2        -150
```

```
/**********************************************************************/
/*

    UDF to define a horizontal plane.  One will thus be able to project

        boundary nodes upon this plane.


    Christoph Hiemcke, Fluent Inc.,        12 Feb 2004        */
/**********************************************************************/


DEFINE_GEOM(plane, domain, dt, position)
{
        position[1] = R1;
    position[2] = R2;
}


/**********************************************************************/
/*

    UDF to define a wall that is initially a circular arc, but then

        oscillates sinusoidally with time.


    alpha = angle that dictates the motion of the arc;

        theta = angle that corresponds to the position of the rotating valve


    Christoph Hiemcke, Fluent Inc.,        13 Feb 2004        */
/**********************************************************************/
DEFINE_GRID_MOTION(Amp10mm, domain, dt, time, dtime)
{
 face_t f;
```

```c
Thread *tf = DT_THREAD ((Dynamic_Thread *)dt);

real NV_VEC (dx);

real NV_VEC (origin), NV_VEC (rvec);

int n;

Node *v;

real sign;

real omg=2*M_PI*60;

real x[ND_ND];

real A1 = 42.340240609312495;

real A2 = 33.489096289515;

real A3 = 20.731702720199146E6;

real A4 = 90.053419217350402E7;

real A5 = 10.2652982820938027E9;

real A6 = 60.344964920192045E9;

real AMP = 0.00003175;

real VEL;


/* enforce face thread only */
if (!FACE_THREAD_P (tf))
  return;


/* set adjacent cell zone as deforming */
SET_DEFORMING_THREAD_FLAG (THREAD_T0 (tf));
if (!NULLP (THREAD_T1 (tf)))
  SET_DEFORMING_THREAD_FLAG (THREAD_T1 (tf));
```

```c
/* set theta-dot*/

VEL = sin(omg*time);


Message ("time = %f, sign = %f\n", time, sign);


/* set origin of cantilever rotation */

NV_D (origin, =, 0.0, 0.0, 0.0);


/* loop over all faces of dynamic thread */

begin_f_loop (f, tf)

  {

    /* loop over all nodes of face */

    f_node_loop (f, tf, n)

      {

        /* get node pointer */

        v = F_NODE (f, tf, n);

        /* if node has not been moved then move it */

        if (NODE_POS_NEED_UPDATE (v))

         {

           /* do vector subtract of origin from node coords to get radius vector rvec */

           NV_VV (rvec, =, NODE_COORD (v), -, origin);


           NODE_COORD
(v)[0]=(A1*pow(rvec[1],2)+A2*pow(rvec[1],3)+A3*pow(rvec[1],4)+A4*pow(rvec[1],5)+A5
*pow(rvec[1],6)+A6*pow(rvec[1],7))*AMP*VEL;


           /*Message("node coords X = %f\n",NODE_COORD (v)[0]);

           Message("node coords Y = %f\n",NODE_COORD (v)[1]);*/
```

124

```
            /* mark node as updated */

            NODE_POS_UPDATED (v);


        }

      }

    /* recalculate face areas etc */

    Update_Face_Metrics (f, tf);

  }

 end_f_loop (f, tf);



}



/**************************************************************/

/*                                                          */

/*      End of the UDF.                          */

/*                                                          */

/**************************************************************/
```

APPENDIX B

Open PIV MATLAB codes sample

```matlab
function im = openpiv_imread(handles,filenum)
% openpiv_imread encapsulates all the image reading functions
% that can be imread for 'jpg','bmp', etc. or 'tiffread2' for TIFF
% images from Insight (tm)
% Usage:
% >>  im = openpiv_imread(handles,file_number);
% >>  imshow(im);

try
   im = imread(fullfile(handles.path,handles.files{filenum}));
catch
   tmp = tiffread2(fullfile(handles.path,handles.files{filenum}));
   im = im2double(tmp.data);
end

if ndims(im) == 3
   im = rgb2gray(im);
end

% Custom pre-processing of images, default = 'imadjust'
preprocess = get(handles.checkbox_preprocess,'Value');
if preprocess
   prepfun = str2func(handles.preprocess);
else
   prepfun = @(x)imadjust(x); % default is to stretch the image
end
im = prepfun(im);
```

```matlab
function [res, filt_res] = openpiv_filter(res,numcols,numrows,outl)
% openpiv_filter(res)
% filters the results of the openpiv processing
% of two images using the 1) global filter, 2) median filter
% and also stores the data in several files
% VEC file with the filtered and interpolated data
% TXT files with the raw, not filtered and not interpolated data
% Last modified: Feb 24, 2016
% Author: Alex Liberzon alex dot liberzon at gmail dot com
%


% Reshape U and V matrices in two-dimensional grid and produce
% velocity vector in U + i*V form (real and imaginary parts):


u = reshape(res(:,3), numcols,numrows);
v = reshape(res(:,4), numcols,numrows);
vector = u + sqrt(-1)*v;

vector(isnan(vector)) = 0;
```

```matlab
% vector = fill_holes(vector);

% Remove outlayers - GLOBAL FILTERING
vector(abs(vector)>mean(abs(vector(vector~=0)))*outl) = 0;
% vector = fill_holes(vector);

u = real(vector);
v = imag(vector);

% Adaptive Local Median filtering

kernel = [-1 -1 -1; -1 8 -1; -1 -1 -1];
tmpv = abs(conv2(v,kernel,'same'));
tmpu = abs(conv2(u,kernel,'same'));

% WE HAVE TO DECIDE WHICH LIMIT TO USE:
% 1. Mean + 3*STD for each one separately OR
% 2. For velocity vector length (and angle)
% 3. OR OTHER.

lmtv = mean(tmpv(tmpv~=0)) + 3*std(tmpv(tmpv~=0));
lmtu = mean(tmpu(tmpu~=0)) + 3*std(tmpu(tmpu~=0));

u_out = find(tmpu>lmtu);
v_out = find(tmpv>lmtv);

% Let's throw the outlayers out:
u(u_out) = 0; u(v_out) = 0;
v(v_out) = 0; v(u_out) = 0;
vector = u + sqrt(-1)*v;

res(:,3) = reshape(real(vector),numrows*numcols,1);
res(:,4) = reshape(imag(vector),numrows*numcols,1);

% Filtered results will be stored in '.._flt.txt' file
filt_res = res;

vector = fill_holes(vector);
res(:,3) = reshape(real(vector),numrows*numcols,1);
res(:,4) = reshape(imag(vector),numrows*numcols,1);

% draw a bit nicer quiver with two colors




% Results visualization
% Only for final, filtered and interpolated data
%    imshow(a,[]);
```

```matlab
%     hold on
%          quiverm(res,2,'g','LineWidth',1);
%          drawnow
%    F(:,fileind) = getframe;

function readURAPIVdata(dirname)
% READURAPIVDATA reads the directory of the experiment,
% where URAPIV saves the output and converts it to the
% 3D matrix of U,V and 2D matrices of X,Y. The files
% would be read and saved: *_flt.txt, *_noflt.txt, *.txt
%
% READURAPIVDATA('Y:\UraPIV\images','flt')
%
% Author: Alex Liberzon
% Copyright (c) 2004, IHW, ETH Zurich
% Last modified: April 23, 2004
%
%

if ~nargin % debug run
    % dirname = 'Y:\UraPIV\images'
    disp('Usage: readURAPIVdata(''E:\aneurism\piv23apr_C001S0003'')');
    return
end

wd = cd;

try
cd(dirname);


direcflt = dir(fullfile(dirname,'*_flt.txt'));
direcnoflt = dir(fullfile(dirname,'*_noflt.txt'));
direc = dir(fullfile(dirname,'*.txt'));
filenames = {};
filenamesflt = {};
filenamesnoflt = {};
[filenames{1:length(direc),1}] = deal(direc.name);
[filenamesflt{1:length(direcflt),1}] = deal(direcflt.name);
[filenamesnoflt{1:length(direcnoflt),1}] = deal(direcnoflt.name);
[junk,i,j1] = intersect(filenamesflt,filenames);
[junk2,i,j2] = intersect(filenamesnoflt,filenames);
ind = 1:length(filenames);
ind = setdiff(setdiff(ind,j1),j2);
filenames = filenames(ind);

filenames = sortrows(filenames);
filenamesflt = sortrows(filenamesflt);
filenamesnoflt = sortrows(filenamesnoflt);
```

```matlab
i = 1;
data = load(filenames{i});
x = data(:,1); y = data(:,2);
u = repmat(0,[length(data),length(filenames)]);
v = u;
u(:,i) = data(:,3);
v(:,i) = data(:,4);

for i = 2:length(filenames)
   data = load(filenames{i});
   u(:,i) = data(:,3);
   v(:,i) = data(:,4);
end

cols = length(unique(x))-1; % notice the directions
rows = length(unique(y))-1;

x = reshape(x,[rows cols]);
y = reshape(y,[rows cols]);
u = reshape(u,[rows cols length(filenames)]);
v = reshape(v,[rows cols length(filenames)]);

save([filenames{1,1}(1:end-14)],'x','y','u','v');

u = repmat(0,[length(data),length(filenamesflt)]);
v = u;
for i = 1:length(filenamesflt)
   data = load(filenamesflt{i});
   u(:,i) = data(:,3);
   v(:,i) = data(:,4);
end
u = reshape(u,[rows cols length(filenamesflt)]);
v = reshape(v,[rows cols length(filenamesflt)]);
save([filenames{1,1}(1:end-14),'_flt'],'x','y','u','v');


u = repmat(0,[length(data),length(filenamesnoflt)]);
v = u;

for i = 1:length(filenamesnoflt)
   data = load(filenamesnoflt{i});
   u(:,i) = data(:,3);
   v(:,i) = data(:,4);
end
u = reshape(u,[rows cols length(filenamesnoflt)]);
v = reshape(v,[rows cols length(filenamesnoflt)]);
save([filenames{1,1}(1:end-14),'_noflt'],'x','y','u','v');

cd(wd);
```

```matlab
catch
    cd(wd);
    error('Something wrong')
end
```

APPENDIX C

Uncertainty Analysis

Experimental studies such as this thesis are prone to wide range of uncertainties. Aside from being experimental many values are measured via the use of apparatuses and devices that each of them has a degree of error embedded. Heat transfer results are acquired under the condition of steady state. This steady state is also assumed to be reached while the fluctuation of the temperature of the heater is less than 1 percent. In many cases the steady state is reached after at least 5 trials, but three best results with the lower deviations are presented in this text. So the reliability of any experimental study depends on low values of uncertainty. This has been elaborately discussed in Moffat [28].

The uncertainty analysis is crucial for the data to be accepted as a correct one, while on the other hand it helps the observer to investigate the possible sources of wrong measurements being identified at the very first stages of the experiments.

The uncertainty analysis results for a case of a metallic fan are presented here. The most crucial value of the heat transfer analysis of the cooling devices is the Nu number. The Nu number is mentioned by Moffat [28] and the related equation used to investigate the error is presented below:

$$\delta Nu = \left[(a_1 \delta Q_s)^2 + (a_2 \delta L)^2 + (a_3 \delta A_s)^2 + \left(a_4 \delta (T_s - T_{amb})\right)^2 + (a_5 \delta k)\right]^{\frac{1}{2}} \quad (1)$$

Where a_i (i=1...5) are the sensitivity coefficients as shown in equation (1). δ shows the uncertainty of corresponding Nu in equation (1) . These coefficients represent the possible uncertainties for each of the values associated with the Nu number.

Major sources of uncertainty for the experiments were identified as the heat losses through the heater holder, temperature measurements and heater power measurements. Although the lateral heat losses were tried to measure by the method of guard heater, but still here the possibility of the presence of uncertainty is assumed to be of importance and calculated. In the

current study, RMS (Root Mean Square) method is used to analyze the uncertainty in the experiments.

Table C1: The uncertainty coefficients definition [28]

Sensitive coefficient	Value
a_1	$\dfrac{d}{A_s(T_s - T_{amb})k}$
a_2	$Nu = \dfrac{Q_s}{A_s(T_s - T_{amb})k}$
a_3	$-\dfrac{Q_s d}{A_s{}^2(T_s - T_{amb})k}$
a_4	$-\dfrac{Q_s d}{A_s(T_s - T_{amb})^2 k}$
a_5	$-\dfrac{Q_s d}{A_s(T_s - T_{amb})^2 k^2}$

The final calculated quantities are Nu and heat transfer coefficients for current heat transfer study which are identical in terms of the uncertainty analysis so only one sample is defined to show the general method of calculation. In Nu number two different types of uncertainties are possible;

• Uncertainty propagated from the measured primary variables.

• Residual piled up uncertainty including the effect of all variable mentioned by Moffat [28]

Propagation of uncertainty is measured using the RMS method using the uncertainty in the primary measured variables listed in Table C2. The values of uncertainty are taken from the least value that can be measured from the equipment. For current study, it is assumed that values of air properties like density, conductivity and viscosity are fixed.

Table C2: The uncertainty and the range of the variables

Primary variables	Absolute uncertainty
$T_{Thermocouple}$ (K)	±0.1
Current(A)	±0.001
Voltage(V)	±0.01
Density(kg/m^3)	Fixed value (1.225)
Air conductivity (W/m-K)	Fixed value (0.0257)
Length, Width, Diameter(mm)	±0.01

Second type of uncertainty is measured by repeating the experiment several times for different operating conditions.

The sample code used for calculating the propagation error is being presented below. As it is shown the variables of the needed results are presented in the code so that the further RMS investigations will be done like a calculator by the use of EES program.

Table C3: Sample EES code for the propagation error calculation of the measurement devices

```
V= 100                                  "Voltage"
I=0.123                                 "Current"
P=V*I                                   "power"
K=0.0257                                "Air conductivity"
T_amb=24.757                            "Ambient Temp"
T_1=59.875                              "Heater Temp1"
T_2=59.884                              "Heater Temp2"
T_3=60.028                              "Heater Temp3"
T_4=60.292                              "Heater Temp4"
T_avg=(T_1+T_2+T_3+T_4)/4               "Average Temp"
T_diff=T_avg-T_amb                      "Temp Differenc"
H_loss=0.024*T_diff-0.0056              "Heat Loss"
H_front=P-H_loss                        "Front Heat"
L_heater=25.4                           "Length of heater"
W_heater=25.4                           "Width of heater"
A=L_heater*W_heater*convert(mm^2,m^2)   "Heater Area"
h=H_front/(A*T_diff)                    "Heat transfer Coefficient"
Nu=h*D/K                                "Nusselt Number"
```

Table C4: Experimental results and (%) error in measured Nu numbers (sample)

Distance(mm)	Voltage peak to peak (V_{pp})	Test 1	Test 2	Test 3	Standard Deviation	%Error
5	100	41.2	46.12	51.11	2.6	1.5
5	110	46.12	52.67	56.17	5.1	2.9
5	120	46.12	56.17	61.23	7.6	4.32
10	100	28.72	32.73	38.9	5.1	2.94
10	110	35.69	38.78	44.3	4.4	2.54
10	120	38.41	42.66	49.8	5.7	3.29
15	100	19.6	25.78	31.05	5.2	3.00
15	110	24.89	31.02	35.4	5.27	3.04
15	120	31.4	34.31	41.2	5.03	2.90

The maximum error found related using standard deviation method is 4.32%, while error from uncertainty propagation is 4.2% (Using the RMS method with the above mentioned EES

code, Table C3). Error calculated from sampling is greater than uncertainty propagation which is why uncertainty in heat transfer using standard deviation is greater that is why 4.32% experimental uncertainty is taken as our uncertainty. Propagation of uncertainty is also included in the uncertainty calculated by the sampling. All the procedure was the same for the measured heat transfer coefficients too.

REFERENCES

[1]   R. F. H., C. A. L. S. H. L., 2010, "Computational and experimental investigations of performance curve of an axial flow fan using downstream flow resistance method," Exp. Therm. Fluid Sci., pp. 827–837.

[2]   McKenzie, A., 1997, Axial Flow Fans and Compressors: Aerodynamic Design and Performance.

[3]   Bleier, F., 1998, Fan Handbook: Selection, Application, and Design, McGraw-Hill.

[4]   Meyer, D. K. C. J., 2001, "Numerical simulation of the flow field in the vicinity of an axial flow fan," Int. J. Numer. Methods Fluids, pp. 947–969.

[5]   Almazo, C. R. a. M. T. D., 2013, "Selection and Design of an Axial Flow Fan," World Acad. Sci. Eng. Technol.

[6]   Akdag, O. C. D. D. I. O. U., 2013, "Experimental investigation of convective heat transfer on a flat plate," Int. Commun. Heat Mass Transf.

[7]   Xiao-Ming, Z. J.-Z. T., 2013, "Flow and heat transfer characteristics under synthetic jets impingement driven," **48**, pp. 134–146.

[8]   Swift, B. L. S. G. W., 2001, "Synthetic Jets at Large Reynolds Number and Comparison," Am. Inst. Aeronaut. Astronaut.

[9]   Rusovici, C. O. C. P. R., 2011, "A coupled field finite element modeling," Intellig. Mater. Syst. Struct, pp. 161–173.

[10]   Pavlova, M. A. A., 2006, "Electronic cooling with synthetic jet impingement," Heat Transf., pp. 897–907.

[11]   "Nuventix" [Online]. Available: www.nuventix.com/technology.

[12] Glezer, B. L. S. a. A., 1998, "The formation and evolution of synthetic jets," Phys. FLUIDS, **10**.

[13] Liu, S.-F., Huang, R.-T., Sheu, W.-J., and Wang, C.-C., 2009, "Heat transfer by a piezoelectric fan on a flat surface subject to the influence of horizontal/vertical arrangement," Int. J. Heat Mass Transf., **52**(11-12), pp. 2565–2570.

[14] Petroski, J., Arik, M., and Gursoy, M., 2010, "Optimization of piezoelectric oscillating fan-cooled heat sinks for electronics cooling," IEEE Trans. Components Packag. Technol., **33**(1), pp. 25–31.

[15] Kimber, M., and Garimella, S. V., 2009, "Measurement and prediction of the cooling characteristics of a generalized vibrating piezoelectric fan," Int. J. Heat Mass Transf., **52**(19-20), pp. 4470–4478.

[16] Açikalin, T., Garimella, S. V., Raman, A., and Petroski, J., 2007, "Characterization and optimization of the thermal performance of miniature piezoelectric fans," Int. J. Heat Fluid Flow, **28**(4), pp. 806–820.

[17] Bürmann, P., Raman, A., and Garimella, S. V., 2002, "Dynamics and topology optimization of piezoelectric fans," IEEE Trans. Components Packag. Technol., **25**(4), pp. 592–600.

[18] Bidkar, R. A., Kimber, M., Raman, A., Bajaj, A. K., and Garimella, S. V, 2009, "Nonlinear aerodynamic damping of sharp-edged flexible beams oscillating at low Keulegan–Carpenter numbers," J. Fluid Mech., **634**, p. 269.

[19] Sudipta Basak, Arvind Raman, S. V. G., 2005, "Dynamic Response Optimization of Piezoelectrically Excited Thin Resonant Beams," J. Vib. Acoust., **127**.

[20]   Berg, R. F., Yao, M., and Panzarella, C. H., 2007, "Hydrodynamic Force on a Cylinder Oscillating at Low Frequency," (December).

[21]   Sobey, I. J., 1982, "Oscillatory flows at intermediate Strouhal number in asymmetric channels," J. Fluid Mech., **125**, pp. 359– 373.

[22]   Yang, S.-J., 2002, "A numerical investigation of heat transfer enhancement for electronic devices using an oscillating vortex generator," An Int. J. Comput. Methodol., **42**(3).

[23]   White, F., Fluid Mechanics, McGraw-Hill.

[24]   Ghaffari, O., Ikhlaq, M., and Arik, M., 2015, "An Experimental Study of Impinging Synthetic Jets for Heat Transfer Augmentation," International Journal of Air-Conditioning and Refrigeration, p. 1550024.

[25]   Bradski, G., and Kaehler, A., 2008, Learning OpenCV Computer Vision with the OpenCV Library, O'Reilly Media.

[26]   Thielicke, W., and Stamhuis, E. J., 2014, "PIVlab – Towards User-friendly, Affordable and Accurate Digital Particle Image Velocimetry in MATLAB," J. Open Res. Softw., **2**(1), p. e30.

[27]   Solovitz, S. O. A. and S. A., "Development of a Variable Diameter Synthetic Jet Actuator," ASME 2014 Int. Mech. Eng. Congr. Expo., **1**.

[28]   R. J. Moffat, "Describing the uncertainties in experimental results," *Exp. Therm. Fluid Sci.*, vol. 1, no. 1, pp. 3–17, 1988.